

UNIVERSITY OF KWAZULU-NATAL



HI Intensity Mapping and Cross-Correlation Science with HIRAX

by

Warren Naidoo

Supervisor: **Prof. Kavilan Moodley**

Submitted in fulfillment of the academic requirements for the degree
of Master of Science in the University of KwaZulu Natal Westville
School of Maths, Stats and Computer Science

Durban

December

As the candidates supervisor I have approved this thesis for
submission

Signed: _____ Name: Kavilan Moodley Date: 28/02/2020

Abstract

In the last few decades, we have seen a wealth of information being extracted from a wide range of astronomical observations. CMB experiments and galaxy surveys have pioneered most of the advances made in understanding the current cosmological paradigm. As successful as these surveys have been, the prospects of intensity mapping of the 21cm line emission from neutral hydrogen (HI) provides an exciting new probe to map out the three dimensional cosmological modes over a large redshift range. Intensity mapping of the 21cm signal provides a biased tracer of the large scale structure distribution of the universe. Intensity mapping experiments have the advantage of being cheaper and able to map out larger volumes of the universe much faster than conventional galaxy surveys since we don't need to resolve individual galaxies.

In this thesis we study the cosmological constraints from the HI intensity mapping experiment, HIRAX, which is currently being developed to measure the cosmic 21cm signal in the 400 – 800 MHz frequency band. We examine the ability of the HIRAX experiment to detect the 21cm signal and we forecast the constraints this detection can place on the baryonic acoustic oscillation signal, the HI parameters and the cosmological parameters. We find that HIRAX will be able to obtain high precision measurements of the 21cm signal with a cumulative signal to noise ratio of 900 over the full bandwidth. Combined with Planck priors, we find that these measurements can constrain the dark energy equation of state parameters below the 5% level at 1σ confidence, with a corresponding dark energy figure of merit of 436.

We also examine how the HIRAX interferometer array layout affects the sensitivity of the instrument as a function of angular scale and frequency, which is relevant to the foreground removal. We quantify different metrics based on the distribution of the baseline redundancy for the different layouts to compare the data rate, data volume, calibration, sensitivity and foreground removal performance. We wish to optimise the array layout to best balance these constraints to achieve the HIRAX science goals.

We then study the cross-correlation of the HIRAX 21cm measurements with other large scale structure probes. We first compute the cross-correlation of the 21cm signal with the CMB lensing convergence field. We find that the two point cross-correlation of the 21cm intensity mapping with the CMB lensing convergence vanishes due to a loss of large scale line of sight modes in 21cm foreground subtraction. We then compute the integrated bispectrum $B_{\ell}^{2121\kappa}$ and find that we can obtain a strong detection of this signal. We show how the bispectrum in combination with the 21cm autocorrelation measurement can break the degeneracy between $f\Omega_{HI}$ and σ_8 thus independently constraining them. In addition the bispectrum can improve the constraints on dark energy parameters, improving the dark energy figure of merit for HIRAX to 927 in combination with Planck priors. In addition to the CMB lensing convergence cross-correlation, we demonstrate that HIRAX measurements can be cross-correlated with spectroscopic and photometric galaxy surveys obtaining high signal to noise ratios. We find that the spectroscopic survey cross-correlation can constrain the HI and galaxy parameters to below the percent level.

Acknowledgments

Firstly, I would like to acknowledge my supervisor, Prof Kavilan Moodley, for his knowledge, patience, wisdom and support. I am grateful for the guidance which has allowed me to strive for excellence and achieve things I did not know I could. I have been able to learn a great deal from such excellent mentorship.

I would like to acknowledge Dr Devin Crichton for his ever present willingness to offer help providing many useful discussions and extensive knowledge on astronomy and programming. I am thankful to Dr Moumita Aich for the various conceptual explanations and continued help in my research.

I wish to thank Prof Jon Sievers and Prof Martin Bucher for their vast knowledge and useful discussions on the array layout simulations and analysis. It has been extremely helpful to engage and learn from the experience offered by these brilliant researchers.

I am thankful to all the members of the Astrophysics and Cosmology Research Unit for their continued support, guidance and interesting conversations. I would like to thank Strini Rajgopaul who has been instrumental in helping me get the opportunity to pursue a career in science and for his support and encouragement.

I am truly grateful to the South African Radio Astronomy Observatory (SARAO) for the financial assistance of the towards this research (www.ska.ac.za). The opportunity created by SARAO has been crucial for me to pursue my dream to be involved in research.

Last, but certainly not least, I am grateful to my parents, without which this opportu-

nity would not have been possible. Their hard work, persistence, guidance and belief have encouraged and inspired me to work harder and make sure I succeed. I would also like to thank all of my friends, a list too numerous to fit in a single thesis, for their support and friendship helping me manage the pressure and stressful nature of research with laughter and encouragement.

Preface

The work described in this dissertation was carried out in the School of Mathematics, Statistics and Computer Science at University of KwaZulu-Natal, Durban, from January 2018 to December 2019, under the supervision of Prof K. Moodley.

This study represents original work by the author and has not otherwise been submitted in any form for any degree or diploma to any other tertiary institution. Where use has been made of the work of others, it is duly acknowledged in the text.

Declaration of Non-Plagiarism

I, **Warren Naidoo**, declare that

1. The research reported in this thesis, except where otherwise indicated, is my original research.
2. This thesis has not been submitted for any degree or examination at any other university.
3. This thesis does not contain other personal data, pictures, graphs or other information, unless specifically acknowledged as being sourced from other persons.
4. This thesis does not contain other persons' writing, unless specifically acknowledged as being sourced from other researchers. Where other written sources have been quoted, then:
 - a. Their words have been re-written but the general information attributed to them has been referenced
 - b. Where their exact words have been used, then their writing has been placed in italics and inside quotation marks, and referenced.
5. This thesis does not contain text, graphics or tables copied and pasted from the Internet, unless specifically acknowledged, and the source being detailed in the thesis and in the References sections.

Signed _____

Contents

Abstract	i
Acknowledgments	iii
Preface	v
Declaration of Non-Plagiarism	vi
1 Introduction	1
2 Cosmological Model and Observational Probes	6
2.1 Standard Model of Cosmology	6
2.1.1 Friedmann-Lemaître-Robertson-Walker Model	6
2.1.2 Cosmological Distances	10
2.1.3 Cosmological Perturbations	12
2.2 Observational Probes	18
2.2.1 CMB Anisotropy	18
2.2.2 Cosmological Matter Power Spectrum	22
2.2.3 Baryonic Acoustic Oscillations	25
2.2.4 Redshift Space Distortions	27
2.2.5 Gravitational Lensing	31

3	21cm Intensity Mapping	34
3.1	Theoretical Model	36
3.1.1	The 21cm Power Spectrum	37
3.1.2	Foregrounds	40
3.2	The HIRAX Survey	42
3.3	HI Intensity Mapping BAO Constraints	45
3.3.1	Fisher Formalism	46
3.3.2	Dark Energy Constraints	51
3.4	HIRAX Array Layout Optimisation	55
3.4.1	Array Layout Strategies	56
3.4.2	Grid Layout Comparison and Analysis	60
4	Cross-Correlations With HI Intensity Mapping	66
4.1	HI IM-CMB Lensing Cross-Correlation	67
4.1.1	CMB Lensing Convergence	68
4.1.2	Vanishing Of The Two Point Cross-Correlation	72
4.1.3	The Bispectrum Estimator	74
4.1.4	Detectability Of The Bispectrum	79
4.1.5	Parameter Constraints	81
4.2	HI IM-Galaxy Survey Cross-Correlation	84
4.2.1	Spectroscopic Survey Cross-Correlations	85
4.2.2	Photometric Survey Cross-Correlations	95
5	Conclusion	100
A	Fisher Matrix Derivatives	103
A.1	The 21cm Signal Derivatives	103
A.2	The Bispectrum Derivatives	105
A.3	The Convergence Field Derivatives	107
A.4	Transformation Matrix Derivatives	107

B	The Bispectrum Derivation	109
B.1	The Squeezed Limit Bispectrum	109
B.2	The 21cm Autocorrelation and Bispectrum Covariance	114
B.3	The Bispectrum Variance	117

Chapter 1

Introduction

Cosmologists in recent decades have made considerable strides to produce a consistent standard model which describes the observations of the universe we live in. Some of the probes used by cosmologists to learn about the nature and content of our universe includes the cosmic microwave background (CMB) radiation [1, 2, 3], galaxy clustering counts [4, 5], type Ia supernova [6], Cepheid distances to galaxies [7], baryonic acoustic oscillations (BAOs) [8, 9], cosmic shear [10] and Ly α forest [11] observations. These measurements suggest we live in a universe which expanded from some primordial singularity about 13.7 billion years ago and is currently made up of 70% dark energy, 25% dark matter and 5% baryonic (ordinary) matter.

We currently understand that at present times, dark energy (DE) and dark matter (DM) dominate the energy budget of the universe but these are virtually unknown quantities. Dark energy drives the accelerated expansion of our universe. The first evidence for the accelerated expansion of our universe was provided by type Ia supernova measurements [6, 12, 13]. Type Ia supernova events were used to track the expansion of the universe because they serve as a standard candle of known brightness. These measurements suggest that the universe is undergoing an accelerated expansion at late times but was in fact decelerating at earlier times indicating that dark energy only dominates at late times.

Dark matter remains a long standing mystery in our universe [14, 15]. First inferred by

Zwicky in 1933 [16] by studying the dispersion velocity of the Coma cluster, where he obtained an inconsistently high dispersion velocity given the visible matter of the cluster. Subsequent observations such as rotation curves of the Andromeda galaxy in 1970 gave the same evidence for the existence of dark matter [17]. Dark matter has since been described as the missing matter that holds galaxies together and evidently it only interacts gravitationally with no pressure and no electromagnetic interactions. Gravitational lensing also provides indirect evidence for dark matter (see [18] for a review). We know from general relativity (GR) that gravity will influence the path trajectory of photons and this implies that light from distant objects can be lensed by intervening mass along the line of sight to an observer. The effect of lensing by galaxy clusters has been used to infer dark matter contributions to many known galaxy clusters and individual galaxies' showing again that there exists gravitationally interacting matter that we cannot see [19]. In recent times, CMB measurements have put forward strong arguments for the existence and content of dark matter in our universe. The position of the acoustic peaks in the CMB spectra helps pin down the contribution to the overall matter content by dark matter [20].

At early times (10^{-36} seconds after the Big Bang singularity to about $10^{-33} - 10^{-32}$ seconds) cosmic inflation rapidly expanded the size of our universe by a factor of 10^{26} [21]. Cosmic inflation is understood to have magnified the quantum field fluctuations that exist into density fluctuations of the matter field which seeded the large scale structure perturbations we observe today [22, 23]. The density fluctuations produced from cosmic inflation can be seen in the temperature variations in the observed CMB light that was emitted around 380 000 years after the Big Bang. Following the inflationary period, the universe has continued to expand outward but at a much slower rate. At late times however, the expansion rate of the universe has accelerated which we believe to be caused by the influence of dark energy.

Detailed studies of CMB measurements have already provided a wealth of high precision constraints on the current cosmological parameters (see [24] for a review). The CMB is referred to as the 'afterglow' of the big bang because it is the primordial light in the universe. Studies of the CMB temperature maps reveal slight fluctuations in the early universe. These temperature fluctuations in the CMB are thought to seed the large scale density fluctuations

that would eventually form. The CMB temperature is quite low, about 3 degrees above absolute zero and hence requires sensitive measurements at low temperatures, with such experiments including ground based [25, 26], balloon borne [27, 28, 29] and space based [1, 2, 3] surveys. We provide more details on the CMB and the information that can be extracted from it in Section 2.2.1.

Measurements from the CMB as well as galaxy clustering have also provided evidence for baryonic acoustic oscillations. The BAO is the characteristic length scale in the matter density field. This preferred clustering scale came about due to the coupled photon-baryon fluid which underwent oscillations due to the opposing forces of gravity and radiation pressure in an expanding universe before recombination. Evidence for the BAO can be seen as a bump in the correlation function of galaxy surveys like SDSS [8] and 2dFGRS [9] and as indirect evidence from the acoustic peaks of the CMB temperature power spectrum. Other galaxy survey detections of the BAO were made by the 6DF [30], WiggleZ [31] and Baryon Oscillation Spectroscopic Survey (BOSS) [32] projects. Since the BAO has a characteristic length scale preserved in the matter distribution of the primordial universe that has been calibrated by CMB measurements it provides an excellent candidate as a standard ruler to measure the cosmic expansion history. Measuring how the BAO scale evolves with time will provide constraints for dark energy models since dark energy influences the expansion rate of the universe. Historically, there has been significant interest in using BAOs to constrain cosmological parameters, and it has already been demonstrated how the detection can be used to measure cosmological parameters [33, 34]. Apart from detecting galaxies in BAO surveys using their optical emissions, galaxies can also be detected through their neutral hydrogen content.

The advent of star formation has meant that much of the neutral hydrogen (HI) in our universe would undergo reionization therefore leaving the remaining HI to be found mostly in the dense regions of galaxies and the intergalactic medium. For this reason HI is believed to be a good tracer of the underlying large scale structure (LSS) and why intensity mapping (IM) of the 21cm line is such a promising field. Intensity mapping is a technique for measuring integrated line emission from radio sources in the universe over a large range of frequencies.

These IM surveys can survey larger volumes much quicker than traditional galaxy surveys and at lower cost. HI (or 21cm) IM experiments are a promising path for improved large scale structure measurements of our universe [35, 36, 37]. Future IM experiments plan to measure the neutral hydrogen distribution through the spin flip transition line emission in our universe. This will provide a biased measurement of the underlying large scale structure (LSS) distribution. Measurements of the LSS from HI surveys will be able to pick out the BAO signal in the epochs of the universe when dark energy starts to dominate the expansion rate. Planned and current IM experiments includes SKA [38], MeerKAT [39], CHIME [40], HIRAX [41], Tianlai [42], BINGO [43] and FAST [44]. These experiments are showing great promise in their forecast for making precise cosmological measurements and in early results related to their detection of fast radio bursts (FRBs). In this thesis we study the cosmological forecasts for the HIRAX experiment and investigate how the survey design can be used to optimise the constraints.

In addition to the individual probes that can be used to study the universe we can also employ the technique of cross-correlations between different tracers to improve the information we get. Cross-correlation studies of CMB lensing and galaxy surveys can constrain the galaxy population distributions and the LSS biases. The cross-correlation here can also independently constrain the neutrino mass and optical depth information as shown by [45]. By cross-correlating CMB lensing with quasars it has also been shown that the quasar population traces the matter distribution and constrain the quasar bias [46]. Cross-correlation surveys for CMB lensing and HI measurements have also been considered showing that this signal would be able to constrain HI parameters such as the bias and HI fraction however this signal seems to be too small and detection is unlikely [47]. HI surveys have also been cross-correlated with galaxy surveys which has been successful in making the first indirect detections of HI intensity mapping [48, 49]. HI cross-correlations with photometric galaxy surveys can also be used to calibrate the galaxy redshifts in photometric surveys [50]. In this thesis we show how HI measurements from HIRAX can be cross-correlated with CMB lensing surveys and find that this correlation will in fact be too weak for detection but by using higher order correlations like the bispectrum we can recover the bispectrum signal.

We also show how HI cross-correlation with galaxy surveys will provide high signal to noise measurements that can be used to constrain HI and galaxy parameters.

The rest of this thesis is structured as follows. In Chapter 2 we discuss the current standard model of cosmology and introduce the theoretical background needed for the subsequent chapters. We also highlight some of the observational probes used by cosmologists which are most relevant to this thesis. In Chapter 3 we discuss the 21cm line emission and the HIRAX experiment designed to measure this signal. We investigate how the HIRAX experiment will be able to make strong detection of the 21cm signal and show high signal to noise ratio (SNR) estimates. We then compute forecasts constraints on the BAO and constraints on the cosmological and HI model parameters. We further show how optimising the array layout can improve our overall sensitivity and foreground mitigation. In Chapter 4 we investigate the prospects for cross-correlation surveys between HIRAX and CMB lensing and galaxy surveys. We show how we can obtain improvements on the HI parameter constraints by computing a bispectrum with the CMB lensing convergence field. We also show improved cosmological parameter constraints. We then compute the cross-correlation for HIRAX and galaxy surveys. We consider both spectroscopic and photometric surveys showing the promising detection in both cases in the form of the signal to noise ratio. We conclude in Chapter 5 where we summarise the significance of the results and discuss the context of this work in the broader field. We also discuss ideas for future work that will follow on from the results presented in this thesis.

Chapter 2

Cosmological Model and Observational Probes

2.1. Standard Model of Cosmology

It has become evident through current observations that we are living in a universe that is dominated by dark energy and dark matter. Present information also suggests that the universe is spatially flat and can be quantified by a few observable cosmological parameters. In this section we discuss the theoretical foundations of the standard model of cosmology.

2.1.1 Friedmann-Lemaître-Robertson-Walker Model

In 1915, Albert Einstein completed his theory of general relativity which describes space-time as a 4-dimensional manifold that can be influenced by the presence of matter. The Einstein field equations are

$$R_{\mu\nu} - \frac{1}{2}g_{\mu\nu}R = \frac{8\pi G}{c^4}T_{\mu\nu}, \quad (2.1)$$

where $R_{\mu\nu}$ and R is the Ricci tensor and Ricci scalar respectively. The metric tensor is denoted by $g_{\mu\nu}$ which describes the line element of a given manifold. Here G is the gravitational constant, c is the speed of light and $T_{\mu\nu}$ is the momentum-energy tensor. The left hand side of the field Equation 2.1 is purely geometric describing the curvature of space and the right

hand side is purely physical describing the matter distribution of a particular fluid. For a perfect isotropic fluid with energy density ρ and pressure p , T_{ν}^{μ} is given by

$$T_{\nu}^{\mu} = \begin{pmatrix} -\rho c^2 & 0 & 0 & 0 \\ 0 & p & 0 & 0 \\ 0 & 0 & p & 0 \\ 0 & 0 & 0 & p \end{pmatrix}. \quad (2.2)$$

According to our most recent observations, we are living in a smooth, expanding, spatially flat universe whose energy content is dominated by dark energy and dark matter. The cosmological principle states that on large scales the universe is homogeneous and isotropic. This simply means that the universe looks the same in all directions and is the same at every point. Weyl's postulate says that the world lines of galaxies form a 3-bundle of non-intersecting geodesics orthogonal to a series of space-like hypersurfaces. The cosmological principle together with Weyl's postulate suggest the form of the line element for our universe as

$$ds^2 = -c^2 dt^2 + a(t) \left[\frac{dr^2}{1 - kr^2} + r^2(d\theta^2 + \sin^2 \theta d\phi^2) \right] \quad (2.3)$$

where $a(t)$ is the scale factor which relates the fixed comoving separation between two comoving observers to the physical distance between. For some real distance \mathbf{r} and comoving distance \mathbf{x} the scale factor relates these two distances by $\mathbf{r} = a(t)\mathbf{x}$. The parameter k above is the curvature parameter. For a flat universe $k = 0$, whereas for a 'closed' universe $k = 1$ and for an 'open' universe $k = -1$. CMB measurements suggest we live in a spatially flat universe with $k = 0$. The line element in Equation 2.3 is known as the Robertson-Walker (RW) metric. To account for the effects of dark energy in the Einstein field equations one is free to add a constant term Λ on the left hand side of the equation without violating the conservation of the stress-energy tensor to give

$$R_{\mu\nu} - \frac{1}{2}g_{\mu\nu}R + \Lambda g_{\mu\nu} = \frac{8\pi G}{c^4}T_{\mu\nu}. \quad (2.4)$$

Solving the field equations with the RW metric shown in Equation 2.3 we get the Friedmann and acceleration equations respectively which describes the evolution of the scale factor of the universe

$$\left(\frac{\dot{a}}{a}\right)^2 = \frac{8\pi G}{3}\rho - \frac{Kc^2}{a^2} + \frac{\Lambda c^2}{3}, \quad (2.5)$$

$$\frac{\ddot{a}}{a} = \frac{-4\pi G}{3}\left(\rho + \frac{3p}{c^2}\right) + \frac{\Lambda c^2}{3}. \quad (2.6)$$

$H(t) = \frac{\dot{a}}{a}$ is referred to as the Hubble parameter. The Hubble parameter describes how the scale factor changes with time. The value of the Hubble parameter today, $H(t_0) = H_0$ is known as the Hubble constant and was described initially by Edwin Hubble in 1929 when he discovered that there exist a linear relation between the recessional velocities of Cepheid variable stars and their proper distances [51].

Given the Friedmann Equations 2.6 and 2.5, we only further require an equation which relates the pressure to density to solve for the time evolution of these quantities. An equation which relates the pressure of a fluid to its energy density is referred to as an equation of state and is generally given by

$$p(\mathbf{r}, t) = w\rho(\mathbf{r}, t) \quad (2.7)$$

where the constant w is the equation of state parameter. For dust, which has no pressure $w = 0$ and for radiation or relativistic matter $w = 1/3$. For the cosmological constant associated with the cosmological expansion $w = -1$. By combining the Friedmann Equations 2.5 and 2.6 we can get the pressure - density equation

$$\frac{d}{dt}(a^3 pc^2) = p \frac{d}{dt}a^3. \quad (2.8)$$

Equation 2.8 solved for a universe comprised of mainly dust with no pressure $w = 0$ gives $\rho_m(t) = \rho_{m,0}a^{-3}$ and for a radiation dominated universe with $w = 1/3$ we get $\rho_r(t) = \rho_{r,0}a^{-4}(t)$. For a universe dominated by a cosmological constant $w = -1$ the density remains constant throughout the evolution of the universe.

Conceptually we can understand the above density solutions in a physical way. If we have

a fixed density of fluid in an expanding volume then the density of that fluid would decrease by the increasing volume which is proportional to the scale factor. Hence the density of the matter dominated universe falls off as $\rho_m(t) \propto \rho_{m,0}a^{-3}(t)$. For a radiation dominated fluid however, the wavelength of the photon is stretched by expansion by a factor of a meaning the energy decreases by a^{-1} . This means that the total energy density for radiation scales as $\rho_r(t) \propto \rho_{r,0}a^{-4}$. Substituting the density solutions back into the Friedmann equations we can solve for the scale factor of the universe to get for a matter or dust dominated universe $a(t) \propto t^{2/3}$ and for radiation dominated $a(t) \propto t^{1/2}$. This indicates that the density in the radiation dominated era falls off faster than in the matter dominated era. This implies that a universe which starts out radiation dominated will not remain radiation dominated forever. No matter how small the initial matter contribution is, it will eventually overtake the radiation. For the dark energy contribution in the form of a cosmological constant, the density remains constant throughout. From the above solution one can see how a universe which may initially be dominated by radiation with small amounts of matter and dark energy will transition to become matter dominated and eventually dark energy dominated. This is exactly what we observe in our universe today.

Given our description for the standard model of cosmology there still remains quantities to be determined by observation. The Hubble constant H_0 was an example of such a quantity which measures the expansion rate. Another important quantity of interest would be the density of the universe. The critical density is defined to be the density which makes a universe flat ($k = 0$), which from Equation 2.5 neglecting Λ is

$$\rho_c = \frac{3H_0^2}{8\pi G}. \quad (2.9)$$

It is then customary to quote the density of a species ρ_x relative to the critical density by defining the dimensionless density parameter

$$\Omega_x = \frac{\rho_x}{\rho_c}. \quad (2.10)$$

The Friedmann equation in terms of the dimensionless density parameters can be written as

$$H^2(t) = H_0^2 (a^{-4}(t)\Omega_{r,0} + a^{-3}(t)\Omega_{m,0} + a^{-2}(t)(1 - \Omega_{m,0} - \Omega_\Lambda) + \Omega_\Lambda), \quad (2.11)$$

where $\Omega_\Lambda = \frac{\Lambda c^2}{3H_0^2}$. It is important to remember that these solutions describe a smooth and homogeneous universe.

2.1.2 Cosmological Distances

We discuss the various distance measures used to quantify distances to objects based on different types of observations. We first define the concept of redshift. Due to the expansion of the universe, light travelling to an observer from distance objects will have its wavelength stretched. The result of increasing wavelength means a decrease in frequency or energy. Hence when we observe distant light we can expect it to be shifted towards the red end of the electromagnetic spectrum. This phenomenon is referred to as redshift. Therefore the redshift z of an object can be defined in terms of the fractional change in the wavelength

$$z = \frac{\lambda_{obs} - \lambda_{emit}}{\lambda_{emit}} = \frac{\lambda_{obs}}{\lambda_{emit}} - 1, \quad (2.12)$$

where λ_{obs} is the observed wavelength and λ_{emit} is the emitted wavelength. Redshift can also be related to the scale factors at the time of emission and observation as

$$1 + z = \frac{\lambda_{obs}}{\lambda_{emit}} = \frac{a(t_{obs})}{a(t_{emit})} = \frac{1}{a(t)}. \quad (2.13)$$

The last equality follows from setting $a(t_{obs})$ as 1 and taking t_{emit} to be any general time.

Given that light travels at a constant speed of c , the proper distance D_{prop} can be defined as the travel time of a light ray between two points

$$D_{prop}(z) = c \int_{t(z)}^{t_0} dt = \frac{c}{H_0} \int_{a(z)}^{a(z_0)} \frac{da}{\sqrt{a^{-1}\Omega_{m,0} + (1 - \Omega_{m,0} - \Omega_\Lambda) + a^2\Omega_\Lambda}}. \quad (2.14)$$

By the definition of comoving co-ordinates we can also define the comoving distance. We

denote the comoving distance by χ_{\parallel} and it is related to the proper distance by $D_{prop} = a\chi_{\parallel}$. The comoving distance can then be written as [52]

$$\chi_{\parallel}(z) = \int_0^z \frac{cdz'}{H(z')}. \quad (2.15)$$

The angular diameter distance is the apparent distance an object appears to be based on its apparent angular size on the sky $D_A = l/\theta$. Here l is the physical length of the object and θ is the angle it subtends. In a flat universe the angular diameter distance is given as

$$D_A = a\chi_{\parallel} = \frac{\chi_{\parallel}}{1+z}. \quad (2.16)$$

Another way to measure cosmological distances is by using the flux emitted by an observed object provided the object has a well known luminosity. The flux measured over some distance d is simply

$$F = \frac{L}{4\pi d^2} \quad (2.17)$$

where L is the luminosity. The picture however gets more complicated in an expanding universe. To account for the expansion we consider the problem in comoving co-ordinates

$$F = \frac{L(\chi_{\parallel})}{4\pi\chi_{\parallel}^2}. \quad (2.18)$$

where $L(\chi_{\parallel})$ is the luminosity through some comoving spherical shell with radius χ_{\parallel} . If we assume that the object emits photons which all have the same initial luminosity we can relate the measured luminosity through an expanding universe to the known luminosity by $L(\chi_{\parallel}) = a^2L$. This then gives

$$F = \frac{La^2}{4\pi\chi_{\parallel}^2} \quad (2.19)$$

where we can see that if we now define the luminosity distance as

$$D_L = \frac{\chi_{\parallel}}{a} \quad (2.20)$$

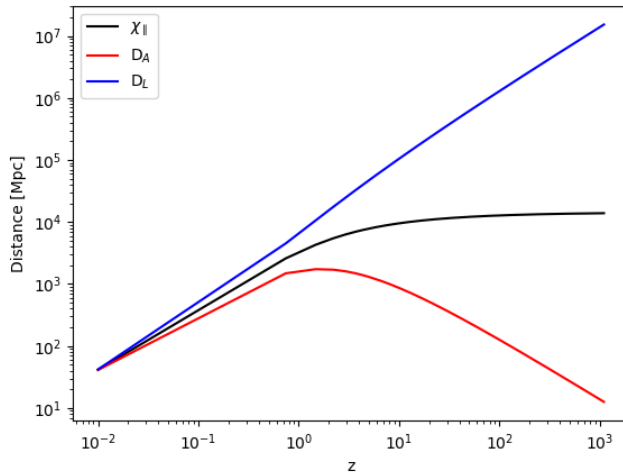


Figure 2.1: A comparison of three cosmological distance measures. From top to bottom luminosity distance, comoving distance and angular diameter distance. This plot is for a universe with $\Omega_m = 0.3$, $\Omega_\Lambda = 0.7$ and $\Omega_k = 0$.

we recover an expression for the flux like that of the form in Equation 2.17. We show in Figure 2.1 how the comoving distance, angular diameter distance and luminosity distance change with redshift. We see that at low redshifts they evolve in a similar way meaning that these distance measures give the same results for nearby objects. For distant objects they behave differently. The comoving distance asymptotically approaches a constant $2c/H_0$ for large z . The angular diameter distance reaches a maximum then falls off making more distant objects appear larger. The luminosity distance increases indefinitely with redshift.

2.1.3 Cosmological Perturbations

The solutions described in Section 2.1.1 describes a smooth homogenous universe. In reality, we observe a universe with perturbations in the form of large scale structure formation. To

obtain the solutions for a perturbed universe we perturb the field equations

$$\begin{aligned}
g_{\mu\nu} &= \bar{g}_{\mu\nu} + \delta g_{\mu\nu} \\
G_{\mu\nu} &= \bar{G}_{\mu\nu} + \delta G_{\mu\nu} \\
T_{\mu\nu} &= \bar{T}_{\mu\nu} + \delta T_{\mu\nu}
\end{aligned} \tag{2.21}$$

to linear order. We can write the form of the perturbed metric tensor as [53]

$$ds^2 = a^2(\eta) [-(1 + 2A)d\eta^2 + 2B_i d\eta dx^i + (\delta_{ij} + h_{ij}) dx^i dx^j] \tag{2.22}$$

where the conformal time is describes as $\eta = \int_0^t \frac{cdt'}{a(t')}$. Here δ_{ij} is the spatial part of the metric tensor and $h_{ij} = 2 \left[C\delta_{ij} + D_i D_j E + D_i \hat{E}_j + \hat{E}_{ij} \right]$ where $D^i \hat{E}_j = 0$ and $D^i \hat{E}_{ij} = 0 = \hat{E}_j^i$. The tensor \hat{E}_j^i is not only divergenceless but also traceless. Essentially we have now split the 10 degrees of freedom of the metric tensor into four scalars A, B, C and D, two vectors B_i and E_i of two degrees of freedom each and one tensor E_{ij} also having two independent degrees of freedom.

General relativity is constructed such that a coordinate transformation leaves physical equations unchanged. Phrased in another way, the physical equations are invariant under coordinate transformation. When applied to the special background and perturbations case, this invariance is no longer an actual coordinate transformations since the background is kept fixed. This is called a gauge transformation. For a given coordinate x^a and a coordinate in the perturbed spacetime \tilde{x}^a we relate them by $x^\alpha = \tilde{x}^\alpha + \xi^\alpha$ where we only keep the linear terms of ξ^a since it and its derivatives are small enough to do so. The perturbations to covariant and mixed tensors of rank 2 transform in the following way [54]

$$\begin{aligned}
\delta \tilde{B}_{\mu\nu} &= \delta B_{\mu\nu} - \xi_{,\mu}^\alpha \bar{B}_{\alpha\nu} - \xi^{\beta, \nu} \bar{B}_{\mu\beta} - \bar{B}_{\mu\nu, \gamma} \xi^\gamma \\
\delta \tilde{B}_\nu^\mu &= \delta B_\nu^\mu - \xi_{,\alpha}^\mu \bar{B}_\nu^\alpha - \xi^{\beta, \nu} \bar{B}_\beta^\mu - \bar{B}_{\nu, \gamma}^\mu \xi^\gamma
\end{aligned} \tag{2.23}$$

To complete our description of the perturbed cosmological solutions we need to perturb the stress-energy tensor for our field equations. For a perfect fluid we can described the

perturbed stress-energy tensor in terms of its components

$$\rho = \bar{\rho} + \delta\rho, \quad p = \bar{p} + \delta p \quad \text{and} \quad u^i = \bar{u}^i + \delta u. \quad (2.24)$$

We know that the metric tensor can be used to raise and lower indices and the velocity field is $u^i = \frac{v^i}{a} = \frac{dx^i}{d\eta} \frac{1}{a}$ thus we can write $u^\mu = \frac{1}{a}(1 - A, v_i)$ and $u_\mu = a(-1 - A, v_i - B - i)$. Like we did for the metric tensor, we can divide the stress energy perturbation. In linear perturbation theory the scalar, vector and tensor perturbations evolve independently and can be treated separately. The scalar perturbations are most relevant to structure formation. Vector perturbations decay with time and do not have a large influence at later times. The tensor perturbations have interesting cosmological significance since these correspond to gravitational waves.

Scalar Perturbations

We can obtain the evolution of the scalar perturbations A,B,D and E using Equation 2.23 to get

$$\begin{aligned} \tilde{A} &= A - \xi^{0'} - \frac{a'}{a}\xi^0 \\ \tilde{B} &= B + \xi' - \xi^0 \\ \tilde{D} &= D - \frac{1}{3}\Delta^2\xi + \frac{a'}{a}\xi^0 \\ \tilde{E} &= E + \xi \end{aligned} \quad (2.25)$$

and for scalar perturbations with $v_i = -v_{,i}$ we get

$$\tilde{\delta\rho} = \delta\rho - \bar{\rho}\xi^0, \quad \tilde{\delta p} = \delta p - \bar{p}\xi^0 \quad \text{and} \quad \tilde{v} = v + \xi' \quad (2.26)$$

Bardeen Potential

The Bardeen potentials are invariant under gauge transformations [55]

$$\begin{aligned}\Psi &= A + \mathcal{H}(B - E') + (B - E)' \\ \Phi &= D + \frac{1}{3}\Delta^2 E - \mathcal{H}(B - E')\end{aligned}\tag{2.27}$$

where \mathcal{H} is the conformal Hubble parameter.

Conformal - Newtonian Gauge

A common gauge used to compute the cosmological perturbations is the Newtonian gauge. Here we set $E^N = B^N = 0$, where the superscript N is used to refer to the conformal-Newtonian gauge. The transformation to the conformal Newtonian gauge is given by

$$\xi = -E\tag{2.28}$$

$$\xi^0 = -B + E'.\tag{2.29}$$

which gives

$$A^N = \Psi\tag{2.30}$$

$$D^N = \Phi.\tag{2.31}$$

We see in the conformal Newtonian gauge the non zero scalar potentials are just equal to the Bardeen invariant potentials. In this gauge these potentials have straight forward interpretations where Ψ describes how the Newtonian potential is perturbed and Φ gives the perturbation to the spatial curvature. We can now write the perturbed metric and stress-energy tensors in this gauge respectively as

$$ds^2 = a^2(\eta) [-(1 + 2\Psi)d\eta^2 + (1 - 2\Phi)\delta_{ij}dx^i dx^j]\tag{2.32}$$

and

$$\delta T_{\nu}^{\mu} = \begin{pmatrix} -\delta\rho^N & -(\bar{\rho} + \bar{p})(v_{,i}^N) \\ (\bar{\rho} + \bar{p})v_{,i}^N & \delta p^N \delta_j^i \end{pmatrix}. \quad (2.33)$$

Synchronous Gauge

Another common gauge used is the synchronous gauge where $A = B_i = 0$ [56]. The choice of gauge may depend heavily on the situation one is solving for but in general the synchronous gauge may be preferred in most computational cases due to its numerical advantages.

Evolution Of The Perturbations

In the conformal Newtonian gauge the scalar perturbation equations for a perfect fluid are given by

$$\Delta^2 \Psi = \frac{3}{2} \mathcal{H}^2 [\delta^N + 3\mathcal{H}(1+w)v^N] \quad (2.34)$$

$$\Psi' + \mathcal{H}\Psi = \frac{3}{2} \mathcal{H}^2 (1+w)v^N \quad (2.35)$$

$$\Psi'' + 3\mathcal{H}\Psi' + (2\mathcal{H}' + \mathcal{H}^2)\Psi = \frac{3}{2} \mathcal{H}^2 \frac{\delta p^N}{\bar{\rho}}. \quad (2.36)$$

We know that the stress-energy tensor is divergenceless and hence

$$T_{\nu;\mu}^{\mu} = 0 \quad (2.37)$$

which we use to get first order evolution equations for δ and v

$$(\delta^N)' = (1+w) (\Delta^2 v^N + 3\Phi') + 3\mathcal{H} \left(w\delta^N - \frac{\delta p}{\bar{\rho}} \right) \quad (2.38)$$

$$(v^N)' = -\mathcal{H}(1-3w)v^N - \frac{w'}{1+w}v^N + \frac{\delta^N}{\bar{p} + \bar{\rho}} + \Phi. \quad (2.39)$$

To obtain the full set of perturbation equations we consider the total energy density as a combination of various contributions

$$\rho = \rho_b + \rho_{DM} + \rho_\gamma + \rho_\nu + \rho_\Lambda. \quad (2.40)$$

In the above, ρ_b is the density of baryons which includes the electron contribution, ρ_{DM} is the dark matter density contribution, ρ_γ is the photon energy density, ρ_ν is the neutrino contribution and ρ_Λ is the contribution from dark energy. The various pressure contributions are $p_b = 0 = p_{DM}$, $p_\gamma = \rho_\gamma/3$, $p_\nu = \rho_\nu/3$ and $p_\Lambda = -\rho_\Lambda$. Decomposing the fields into their Fourier modes and solving we get the full set of perturbation equations. For linear perturbations different Fourier modes are uncorrelated so we can treat each mode separately and work with their amplitudes. Note that we consider dark energy to be homogenous in the universe, i.e. it does not have any perturbations.

$$\delta'_{DM} = -kv_{DM} + 3\Phi' \quad (2.41)$$

$$v'_{DM} = -\mathcal{H}v_{DM} + k\Phi \quad (2.42)$$

$$\delta'_b = -kv_b + 3\Phi' \quad (2.43)$$

$$v'_b = -\mathcal{H}v_b + k\Phi \quad (2.44)$$

$$\delta'_\gamma = -\frac{4}{3}kv_\gamma + 4\Phi' \quad (2.45)$$

$$v'_\gamma = \frac{1}{4}k\delta_\gamma + k\Phi + \text{collision term} \quad (2.46)$$

$$\delta'_\nu = -\frac{4}{3}kv_\nu + 4\Phi' \quad (2.47)$$

$$v'_\nu = \frac{1}{4}k\delta_\nu + k\Phi. \quad (2.48)$$

These equations describe the evolution of the perturbation to all components of the universe. Note that in the above equations we have neglected most collision terms since the only collision effect that turns out to be important is the momentum transfer between photons

and baryons, captured in the collision terms in the velocity equations [54].

2.2. Observational Probes

Here we discuss some of the observable probes in our universe and highlight the key theoretical features of these observables.

2.2.1 CMB Anisotropy

Here we discuss the description of the CMB anisotropies from temperature maps. CMB experiments measure temperature fluctuations over the sky. Figure 2.2 shows the 2018 Planck CMB map [57]. The figure shows hot and cold spots in the temperature field of the early universe. We use these hot and cold spots to infer density fluctuations in the matter distribution which seeded the large scale structure formation we observe today. We briefly outline the thermal description of the CMB anisotropy and the statistics (see [24] for a review).

Consider a temperature fluctuation in the CMB measurement as

$$\Theta(\hat{\mathbf{n}}) = \frac{T(\hat{\mathbf{n}}) - \bar{T}}{\bar{T}} = \frac{\Delta T}{\bar{T}} \quad (2.49)$$

where $\hat{\mathbf{n}}$ is the positional vector on the observed sky and \bar{T} is the mean CMB temperature. We decompose the temperature fluctuations using spherical harmonics over the angular sky

$$\Theta(\hat{\mathbf{n}}) = \sum_{\ell m} a_{\ell m} Y_{\ell m}(\hat{\mathbf{n}}) \quad (2.50)$$

where all the information about the temperature field is now contained in the $a_{\ell m}$ s. For a Gaussian random field all of the statistical information is contained in the power spectrum and for the measured CMB temperature fluctuation on the sky we consider the angular power spectrum as

$$\langle a_{\ell m} a_{\ell' m'}^* \rangle = \delta_{\ell\ell'} \delta_{mm'} C_{\ell}. \quad (2.51)$$

The angular temperature fluctuation is nothing but a projection of the initial spatial tem-

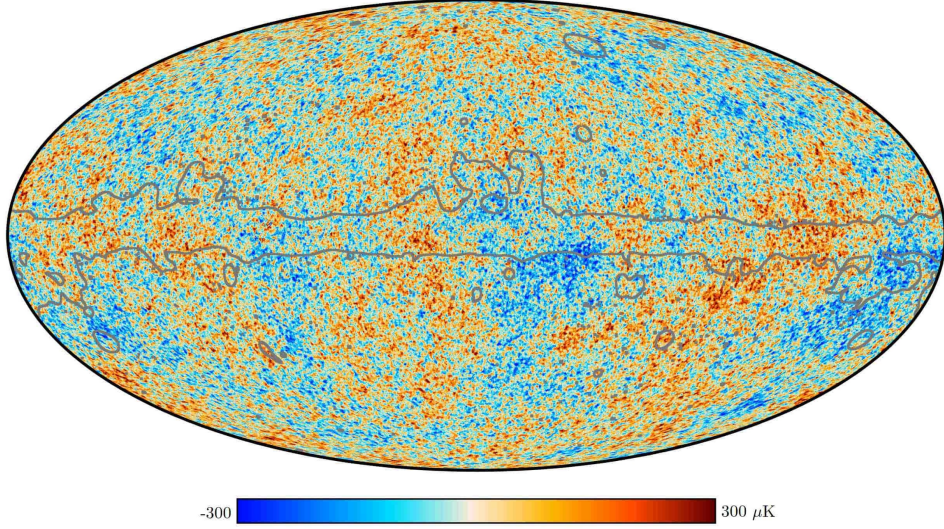


Figure 2.2: Planck 2018 temperature map. Temperature fluctuations here indicates density variations in the early universe. The grey outline shows the masking region of the galactic plane where the foreground residual is expected to be. Figure taken from [57].

perature fluctuation over the line of sight [58]

$$\Theta(\hat{\mathbf{n}}) = \int d\chi_{\parallel} \Theta(\mathbf{x}) \delta_D(\chi_{\parallel} - \chi_{\parallel}^*) \quad (2.52)$$

where the spatial temperature fluctuation would be $\Theta(\mathbf{x}) = (T(\mathbf{x}) - \bar{T}) / \bar{T}$. Like we did for the angular temperature fluctuation, we can decompose the spatial field at the last scattering surface into its harmonic modes which for a flat geometry would just be described by the Fourier transform

$$\Theta(\mathbf{x}) = \int \frac{d^3k}{(2\pi)^3} \Theta(\mathbf{k}) e^{i\mathbf{k}\cdot\mathbf{x}}. \quad (2.53)$$

We can now compute the primordial temperature power spectrum for the CMB

$$\langle \Theta(\mathbf{k}) \Theta^*(\mathbf{k}') \rangle = (2\pi)^3 \delta_D^3(\mathbf{k} - \mathbf{k}') P(k) \quad (2.54)$$

which we use to compute the two point correlation function in real space as

$$\langle \Theta(\mathbf{x}) \Theta(\mathbf{x}) \rangle = \int \frac{d^3k}{(2\pi)^3} P(\mathbf{k}) = \int dk \frac{k^2 P(\mathbf{k})}{2\pi^2}. \quad (2.55)$$

Finally to relate the angular temperature fluctuation to the spatial fluctuation we decompose the angular field into Fourier modes

$$\Theta(\hat{\mathbf{n}}) = \int \frac{d^3k}{(2\pi)^3} \Theta(\mathbf{k}) e^{i\mathbf{k}\cdot\chi_{\parallel}\hat{\mathbf{n}}} \quad (2.56)$$

and write the exponential function using the spherical Bessel functions j_{ℓ} as

$$e^{i\mathbf{k}\cdot\chi_{\parallel}\hat{\mathbf{n}}} = 4\pi \sum_{\ell m} i^{\ell} j_{\ell}(k\chi_{\parallel}) Y_{\ell m}(\hat{\mathbf{n}}) Y_{\ell m}(\hat{\mathbf{k}}). \quad (2.57)$$

With Equation 2.56 and Equation 2.57 put together we can compute the $a_{\ell m}$ s needed for the C_{ℓ} computation in Equation 2.51 which gives

$$\langle a_{\ell m} a_{\ell' m'}^* \rangle = \delta_{\ell\ell'} \delta_{mm'} \int dk j_{\ell}^2(k\chi_{\parallel}^*) \frac{k^2 P(k)}{\pi} = \delta_{\ell\ell'} \delta_{mm'} C_{\ell}. \quad (2.58)$$

Finally, we approximate the expression for the CMB temperature fluctuation angular power spectrum by assuming the spatial power spectrum $P(k)$ is slowly varying and we can remove it from the integral. In this approximation we also have $k\chi_{\parallel} \sim \ell$. The integral can then be evaluated as $\int_0^{\infty} j_{\ell}^2(x) d \ln x = 1/2\ell(\ell + 1)$ to give the result

$$C_{\ell} \approx \frac{\ell^2 P(\ell/\chi_{\parallel})}{\pi \chi_{\parallel} (\ell + 1)}. \quad (2.59)$$

It is common practice to plot the power spectrum in the flat sky limit as

$$\frac{\ell(\ell + 1)}{2\pi} C_{\ell} \approx \Delta_T^2 \quad (2.60)$$

where $\Delta_T^2 = k^3 P(k)/2\pi^2$. In Figure 2.3 we show the power spectrum of the CMB fluctuations along with observational data sets. The COBE [1] experiment made the first measurements of the CMB anisotropy but newer experiments are able to make measurements on much smaller scales. The acoustic peaks in the CMB power spectrum arise from the pressure - gravity balance. Solving the basic fluid equations for the universe before recombination which we

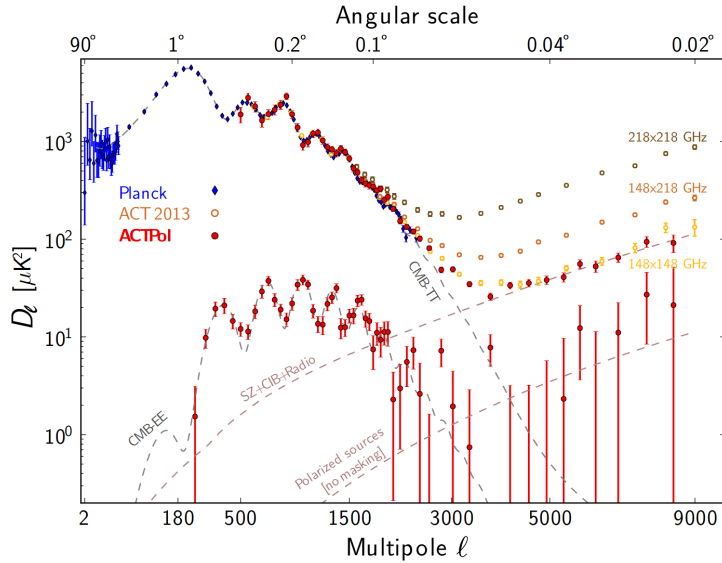


Figure 2.3: The Planck, ACT and ACTPol CMB temperature and polarization data. The grey dashed lines show the theoretical spectra. Figure taken from [59]

show in Section 2.2.3 one recovers the key features of the CMB spectrum which are the height of the acoustic peaks, the distance between acoustic peaks, the location of the first peak, the Sachs-Wolfe plateau and damping tail. Hence, the measurements of these features can give information on their dependency on the cosmological model. In other words measurements of the acoustic peaks can give constraints on the initial conditions and energy content of the universe. For example, precision measurements on the first acoustic peak suggests that the universe is flat, i.e. no curvature ($k=0$ in the field Friedmann equations) [60, 61].

Thompson scattering is expected to generate polarization of the CMB. Polarization signals can be described by their conventional Stokes parameters Q and U however in cosmology the CMB polarization is usually described with the scalar E-mode and pseudo-scalar B-mode parameters [62]. The scalar E-mode polarization arises from the acoustic peaks in the density field and is sometimes referred to as acoustic polarization. This symmetry can be seen in Figure 2.3 as the EE power spectrum follows the shape of the temperature power spectrum TT, be it out of phase and lower in amplitude by a factor of about ten as expected from the process of Thompson scattering [63]. The symmetry occurs in the absence of the BB signal which makes measurements of this signal an area of great interest in physics. The

BB polarization signal can be induced by gravitational waves in the primordial universe and a detection of the BB signal in the CMB signal will provide evidence for primordial gravitational waves.

2.2.2 Cosmological Matter Power Spectrum

The growth of structures in our universe can be attributed to gravitational instability. Regions with slight excess in the matter distribution of the early universe will eventually grow by the effect gravity to form the structure we see today. Our measurements of the LSS mainly constrain the distribution of matter in the current epoch. We can relate the potential of the matter distribution today to the primordial potential by

$$\Phi(\mathbf{k}, z) = \Phi_p(\mathbf{k})T(k)D(z) \quad (2.61)$$

where $\Phi_p(\mathbf{k})$ is the primordial gravitational potential of the universe, $T(\mathbf{k})$ is the transfer function and $D(z)$ is the growth function. The transfer function and growth function carry the scale dependent and epoch dependent information on the structure formation process which drives the primordial potential towards the observed potential. The transfer function is given as [52]

$$T(\mathbf{k}) = \frac{\Phi(\mathbf{k}, a_{\text{late}})}{\Phi_{\text{Large-Scale}}(\mathbf{k}, a_{\text{late}})}. \quad (2.62)$$

The growth function is $D(z) = a \frac{\Phi(a)}{\Phi(a_{\text{late}})}$ where $a = \frac{1}{1+z}$ describes the growth of the matter perturbations in the universe obtained from solving the evolution equation for the matter density contrast. At matter dominated times $D(a) \propto a$ is the scale factor of the universe. At later times when the effect of dark energy becomes more prevalent in the cosmic evolution, the growth function is altered in a more complicated way as the growth of structures becomes suppressed by the expansion of space. In this regime the growth function takes the form

$$D(a) = \frac{5\Omega_{m0}H_0^2H(a)}{2} \int_0^a da' [a'H(a')]^{-3}. \quad (2.63)$$

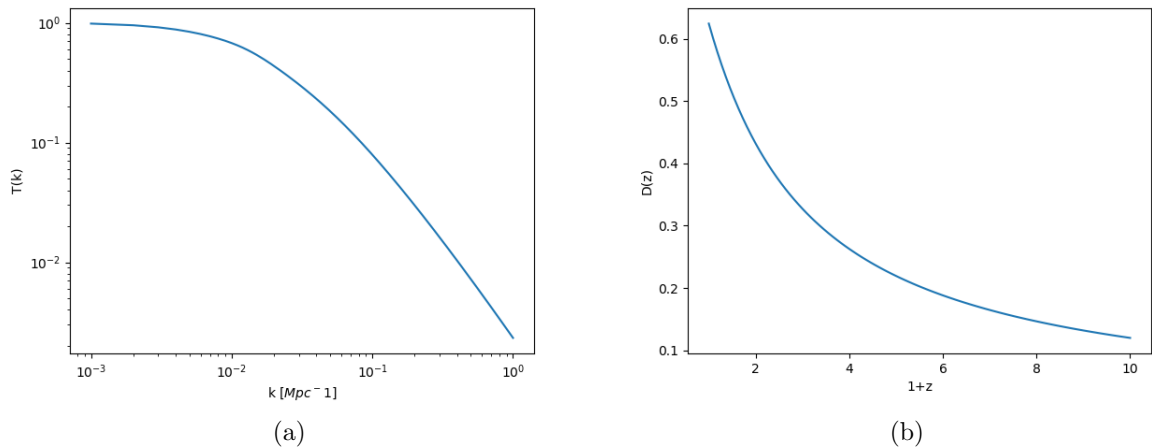


Figure 2.4: (a) The transfer function verse scale showing how the primordial fluctuations evolve in length scale. (b) Growth function verse redshift showing how the primordial fluctuations evolve in time. Plots produced using the Cosmology package.²

Solving for the potential we get [52]

$$\Phi(\mathbf{k}, z) = \frac{9}{10} \Phi_p(\mathbf{k}) T(k) D(z) (1+z). \quad (2.64)$$

In Figure 2.4 we show the transfer function and the growth function. The transfer function shows how the perturbation in the primordial universe evolves as a function of scale. The growth factor describes the growth of structures as a function of redshift and is defined to be unity for $z=0$.

In the case of CMB and LSS surveys the two point correlation function is used to probe the statistical nature of the distribution of quantities. The two point function in Fourier space gives the power spectrum. For example in the case of galaxy surveys, the two point correlation function gives the excess probability of finding two galaxies separated by a given distance scale. The two point correlation function can be written as

$$\xi(r) = \langle \delta(\mathbf{x}) \delta^*(\mathbf{x}') \rangle \quad (2.65)$$

²<http://roban.github.io/Cosmology/>

where here $\delta(x)$ would be any Gaussian random field and x would describe a positional vector. Here ξ depends on $r = |\mathbf{x} - \mathbf{x}'|$ due to statistical isotropy. Equivalently we can take the power spectrum in Fourier space as

$$\langle \delta(\mathbf{k})\delta^*(\mathbf{k}') \rangle = (2\pi)^3 \delta_D^3(\mathbf{k} - \mathbf{k}') P(k). \quad (2.66)$$

The angular brackets denotes the ensemble average and δ_D is the Dirac delta function which constrains $\mathbf{k} = \mathbf{k}'$. For the primordial matter power spectrum we relate the gravitational potential to density contrast using the Poisson equation

$$\Phi = 4\pi G \rho_m \frac{a^2}{k^2} \delta_m \quad (2.67)$$

where the matter density is $\rho_m = \Omega_m \rho_{crit}/a^3$ and $\rho_{crit} = (3/8\pi G)H_0^2$. This gives the matter density contrast as

$$\delta_m(\mathbf{k}, z) = \frac{3}{5} \frac{k^2}{H_0^2} \Phi_p(\mathbf{k}) T(k) D(z) \quad (2.68)$$

where the primordial potential is calculated as $\Phi_p(\mathbf{k}) = (50\pi^2/9k^3)(k/H_0)^{n-1} \delta_H^2 (\Omega_m/D(z))^2$ where δ_H is the amplitude at horizon crossing. For the above, a scale invariant solution with $n \approx 1$ [3] is usually considered and is referred to as the Harrison-Zel'dovich-Peebles spectrum [64, 22, 65]. Putting the above solutions together we get the theoretical matter power spectrum as

$$P_m(k, a) = 2\pi^2 \delta_H^2 \frac{k^n}{H_0^{n+3}} T^2(k) \left(\frac{D(a)}{D(a=1)} \right)^2 \quad (2.69)$$

We plot the primordial matter power spectrum in Figure 2.5. Non-linear effects cause the power spectrum to deviate from the linear approximation only at small scales.

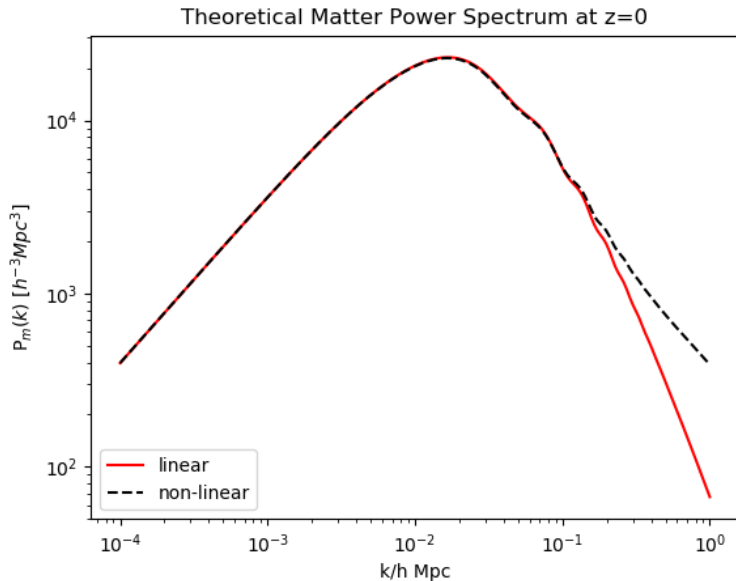


Figure 2.5: Theoretical matter power spectrum at $z = 0$, i.e. the primordial matter power spectrum. Black dashed lines show non-linear corrections to the matter power spectrum.

2.2.3 Baryonic Acoustic Oscillations

Here we provide a basic overview of baryonic acoustic oscillations. The acoustic peaks in the CMB temperature maps provide indirect evidence for the BAOs. We understand that prior to recombination the photons (or radiation field) and baryons were tightly coupled and therefore behaved as a single fluid. For this reason, the acoustic peak features we observe in the radiation field of the CMB are most likely to be imprinted on the matter density field. We now have evidence from galaxy surveys which gives evidence of the BAO scale in the matter distribution. We show the results from the SDSS survey in Figure 2.6 which gives evidence for the BAO scale which occurs around a $100h^{-1}Mpc$ spatial separation. The evidence shows up here as a ‘bump’ in the correlation function of the galaxy clustering. The BAO signal has also been measured and constrained by subsequent galaxy surveys [66] and further used to obtain cosmological parameters [67]. Studies have also been carried out to obtain model independent errors on the BAO using the SDSS’s Baryon Oscillation Spectroscopic Survey [68].

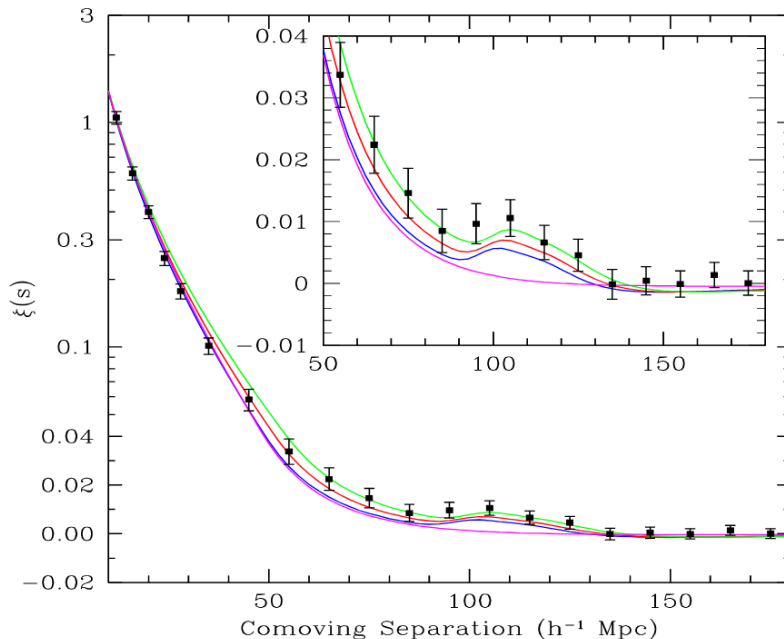


Figure 2.6: Evidence for the BAO length scale from the clustering of the SDSS LRG galaxy sample. The ‘bump’ in the correlation function at comoving separation of about $100 h^{-1} Mpc$ shows there exist a preferred clustering scale at this separation. Figure taken from [69]

We can obtain a simple model for the BAO scale by solving the basic fluid dynamic equations for the photon-baryon fluid prior to recombination [70]. Similar to the CMB temperature anisotropy case we decompose the field into its Fourier modes but we only look at the monopole term here

$$\Theta_{\ell=0,m=0}(\mathbf{x}) = \int \frac{d^3k}{(2\pi)^3} e^{i\mathbf{k}\cdot\mathbf{x}} \Theta(\mathbf{k}), \quad (2.70)$$

where we have left out the 00 subscript on the Fourier amplitude. The temperature perturbations in the Fourier space obey

$$\dot{\Theta} = -\frac{1}{3}k v_{\gamma}. \quad (2.71)$$

Here the derivative is with respect to conformal time. This equation is the usual continuity equation. We can also consider the Euler equation assuming pressure gradients supply the

only force [70]

$$\dot{v}_\gamma = k\Theta. \quad (2.72)$$

Differentiating the continuity equation and inserting the Euler equation we get the familiar form of a basic harmonic oscillator

$$\ddot{\Theta} + c_s^2 k^2 \Theta = 0, \quad (2.73)$$

where $c_s^2 = 1/3$ is the sound speed in the fluid. This equation indicates that the pressure gradient provides a restoring force to any initial perturbation in the fluid which then oscillates at the sound speed. To get a sense of the scales these corresponds to consider the fluid at recombination. A temperature variation of wavelength λ appears as an angular anisotropy of scale $\theta \approx \lambda/D$ where $D(z)$ is the angular diameter distance. For a flat universe, $D(\chi_{\parallel}^*) = \eta_0 - \eta_* \approx \eta_0$. In harmonic space this implies a series of acoustic peaks in anisotropy spectrum corresponding to

$$\ell_n \approx n\ell_a, \quad \ell_a \equiv \pi D(\chi_{\parallel}^*)/s_* \quad (2.74)$$

where $s = \int c_s d\eta \approx \eta/3$ is the distance sound can travel by η . To see how this simple model can give insight into where the oscillation features should be, consider a flat matter dominated universe $\eta \propto (1+z)^{-1/2}$ so that $\eta_*/\eta_0 \approx 1/30 \approx 2^\circ$ or equivalently $\ell \approx 200$. In any spatially curved universe the angular diameter distance does not equal the coordinate distance which means measurements of the position of the oscillation peak can constrain the curvature of the universe. Deviations of the position of the first peak from $\ell = 200$ would indicate a universe which is not spatially flat, however, thus far measurements on the acoustic peaks suggest a flat universe.

2.2.4 Redshift Space Distortions

All measurements of the sky are made in redshift space due to the expansion of the universe. Redshift space distortion (RSD) is the description of spatial distortions that are induced into the real space measurements by the redshift space observations. This effect and the modelling

for it was described by Kaiser in 1987 [71]. In Figure 2.7 we see the effect of RSD on the shape of an observed object. We see how a seemingly circular object or distribution can be flattened in the redshift space. We also see from Figure 2.7 how in the case of non-linear collapse the RSD effect can be so severe as to completely flip the opposing ends from the real space to the measured redshift space.

To understand this effect consider the simplest form for a galaxy's radial position out to a redshift z [52]

$$\chi_s(z) = \frac{z}{H_0} \quad (2.75)$$

where the subscript s denotes redshift space and $z \ll 1$. Redshift space then corresponds to assigning cartesian coordinates to a galaxy equal to

$$\mathbf{x}_s = \frac{z}{H_0} (\sin \theta \cos \phi, \sin \theta \sin \phi, \cos \theta). \quad (2.76)$$

Redshift space induces an apparent quadrupole moment in an otherwise circular overdensity. This means that redshift space distorts overdensities that we observe. As a region becomes more overdense the nature of the redshift space distortion changes. Thus, accounting for the redshift space distortion can be a tricky task. A qualitative treatment can be given as follows [71]. Firstly, we should note that the number of galaxies in a particular region is the same regardless of whether we use redshift space or real space coordinates. Therefore,

$$n_s(\mathbf{x}_s) d^3 x_s = n(\mathbf{x}) d^3 x \quad (2.77)$$

where n is the number density of galaxies. The volume element in redshift space is $d^3 x_s = dx_s^2 \sin \theta d\theta d\phi$ while for real space it is $d^3 x = dx x^2 \sin \theta d\theta d\phi$. The angular volume elements are identical so

$$n_s(\mathbf{x}_s) = n(\mathbf{x}) J \quad (2.78)$$

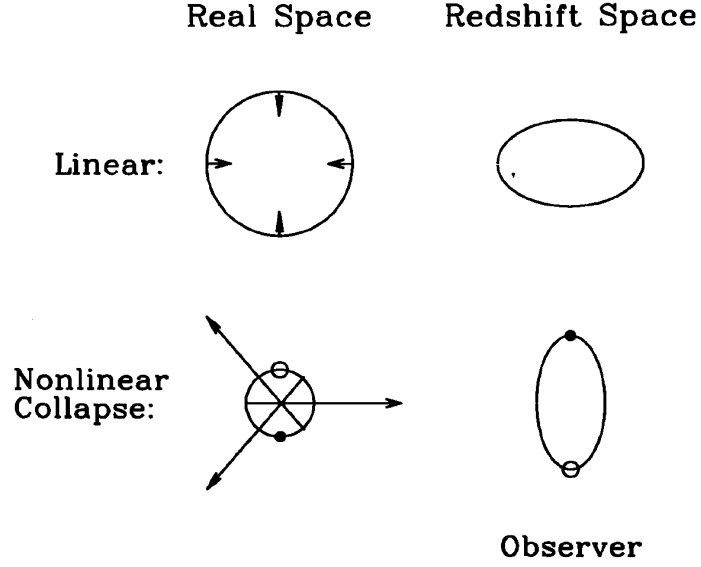


Figure 2.7: The redshift space distortion effect. In each case a circular contour of constant density is distorted in the redshift space. Figure taken from [52].

where J is the Jacobian given by

$$J \equiv \left| \frac{d^3x}{d^3x_s} \right| = \frac{dx}{dx_s} \frac{x^2}{x_s^2}. \quad (2.79)$$

To compute the Jacobian we use the definition of the observed redshift

$$z = H_0 x + \mathbf{v} \cdot \hat{x}. \quad (2.80)$$

The first term comes from Hubble's law and the second term is the velocity along the line of sight. Dividing Equation 2.80 by H_0 and using Equation 2.75 we obtain

$$x_s = x + \frac{\mathbf{v} \cdot \hat{x}}{H_0}. \quad (2.81)$$

The Jacobian then becomes

$$J = \left(1 + \frac{\partial}{\partial x} \left[\frac{\mathbf{v} \cdot \hat{x}}{H_0} \right] \right)^{-1} \left(1 + \frac{\mathbf{v} \cdot \hat{x}}{H_0 x} \right)^{-2}. \quad (2.82)$$

Real Space



Redshift Space



Figure 2.8: This figure shows how redshift space distortions can affect clustering and LSS experiments. In redshift space objects appear more squashed and the apparent overdensities appear to be much larger at the center than it is in real space, as viewed from the bottom of the page. Figure taken from [52].

Equation 2.82 can be further simplified following the treatment of Kaiser [71]. Kaiser realized that the correction term due to the derivative of the velocity is much more important than the $\mathbf{v} \cdot \hat{x}/H_0 x$ term. This is because for a plane wave perturbation, the term with the derivative of the velocity is of order $v'/H_0 \sim kv/H_0$, while the other correction is of order $v/H_0 x$. That is, the first correction term is larger than the second by a factor of order kx . This is generally the case since x is of order the size of the survey, while k is of order the Fourier modes we can hope to measure in the survey. Perturbations on the largest scale probed by the survey $k \sim x^{-1}$ are very poorly determined, since there are only a handful of Fourier modes with wavelength of order the survey size. Modes with smaller wavelength are much easier to measure since there are many such modes, and we effectively average over all of them to get an estimate of the power spectrum. Therefore, we are really interested only in modes with $kx \gg 1$. Expanding the remaining denominator about $v = 0$, we see that

$$J \simeq \left(1 - \frac{\partial}{\partial x} \left[\frac{\mathbf{v} \cdot \hat{x}}{H_0} \right] \right). \quad (2.83)$$

The number densities in real and redshift space is given as $n = \bar{n}(1 + \delta)$ and $n_s = \bar{n}(1 + \delta_s)$ respectively and \bar{n} is the average number density. With the aid of Equation 2.78 we then get

$$1 + \delta_s = [1 + \delta] \left(1 - \frac{\partial}{\partial x} \left[\frac{\mathbf{v} \cdot \hat{x}}{H_0} \right] \right). \quad (2.84)$$

Expanding this result to first order shows us that the overdensity in redshift space is just the sum of the overdensity in real space and a correction for peculiar velocity,

$$\delta_s(\mathbf{x}) = \delta(\mathbf{x}) - \frac{\partial}{\partial x} \left[\frac{\mathbf{v}(\mathbf{x}) \cdot \hat{x}}{H_0} \right]. \quad (2.85)$$

Now using the distant observer approximation, which says that the direction vector \mathbf{x} is fixed, and transforming to Fourier space we get

$$\delta_s(\mathbf{k}) = [1 + f\mu_k^2]\delta(\mathbf{k}), \quad (2.86)$$

where the linear velocities are $\mathbf{v}(\mathbf{k}) = ifH_0\delta(\mathbf{k})\frac{\mathbf{k}}{k^2}$, f is the linear growth rate and $\mu_k = \frac{k_{\parallel}}{k}$ [52]. The linear growth rate f is related to the growth function by $f = d \log D(a)/d \log a$. We use the parametric form $f(z) = \Omega_M^{\gamma}(z)$ for the growth rate, where $\Omega_M^{\gamma}(z)$ is the matter density parameter as a function of redshift and $\gamma \approx 0.55$ for the Λ CDM model [72].

In Figure 2.8 we see how the RSD effect can affect clustering measurements by inducing an apparent clustering in some measurements about the central point. This kind of induced squashing of the matter distribution can adversely affect our LSS results if we had not considered it in our modelling.

2.2.5 Gravitational Lensing

According to general relativity, light rays can be influenced by a gravitational potential. This phenomena whereby light rays are deflected by a massive object that lies along the trajectory of the photons is referred to as gravitational lensing. We show a schematic diagram of the gravitational lensing process in Figure 2.9 which shows how distance objects can appear distorted or lensed by a gravitational lens which lies along the line of sight between the source and the observer. Gravitational lensing provides astronomers with a powerful tool for observing our universe. One application of the lensing effect is to use strong gravitational objects as a magnifying lens to observe the distant universe. In the cosmological context, gravitational lensing can be used to constrain the large scale structure distribution. Since

light is deflected by intervening matter, measuring the gravitational lensing of distant galaxies or the CMB can provide us with information on the matter distribution along the line of sight [73, 74, 75]. Here we discuss the theoretical description of a lensed photon by a gravitational potential well.

The deflection angle of a photon which is being influenced by a gravitational potential in a flat universe is given by [76, 77]

$$\boldsymbol{\alpha} = -2 \int_0^{\chi_{\parallel}^*} d\chi \frac{\chi_{\parallel}^* - \chi_{\parallel}}{\chi_{\parallel}^*} \nabla_{\perp} \Psi(\chi_{\parallel} \hat{\mathbf{n}}, \eta_0 - \chi_{\parallel}) \quad (2.87)$$

where $\Psi(R)$ is the gravitational potential and $\eta_0 - \chi_{\parallel}$ represents the conformal time at which the photon was at position $\chi_{\parallel} \hat{\mathbf{n}}$. In the equation above, $\nabla_{\perp} \Psi$ defines the gradient of the potential. As discussed previously, χ_{\parallel}^* is the comoving distance to the last scattering surface. The derivative of the deflection angle defines a magnification matrix [78]

$$A_{ij} = \delta_{ij} + \frac{\partial \alpha_i}{\partial x_j} = \begin{pmatrix} 1 - \kappa - \gamma_+ & -\gamma_{\times} \\ -\gamma_{\times} & 1 - \kappa + \gamma_+ \end{pmatrix}. \quad (2.88)$$

The convergence field is defined as $\kappa = \frac{1}{2} \nabla \cdot \boldsymbol{\alpha}$. The components of shear, given by

$$\gamma_+ = \frac{1}{2} \left(\frac{\partial^2 \psi}{\partial x_1^2} - \frac{\partial^2 \psi}{\partial x_2^2} \right) \quad \text{and} \quad \gamma_{\times} = \frac{\partial^2 \psi}{\partial x_1 \partial x_2}, \quad (2.89)$$

determines the shape of a source at different axes due to the influence of tidal gravitational forces. Here x_1 and x_2 defines the two component coordinate system of the image axes. The lensing potential is defined such that $\boldsymbol{\alpha} = \nabla \psi$. The convergence field $\kappa = \frac{1}{2} \nabla \cdot \boldsymbol{\alpha} = \frac{1}{2} \nabla^2 \psi$ encodes the effects of gravitational lensing and can be described in terms of the integrated projection of the matter density [79, 80]

$$\kappa(\boldsymbol{\theta}) = \int d\chi_{\parallel} W_{\kappa}(\chi_{\parallel}) \delta_m(\mathbf{r}; z) \quad (2.90)$$

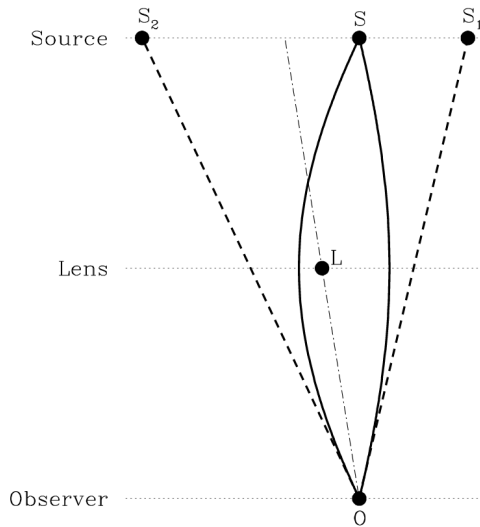


Figure 2.9: Schematic representation of gravitational lensing of a distant source S by some intervening lens L . We see the lens causes light rays traveling to us from the source to be deflected resulting in the formation of two images S_1 and S_2 . Figure taken from [81].

where $\mathbf{r} = [\chi_{\parallel}\boldsymbol{\theta}, \chi_{\parallel}]$ and the lensing kernel is

$$W_{\kappa}(\chi_{\parallel}) = \frac{3}{2}\Omega_{m0} \left(\frac{H_0}{c}\right)^2 \chi_{\parallel}^2 \left(\frac{\chi_{\parallel}^* - \chi_{\parallel}}{\chi_{\parallel}^*\chi_{\parallel}}\right) (1+z). \quad (2.91)$$

This expression for the convergence field describes the total integrated sum of the matter density contrasts from the last scattering surface to us today.

Cross-correlating different lensing probes such as CMB lensing maps and galaxy lensing surveys are also very useful providing constraints on the lensing biases [82]. Galaxy lensing measurements can also be used to constrain dark energy [83]. In Chapter 4 we study the cross-correlation of the 21cm signal with the CMB lensing convergence field. The CMB lensing convergence is deflected by the large scale structure between the surface of last scattering and us today. For this reason CMB lensing surveys provides an excellent projected tracer of the matter distribution of the universe.

Chapter 3

21cm Intensity Mapping

In this chapter we introduce the 21cm signal from neutral hydrogen (HI) which presents a new probe to measure the LSS of the universe. We compute the power spectrum for the 21cm signal and thereafter discuss the HIRAX [41] experiment which is currently being built to measure the 21cm signal in the 400-800 MHz frequency band. We then forecast constraints for the HIRAX experiment focusing on BAO detectability and constraining the cosmological and HI model parameters. We also investigate the HIRAX sensitivity, focusing on the array layout optimisation and how this translates into a 21cm signal detection in the presence of astrophysical foreground contaminants.

Neutral hydrogen is the simplest atomic species and the most abundant. HI can be used to trace the underlying structure of the universe offering a 3D map of the global LSS through cosmic history [84]. The crucial phenomena which enables us to track the HI distribution is the spin-flip transition which the HI atom undergoes. The spin-flip transition occurs when an electron and proton of an HI atom are bound in the unfavourable configuration with their intrinsic spins aligned. This configuration of the HI atom happens to be at a higher energy level than if the electron and proton were bound together with their spins in the opposite direction. Therefore an electron in an HI atom may undergo a spin-flip to allow the lower energy configuration of the atom and this process releases a 21cm signal. In reality the 21cm

emission line of hydrogen is a ‘forbidden’ transition which means the probability of a 21cm emission from an individual atom is quite low. However, given the sheer abundance of the hydrogen atom in the universe we have a statistically favourable chance of detecting the 21cm emission. The 21cm emission has been directly detected in nearby galaxies [85, 86].

The 21cm intensity mapping (IM) technique has a wide range of advantages over conventional galaxy surveys and for this reason HI surveys are generating a large interest in the cosmological community. The 21cm signal can allow us to accurately measure scales which were previously inaccessible [87]. CMB and galaxy surveys mainly probe the very early or late universe respectively. With 21cm surveys we can observe a large period in the cosmic history of the universe since HI has been around since the recombination era. These surveys also makes much faster measurements of large portions of the sky since we are not required to resolve individual objects.

There is currently a wide range of next generation 21cm experiments around the world, either in preparation or currently online around to measure the 21cm signal such as the SKA [38], MeerKAT [88], CHIME [89], HIRAX [41], BINGO [90] and Tianlai [42]. The first successful application of HI intensity mapping was done by cross-correlating the Green Bank Telescope 21cm maps with the DEEP2 optical galaxy surveys [48].

One of the major challenges facing 21cm IM surveys will be recovering the cosmological signal in the presence of the galactic and extragalactic foreground contamination [91]. These foregrounds are generally many orders of magnitudes larger than the 21cm signal but fortunately the foregrounds have smooth frequency dependence and can in principle be filtered out [92, 93, 94, 95, 96].

In this chapter we obtain a fair amount of new results on the 21cm intensity mapping ability of the HIRAX experiment. In Section 3.2 we show how the HIRAX experiment will be able to make a significant detection of the 21cm power spectrum quantified through the signal to noise estimate. In Section 3.3 we show how the high signal to noise ratio measurements can then be used to obtain tight constraints on the BAO signal and dark energy parameters. In Section 3.4 we show how the choice of the array layout can improve or hinder 21cm measurements. We also look at how the array layout affects the data rate, data volume,

calibration and foreground mitigation efforts.

3.1. Theoretical Model

In the Rayleigh-Jeans limit we can relate the intensity I_ν to a brightness temperature T_b by [87]

$$I_\nu = \frac{2k_B}{c} T_b \nu^2 \quad (3.1)$$

where as before c is the speed of light and k_B is the Boltzmann's constant. The 21cm brightness temperature can be expressed as [97]

$$T_b(z) = \frac{T_{\text{EX}} - T_{\text{CMB}}}{1+z} (1 - e^{-\tau_{21}}) \quad (3.2)$$

where T_{EX} is the excitation temperature of the spin-flip transition, also referred to as the spin temperature. T_{CMB} is the background temperature of the CMB which pervades the universe and τ_{21} is the 21cm optical depth which describes the scattering of 21cm photons by intervening electron clouds given by

$$\tau_{21} = \frac{3\hbar c^3}{16k_B \nu_{21}^2} \frac{x_{\text{HI}} n_{\text{H}}}{T_{\text{EX}} (dv_{\parallel}/d\chi_{\parallel}) (1+z)} \quad (3.3)$$

where x_{HI} is the fraction of HI and n_{HI} is their number density. The $dv_{\parallel}/d\chi_{\parallel}$ function describes the gradient of the velocity field along the line of sight χ_{\parallel} . In principle one can estimate the global 21cm signal using a spherically averaged brightness temperature which can be approximated as [36]

$$\bar{T}_b(z) \approx 566h \left(\frac{H_0}{H(z)} \right) \left(\frac{\Omega_{\text{HI}}(z)}{0.003} \right) (1+z)^2 \quad (3.4)$$

where $\Omega_{\text{HI}}(z)$ is the HI density contrast parameter as a function of redshift.

In statistical studies, the quantity of interest is the brightness temperature fluctuations or contrast. To get an expression for the brightness temperature fluctuation of the 21cm signal

we first consider the HI density fluctuations which we define as a biased tracer of the matter fluctuations

$$\delta_{HI}(\mathbf{k}, z) = (b_{HI}(z) + f(z)\mu_k^2) \delta_m(\mathbf{k}, z) \quad (3.5)$$

where b_{HI} is the HI bias term which quantifies how HI traces the matter density and we take into consideration the RSD term discussed in Section 2.2.4. The HI bias is given as [98]

$$b_{HI}(z) = \frac{\int_{M_{min}}^{M_{max}} dM M \frac{dn}{dM} b(M, z)}{\int_{M_{min}}^{M_{max}} dM M \frac{dn}{dM}} \quad (3.6)$$

where M_{min} and M_{max} are the lower and upper limits of the masses and $b(M, z)$ is the halo bias. We now calculate the 21cm brightness temperature fluctuations by converting the density fluctuations into a temperature estimate by multiplying the density field with the 21cm mean brightness temperature

$$\delta T_{21}(\mathbf{k}, z) = \bar{T}_b(z) \delta_{HI}(\mathbf{k}, z) = \bar{T}_b(z) (b_{HI}(z) + f(z)\mu_k^2) \delta_m(\mathbf{k}, z). \quad (3.7)$$

With the expression for the 21cm brightness temperature fluctuations in Equation 3.7 we are now in a position to compute the 21cm brightness temperature power spectrum which we discuss in the next section.

3.1.1 The 21cm Power Spectrum

Like in CMB studies we can extract a wealth of information on the statistics of the large scale universe from a power spectrum for the 21cm signal. We will compute the 21cm signal in some comoving volume element cube which we center at some point and choose our bins fine enough that the signal is mostly constant in the given volume element. In this formalism the 21cm signal we compute will have some value centered at co-ordinates (z_i, θ_i) which accounts for the radial and angular position of the volume element.

We can now express the 21cm intensity signal in observational coordinates, in some comoving volume centered at redshift z_i , with width Δz_i corresponding to a frequency range

$\Delta\tilde{\nu}_i$, in the flat sky as [36]

$$\delta T_{21}(\boldsymbol{\ell}, y; z_i) = \int d^2\theta d\tilde{\nu} e^{-i(\boldsymbol{\ell}\cdot\boldsymbol{\theta}+y\tilde{\nu})} \delta T_{21}(\boldsymbol{\theta}, \tilde{\nu}; z_i). \quad (3.8)$$

Note that $\tilde{\nu} = 1/(1+z)$ varies over the width of the bin and need not correspond to the central redshift z_i . The radial modes y are defined such that $y = c(\tilde{\nu}_p - \tilde{\nu}_i)(1+z_i)^2/H(z_i) = r_\nu(z_i)(\tilde{\nu}_p - \tilde{\nu}_i)$ where $\tilde{\nu} = \nu/\nu_{21} = 1/(1+z)$. Here ν_p denotes the frequency values varying in the volume and ν_i is the frequency corresponding to the central redshift. It is clear that y defines the radial modes because it decomposes the frequency direction which in 21cm measurements represents the distance to a given object or basically the radial direction to a given point in the universe. Decomposing the 21cm intensity field into plane waves in the comoving volume (where $\mathbf{r} = [\chi_{\parallel,i}\boldsymbol{\theta}, \chi_{\parallel,i}]$), and simplifying, gives

$$\delta T_{21}(\boldsymbol{\ell}, y; z_i) = \frac{1}{V_p(z_i)} \delta T_{21}(\mathbf{k}; z_i) \quad (3.9)$$

where we have defined the comoving volume factor as $V_p(z_i) = \chi_{\parallel,i}^2 r_{\nu,i}$ which converts the physical field into the observable field. In Equation 3.9 we have explicitly defined the relation of the Fourier wavenumbers to the observational harmonic space radial and angular wavenumbers $\mathbf{k}_\perp = \boldsymbol{\ell}/\chi_{\parallel,i}$ and $k_\parallel = y/r_{\nu,i}$.

We now define the HI angular power angular spectrum as a function of angular and radial wavenumbers as

$$\langle \delta T_{21}(\boldsymbol{\ell}, y; z_i) \delta T_{21}^*(\boldsymbol{\ell}', y'; z_i) \rangle = (2\pi)^3 \delta_D^2(\boldsymbol{\ell} - \boldsymbol{\ell}') \delta_D(y - y') C_{\ell,S}^{21}(y; z_i), \quad (3.10)$$

which we compute to get

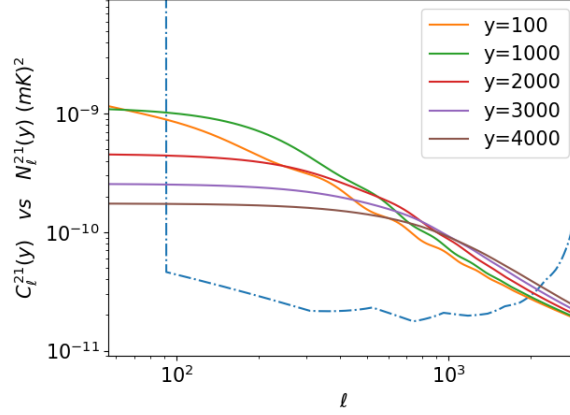


Figure 3.1: The 21cm power spectra for various y modes vs ℓ . The blue dot-dashed curve shows the HIRAX interferometer noise which we discuss in Section 3.2. From the plot we can see that the HIRAX experiment will be able to make a significant detection of the 21cm signal where the HIRAX noise is minimized which happens at the most relevant scales for the BAOs ($\ell \sim 100 - 1500$).

$$\begin{aligned}
C_{\ell,S}^{21}(y; z_i) &= \int \frac{d^2\ell'}{(2\pi)^2} \int \frac{dy'}{(2\pi)} \langle \delta T_{21}(\ell, y; z_i) \delta T_{21}^*(\ell', y'; z_i) \rangle \\
&= \int \frac{d^2\ell'}{(2\pi)^2} \int \frac{dy'}{(2\pi)} \bar{T}_b^2(z_i) (b_{HI}(z_i) + f(z_i)\mu_k^2)^2 \frac{D^2(z_i)}{V_p^2(z_i)} \langle \delta_m(\mathbf{k}, z=0) \delta_m^*(\mathbf{k}', z=0) \rangle \\
&= \bar{T}_b^2(z_i) (b_{HI}(z_i) + f(z_i)\mu_k^2)^2 \frac{D^2(z_i)}{V_p^2(z_i)} \int \frac{d^2k'_\perp}{(2\pi)^2} \int \frac{dk'_\parallel}{(2\pi)} V_p(z_i) \delta_D^3(\mathbf{k} - \mathbf{k}') P_m(k, z=0) \\
&= \bar{T}_b^2(z_i) (b_{HI}(z_i) + f(z_i)\mu_k^2)^2 D^2(z_i) \frac{P_m(k; z=0)}{V_p(z_i)} = \frac{P_{21}(k; z_i)}{V_p(z_i)}.
\end{aligned} \tag{3.11}$$

Here we have used the growth function $D(z)$ to remove the redshift dependence on the matter power spectrum and defined $P_{21}(k; z_i) = \bar{T}_b^2(z_i) (b_{HI}(z_i) + f(z_i)\mu_k^2)^2 D^2(z_i) P_m(k; z=0)$. The 21cm power spectrum will have to be measured in the presence of foreground contamination and some instrumentation noise. We discuss the foreground signal in Section 3.1.2. In Section 3.2 we discuss the HIRAX interferometer noise contribution which limits our survey sensitivity. In Figure 3.1 we show the computed 21cm power spectrum shown in Equation 3.11 and we show the HIRAX interferometric noise model which we describe in Section 3.2. We see that the HIRAX experiment will be able to make a significant detection of the 21cm signal where the HIRAX noise is minimized. The scales on which the HIRAX noise drops

below the signal is where we expect to make our best measurements and we can see how the design specifications of HIRAX ensure these scales are where the BAO signals reside in the 21cm power spectrum. This corresponds to the range $\ell \sim 100 - 1500$ in Figure 3.1 where the HIRAX noise is lowest and the wiggles in the 21cm power spectrum from the BAO feature is visible. We quantify the actual constraint on the BAO parameters this detection will provide in Section 3.3.

3.1.2 Foregrounds

A major challenge facing HI 21cm surveys are the astrophysical foregrounds which contaminate radio measurements of the sky. The main types of foreground contaminants are thought to be from galactic synchrotron, galactic free-free, extragalactic diffuse free-free and extragalactic point source emissions. These foreground signals can be up to 6 orders of magnitudes larger than the cosmological 21cm signal [95]. In Figure 3.2 we see how the 21cm signal is significantly smaller than the various foreground components. Even though the 21cm signal may be much smaller in magnitude than the foregrounds, a key feature of the foreground signal is that it is expected to be smoothly varying in frequency as opposed to the 21cm signal. This means we can effectively separate these signals. Modelling and removing the foreground contamination has been studied using many different methods and techniques [91, 94, 99, 100].

The foreground signal is usually modelled as a power law function of the form [99]

$$C_\ell^F = A \left(\frac{1000}{\ell} \right)^\beta \left(\frac{\nu_f}{\nu} \right)^{2\alpha} \quad (3.12)$$

where $\nu_f = 130\text{MHz}$, A and β are parameters that define the type of foreground emission and α is the spectral index. In Table 3.1 we show the foreground parameters discussed in [99]. Figure 3.2 shows the various foreground model signals and how they dwarf the 21cm signal in amplitude. A clear understanding of the various foreground models and the characterization of our instrument is vital if we hope to efficiently extract a cosmological signal. If we lack a decent understanding of our instrument it can cause a leakage of foreground contaminant

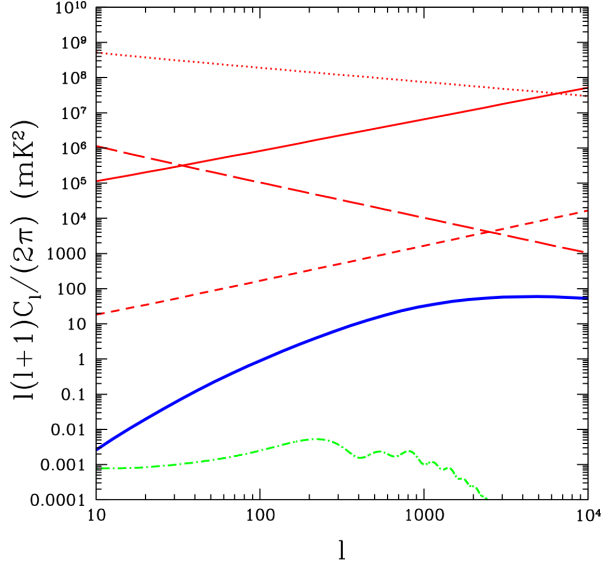


Figure 3.2: The 21cm signal (blue) versus the foreground models as modelled in Eq 3.12 using the foreground parameters specified in Table 3.1. The red dotted line represents the galactic synchrotron emission signal, the red solid line is the point sources, the red long dashed line galactic free-free emission and the red short dashed line is the extragalactic free-free. The green curve shows the CMB signal level for comparison. Figure from [99].

into the 21cm signal unbeknown to us. This can then force foreground power into our 21cm signal giving incorrect results.

	$A(\text{mK})^2$	α	β
Extragalactic point sources	57	1.1	2.07
Extragalactic free-free	0.0014	1.0	2.10
Galactic synchrotron	700	2.4	2.80
Galactic free-free	0.088	3.0	2.15

Table 3.1: Fiducial foreground parameters at $\ell = 100$ and $\nu = 130$ MHz for the various foreground sources, taken from [99].

For the purpose of this work, we assume all measurements have undergone some efficient foreground cleaning method at a cost of removing slowly varying frequency modes. This means we expect to lose some of the cosmological signal at the low radial wavenumbers $y < y_{FG}$. For the modes which are lost in foreground subtraction we consider the low-cut from [36]. Here they assume that the smooth variation of the foregrounds in frequency is difficult to separate from cosmological modes on scales comparable to the total survey

bandwidth, $k_{FG} \sim 1/(r_\nu \Delta \tilde{\nu}_{tot})$. The corresponding value for the minimum cut of radial modes for the HIRAX experiment corresponds to about $k_{FG} \sim 0.01 \text{ Mpc}^{-1}$.

3.2. The HIRAX Survey

Here we discuss the Hydrogen Intensity and Real-time Analysis eXperiment (HIRAX) which is a planned HI intensity mapping experiment to be located at the SKA site in the Karoo, South Africa [41]. HIRAX will be a 1024 6m dish interferometer array which will observe the HI signal in the 400-800 MHz frequency band which corresponds to redshift of about $z \approx 0.755 - 3.5$. HIRAX will map the universe using the BAO as a standard ruler to constrain the nature of dark energy as a function of time. These measurements can then be turned into tight constraints on the dark energy EOS parameters. We show the HIRAX survey strategy details in table 3.2.

Experiment	HIRAX
$S_{area} [\text{deg}^2]$	15000
$T_{obs} [\text{years}]$	4
Redshift range	0.755-2.55
$T_{inst} [\text{K}]$	50
N_{dish}	1024
$D_{dish} [\text{m}]$	6
$D_{min} [\text{m}]$	6
$D_{max} [\text{m}]$	270

Table 3.2: Experimental specifications for HIRAX.

In radio astronomy we require instruments which can efficiently measure the cosmological signals of interest. As we seek to measure larger wavelength signals we require larger dish sizes to obtain more angular resolution. This naturally leads to a problem whereby we may require to build a single dish telescope too large for all practical purposes. This is where radio interferometry can improve the angular resolution. Interferometry works by measuring a signal using two smaller dishes separated by some distance. The separation from dish center to dish center is referred to as a baseline. In radio interferometry we make measurements of

the sky with the given baselines of some array configuration. This means that we can measure really large wavelength signals with a number of small dishes with some large separation.

The visibility measured by an interferometer is simply the cross-correlation of the electric field measured on the sky between antennas [101]

$$V_{ij}(\nu) = \int d^2\theta \langle A_i(\boldsymbol{\theta}, \nu) E(\boldsymbol{\theta}, \nu) A_j^*(\boldsymbol{\theta}, \nu) E^*(\boldsymbol{\theta}, \nu) e^{-2\pi i[(r_i - r_j)\nu/c] \cdot \boldsymbol{\theta}} \rangle \quad (3.13)$$

where $E(\boldsymbol{\theta}, \nu)$ is the actual sky electric field and $A_i(\boldsymbol{\theta}, \nu)$ is the electrical sensitivity of the i^{th} antenna. The quantity $r_i - r_j$ is the physical separation of the two antennas and is the given baseline between those antennas. We can simplify Equation 3.13 by using the fact that $\langle EE^* \rangle$ just gives the intensity or brightness I and $\langle AA^* \rangle$ gives the the antenna power sensitivity or antenna beam pattern B . Therefore, we can write the visibility as

$$V_{ij}(\nu) = \int d^2\theta I(\boldsymbol{\theta}, \nu) B(\boldsymbol{\theta}, \nu) e^{2\pi i \mathbf{u}_{ij}(\nu) \cdot \boldsymbol{\theta}} \quad (3.14)$$

where $\mathbf{u}_{ij}(\nu) = (r_i - r_j)\nu/c$ is just the spatial separation of any two antennas in wavelength units.

Most experimental instruments have some intrinsic noise that contributes to the final measurements. The noise term for interferometer experiments comes from the response towards the sky measurements which depends on the survey parameters and importantly the array layout configuration. For a given measured visibility along some baseline $|u| = D/\lambda$ we have the apparent sky intensity as [50]

$$\sigma_T^2 = \frac{\langle |V(\ell/2\pi)|^2 \rangle}{n(\ell/2\pi) d^2u} \quad (3.15)$$

where the variance per visibility is $\langle |V(\ell/2\pi)|^2 \rangle = [\lambda^2 T_{sys}^2 / A_e \sqrt{\Delta\nu t_p}]^2$. We now approximate the noise power spectrum for an interferometer by using $d^2u \sim 1/FOV$ and relating the visibility to a noise power spectrum

$$C_{\ell, N}^{21}(y; z_i) = \langle N_\ell N_\ell^* \rangle \approx (\delta\nu/\nu_{21}) \sigma_T^2 \quad (3.16)$$

to obtain [36]

$$C_{\ell,N}^{21}(y; z_i) = \frac{T_{\text{sys}}^2(\tilde{\nu}_i) \text{FOV}(\tilde{\nu}_i) 4\pi}{\nu_{21} n_{\text{pol}} N_b t_{\text{tot}} n(\mathbf{u} = \ell/2\pi)}, \quad (3.17)$$

where the pointing time is just $t_p = t_{\text{tot}} S_{\text{area}} / \text{FOV}$, A_e is the effective dish area and the bandwidth is $\Delta\nu$. The system temperature is given as $T_{\text{sys}} = T_{\text{inst}} + T_{\text{sky}}$, where $T_{\text{sky}} \approx 60K \left(\frac{\nu_i}{300 \text{ MHz}}\right)^{-2.5}$. The function $n(u)$ is the baseline density function in uv co-ordinates. The baseline density function for an interferometer experiment sets the scales to which the experiment is sensitive since $u = \frac{D}{\lambda}$ where D is the physical length of the baselines. Therefore, for an experiment with a given maximum and minimum baseline we get the scales which is accessible as $D_{\text{min}} = \lambda u_{\text{min}}$, $D_{\text{max}} = \lambda u_{\text{max}}$. In the above expression we have also included for the sake of generality the proportionality of the noise spectrum on the number of beams N_b and number of polarizations of the antenna feeds n_{pol} . We use $S_{\text{area}}/f_{\text{sky}} = 4\pi$ since we find it more convenient to set $f_{\text{sky}} = 1$ in the noise expression above, i.e., consider the full sky noise, and to include the f_{sky} factor in the SNR expression when doing the mode counting on a smaller patch of sky. Note that the number of ℓ modes decreases to $f_{\text{sky}}(2\ell + 1)$ on a smaller patch of the sky.

To quantify the signal detection by a given experiment one can compute the signal to noise ratio (SNR). Here we compute the SNR for the modelled HIRAX noise vs the theoretical signal model. The SNR is calculated by

$$(\text{SNR})^2 = 0.5 (\Delta\tilde{\nu}_i S_{\text{area}}) \int_{y_{\text{min}}}^{y_{\text{max}}} \frac{dy}{(2\pi)} \int_{\ell_{\text{min}}}^{\ell_{\text{max}}} \frac{d\ell}{(2\pi)} \ell \left[\frac{C_{\ell,S}^{21}(y; z_i)}{C_{\ell,S}^{21}(y; z_i) + C_{\ell,N}^{21}(y; z_i)} \right]^2. \quad (3.18)$$

This equation estimates the statistical detection expected given some intrinsic noise term associated with the HIRAX experiment. In Figure 3.3 we show the SNR per pixel for 4 redshift bins in the HIRAX range computed in the $k_{\perp} - k_{\parallel}$ plane. We compute the SNR integral by subdividing the total $k_{\perp} - k_{\parallel}$ plane into 15 bins in each direction of width $\Delta k = 0.01 \text{ Mpc}^{-1}$ and computing the SNR in each bin. We can see in Figure 3.3 that the HIRAX experiment will be able to access many modes with high sensitivity measurements, with cumulative signal-to-noise values of around 800. This can be translated into very high precision

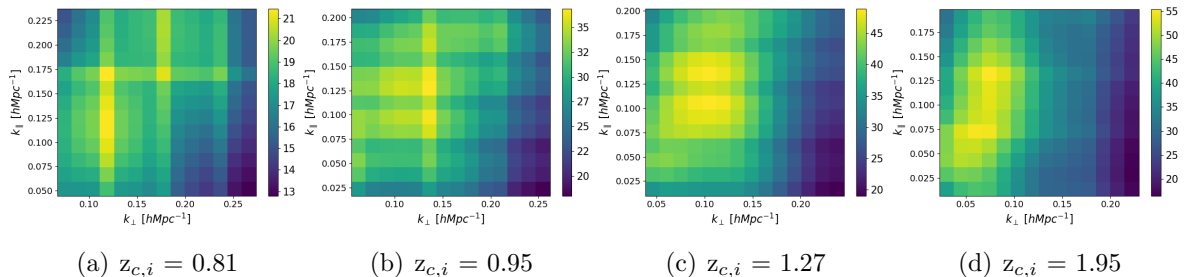


Figure 3.3: HI SNR in k_{\parallel} and k_{\perp} bins of width 0.01 Mpc^{-1} for all four redshift bins. We see how the HIRAX experiment is designed to maximize the SNR at the scales most important for BAO measurements.

measurements on the BAO signal as well as be turned into tight parameter constraints which we show in Section 3.3. We see how interferometer experiments will be restricted to the scales that are accessible due to the baseline lengths and the foreground limits. We also restrict our analysis to only the linear regime where we have a good understanding of the physical processes. We list below a summary of accessible scales for the HIRAX experiment

$$\begin{aligned}
 \ell_{min} &= 2\pi u_{min} = 2\pi \frac{D_{min}}{\lambda} \\
 \ell_{max} &= 2\pi u_{max} = 2\pi \frac{D_{max}}{\lambda}, \\
 y_{min} &= y_{FG} \sim \frac{1}{\Delta \tilde{\nu}_{tot}}, \\
 y_{max} &= y_{NL} = r_{\nu} k_{NL}.
 \end{aligned}$$

We take the non-linear scale to be $k_{NL} \sim 0.14 \text{ Mpc}^{-1}$.

3.3. HI Intensity Mapping BAO Constraints

In this section we transform our HIRAX signal detection estimates into constraints on the cosmological and HI model parameters. To obtain the expected errors on a given measured parameter we use the Fisher forecasting formalism. The Fisher formalism is based on a likelihood function which gives the expected measurements of an experiment for some associated underlying theory.

3.3.1 Fisher Formalism

The preferred method of parameter estimation in cosmological surveys is the maximum likelihood estimation. For some underlying theory and a given measurement the likelihood function can be simply stated as: what is the probability of making a given measurement on a parameter given some underlying theory

$$\mathcal{L} \equiv P[\text{data}|\text{theory}]. \quad (3.19)$$

A key quantity of interest here is the Fisher matrix which quantifies the expectation value of the likelihood function at a given data point. One way to intuitively understand the Fisher matrix is to consider a Taylor expansion of the likelihood function about the peak value up to second order. If we use x to represent some random distribution of our observed samples and x_0 is the value for x where the likelihood function peaks then we have

$$\mathcal{L}(x) \approx \mathcal{L}(x_0) + \frac{\partial \mathcal{L}}{\partial x}(x - x_0) + \frac{1}{2} \frac{\partial^2 \mathcal{L}}{\partial x^2}(x - x_0)^2. \quad (3.20)$$

In the above expression however, the linear term is zero since x_0 is a maximum point and hence the first derivative here vanishes. This essentially leaves us with a quadratic approximation for the likelihood function. In general the distribution of a likelihood function can be any function and not just quadratic. It is common practice to describe the likelihood as Gaussian since most fields of interest are assumed to be Gaussian and furthermore a Gaussian function helps visualize a spread and variance of some distribution about a point x_0 more intuitively. Therefore we take the Fisher matrix to be Gaussian by differentiating the natural log of the likelihood function instead (see [102] for a review). From here on for our forecasts we use the Fisher matrix in the form [103]

$$F_{\alpha\beta} = (\Delta\tilde{\nu}_i S_{\text{area}}) \int_{y_{\min}}^{y_{\max}} \frac{dy}{(2\pi)} \int_{l_{\min}}^{l_{\max}} \frac{dl}{(2\pi)^2} \ell (\partial_\alpha \ln X^{\text{tot}} \partial_\beta \ln X^{\text{tot}}) \quad (3.21)$$

where $X^{tot} = X^{Signal} + X^{Noise}$ and X^{Signal} is the signal spectra for a given probe with the corresponding noise or variance X^{Noise} . The inverse of the Fisher matrix gives the covariance matrix which contains the uncertainty or errors on the parameters.

We now turn our attention to the Fisher forecasts for the HI case. The 21cm power spectrum we computed in Equation 3.11 can be written explicitly as

$$C_l^{21}(y; z_i) = A_b^2(z_i) [b_{HI}(z_i)\Omega_{HI}^2(z_i) + f(z_i)\Omega_{HI}^2(z_i)\mu_k^2]^2 D^2(z_i) \left(\frac{\sigma_8}{\sigma_8^{fid}} \right)^2 \frac{P_m^{fid}(k, z=0)}{V_p(z_i)} \quad (3.22)$$

where we have defined $A_b(z) = \frac{566h}{0.003} \frac{H_0}{H(z)} (1+z)^2 \mu K$ such that we can write $\bar{T}(z) = A_b(z)\Omega_{HI}(z)$. For 21cm experiments the Ω_{HI} function is usually degenerate with most parameters since they enter the signal expression as a product. This means we actually measure a single quantity which is a product of various parameters and cannot differentiate the information on the individual parameters unless we have some external knowledge on some of the parameters. For this case where the parameters are combined or degenerate with each other we can either fix certain parameter values by assuming we have complete knowledge of it or we can combine parameters to obtain a combined constraint. In this work we combined Ω_{HI} into the bias and RSD growth function terms b_{HI} and f to get constraints on $b_{HI}\Omega_{HI}$ and $f\Omega_{HI}$. It is also worth pointing out that constraints on the RSD growth function can be made using a multipole expansion of the power spectrum [104].

The amplitude of the matter power spectrum σ_8 is defined as the normalization of the matter power spectrum

$$P_m(k) = \left(\frac{\sigma_8}{\sigma_8^{fid}} \right)^2 P_m^{fid}(k). \quad (3.23)$$

For 21cm IM surveys modelled in Equation 3.22 we can constrain the following set of parameters: $\{ A_{BAO}, \sigma_8, \Omega_{HI}b_{HI}, \Omega_{HI}f, \alpha_{\parallel}, \alpha_{\perp} \}$. Note that here we have dropped the explicit redshift dependence for brevity. It is necessary to vary as much of the parameters as we can to keep the forecasts realistic. Forecast constraints on all parameters can have some covariance between them meaning that uncertainty on one parameter propagates uncertainties into the others.

One can test the expansion of the universe and its geometry using the Alcock-Paczynski test [105]. This method evaluates the ratio of the observed angular size to radial/redshift size. The distance scale parameters α_{\parallel} and α_{\perp} are defined as [36, 106]

$$\alpha_{\perp} = \frac{\chi_{\parallel}^{fid}}{\chi_{\parallel}} = \frac{D_A^{fid}(z)}{D_A(z)}, \quad \alpha_{\parallel} = \frac{r_{\nu}^{fid}}{r_{\nu}} = \frac{H(z)}{H^{fid}(z)}. \quad (3.24)$$

Here the angular diameter distance and expansion rate $D_A(z)$ and $H(z)$ respectively measure the distance in the transverse and radial directions. To include constraints on the distance scales we replace $\ell \rightarrow \alpha_{\perp}\ell$ and $y \rightarrow \alpha_{\parallel}y$ and include the derivatives for $\alpha_{\perp}, \alpha_{\parallel}$ in our Fisher matrix. A common quantity of importance in studies of the distance scales is usually the distance volume scale which is a combination of $D_A(z)$ and $H(z)$. Many forecasts and survey measurements are done directly on the redshift dependent volume scale which is defined as [107]

$$D_V(z) = \left((1+z)^2 D_A^2 \frac{cz}{H(z)} \right)^{\frac{1}{3}}. \quad (3.25)$$

We can see that the distance volume scale in Equation 3.25 does in fact describe a volume element as a function of redshift and serves as a tracer of the volume expansion through cosmic time.

To include constraints on the amplitude of the BAO wiggles we follow the details outlined in [36] based on the approach by [106]. Firstly we have to define the BAO wiggle function by separating the matter power spectrum into a smooth part and the oscillatory part

$$f_{bao}(k) = \frac{P(k) - P_m^{smooth}(k)}{P_m^{smooth}(k)}. \quad (3.26)$$

We then have to define the parameter A_{bao} to quantify the amplitude of fluctuations such that

$$P(k) = [1 + A_{bao}f_{bao}(k)] P_m^{smooth}(k). \quad (3.27)$$

Therefore, constraints on A_{bao} can account for the errors on the BAO fluctuation amplitudes. Here P_m^{smooth} represents the smooth matter power spectrum which has the oscillatory part

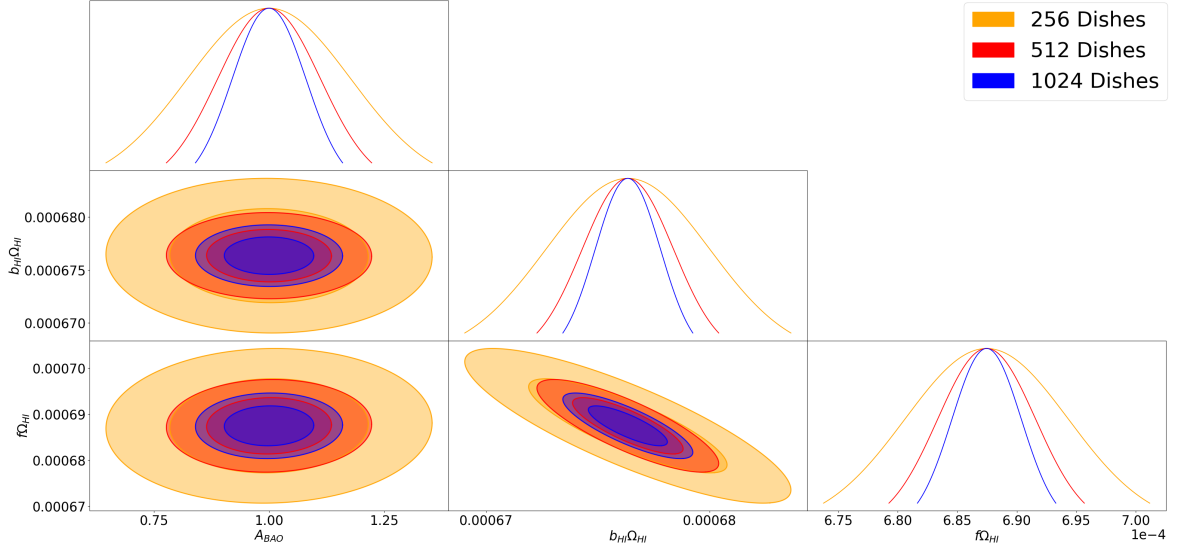


Figure 3.4: Forecast constraints on the HI model parameters in the $z_i = 1.27$ redshift bin. We show here the comparative constraints from the HIRAX experiments for 256, 512 and 1024 dish stages. Here we have fixed σ_8 since it is degenerate with the other parameters but show in Chapter 4 how we can break the degeneracy with cross-correlation.

removed in any arbitrary way. From Equation 3.21 we see that for constraints on a given parameter we have to compute the derivatives of the probe with respect to each of the parameters we varying. Consider a given parameter p_α for which we compute the derivative as

$$\partial_{p_\alpha} \ln X^{tot} = \partial_{p_\alpha} \ln (X^{Signal} + X^{Noise}). \quad (3.28)$$

Here it must be pointed out that the noise terms of surveys are usually independent of the parameters. In other words the parameters we are constraining from the cosmological surveys only enter through the contributions of the signal terms. Therefore we get the Fisher matrix derivatives as

$$\partial_{p_\alpha} \ln X^{tot} = \frac{\partial_{p_\alpha} X^{Signal}}{(X^{Signal} + X^{Noise})} = \frac{\partial_{p_\alpha} X^{Signal}}{X^{tot}}. \quad (3.29)$$

From Equation 3.29 we see that for the fisher matrix entries we only require the derivatives of the signal terms of each probe with respect to the parameters. We show the Fisher matrix derivative for the 21cm power spectrum in Appendix A.

In Figure 3.4 we show the forecast constraints in one redshift bin on the HI model pa-

parameters A_{BAO} , $b_{HI}\Omega_{HI}$ and $f\Omega_{HI}$ for the HIRAX experiment considering 256, 512 and 1024 dishes. Here we fix σ_8 since it is degenerate with f and we marginalize over the distance parameters. In Chapter 4 we show how we can break the degeneracy between σ_8 and f using a three point function correlation with the CMB lensing convergence field. We see how the increased number of dishes would improve our sensitivity to the HI model parameters and improve the constraints. We would expect this effect since the number of dishes scales up the baseline density which improves our response towards the 21cm signal.

In Figure 3.5 we show the constraint errors expected to be obtained from the HIRAX survey on the BAO wiggles and distance volume scale. The errors on the BAO wiggles are computed by accounting for the total sensitivity to the measured power spectrum in narrow bins over the entire survey redshift range. We must account for how the uncertainty in all the parameters affect the BAO measurements. We therefore compute the full Fisher matrix in these bins and take the fractional errors on the power spectrum at each bin. We see in Figure 3.5(a) how HIRAX is designed to minimize its noise particularly on the scales relevant to BAO cosmology. Here again we compare the ability of the HIRAX experiment to measure the BAO for 256, 512 and 1024 dishes.

The constraints on $D_V(z)$ shown in 3.5(b) is relatively straightforward to compute. We simply replace the original distance scale parameters with $D_A(z)$ and $H(z)$ then transform these into $D_V(z)$ according to Equation 3.25. In Figure 3.5(b) it is clear how the tight constraints on the volume scale by HIRAX will be able to pick up small variations between the distance models.

We see from these constraints how HIRAX can tie down the oscillation features as a function of scale and redshift. The errors on both the BAO and volume scale shown in Figure 3.5 particularly for the 1024 dish experiment is extremely promising, showing that HIRAX 1024 will be highly sensitive to these quantities. We can then turn these promising constraints into cosmological constraints and of particular interest for the HIRAX experiment would be to constrain the expansion history and dark energy parameters.

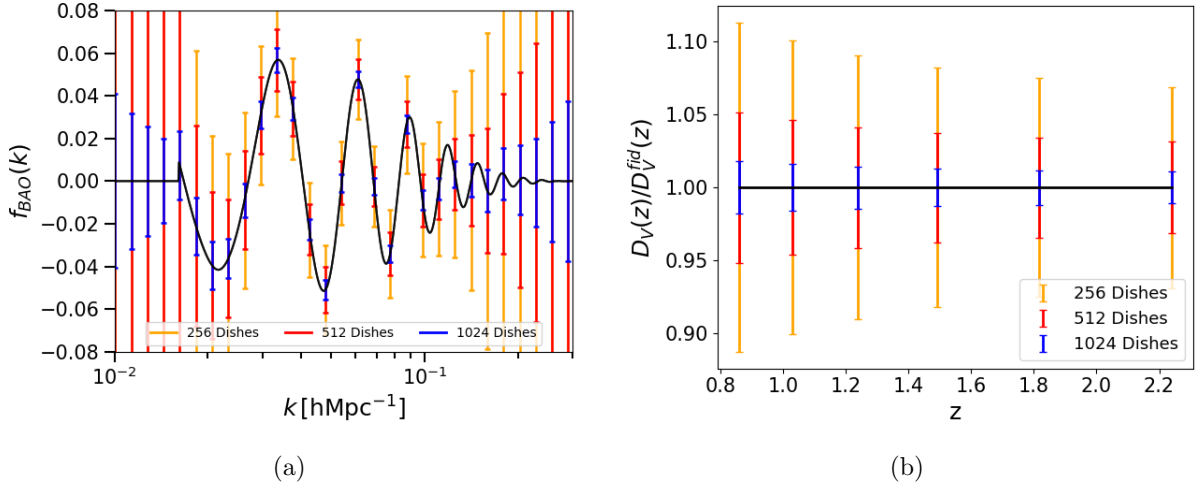


Figure 3.5: (a) Constraints on the BAO wiggles for the HIRAX survey combined over all redshift bins. (b) Constraints on the distance volume scale as a function of redshift in the HIRAX range.

3.3.2 Dark Energy Constraints

To obtain the Fisher matrix with forecasts on the cosmological parameters we need to transform our constraints on the redshift function parameters to the cosmological parameters. The constraints on the cosmological parameters would be summed over the entire survey redshift range. From the Fisher matrix consisting of the cosmological parameters we can obtain constraints on the dark energy equation of state parameters and FOM estimates.

To do this we use a simple linear transformation matrix of the form

$$[F'_{\alpha'\beta'}] = [M_{\alpha\beta}]^T [F_{\alpha\beta}] [M_{\alpha\beta}] \quad (3.30)$$

where $F_{\alpha\beta}$ is the fisher matrix with parameters $p = \{f(z), \alpha_{\perp}, \alpha_{\parallel}\}$ and $F'_{\alpha'\beta'}$ is the new fisher matrix with cosmological parameters $p' = \{\Omega_k, \Omega_{\Lambda}, w_0, w_a, h, \gamma\}$. Here Ω_k and Ω_{Λ} are the density contrast parameters for curvature k and dark energy Λ and $M_{\alpha\beta} = \frac{\partial p_i}{\partial p'_j}$ is the transformation matrix. The density contrast parameters satisfy the dimensionless Friedmann equation $\Omega_{\Lambda} + \Omega_m + \Omega_k = 1$ where Ω_m is the matter density contrast. We show the derivatives of the different probes with respect to the distance parameters α_{\perp} and α_{\parallel} in Appendix A. The

parameter h here is a scaling commonly used in astronomy defined in terms of the Hubble constant $H_0 = 100h \text{ km s}^{-1} \text{ Mpc}^{-1}$. The γ parameter is defined from the linear growth rate $f = \Omega_m(z)^\gamma$. Strong constraints on γ can put limits on modified gravity theories and alternative GR models [108].

The dark energy equation of state parameters w_0 and w_a we obtain from assuming a varying cosmological constant. We assume that dark energy varies over time in the universe and we parameterize the equation of state for the dark energy according to a redshift expansion [109]

$$w(z) = w_0 + w_a \frac{z}{1+z}. \quad (3.31)$$

The dark energy equation of state parameters are of particularly high interest to many LSS surveys. One can obtain constraints on the dark energy parameters by high precision measurements on f , $H(z)$ and $D_A(z)$ through a range of redshifts. Though the parametric form for the dark energy equation of state may vary according to models and interest, an overall estimator to an experiment sensitivity to dark energy EOS parameters are quantified through the Figure of Merit (FOM) as defined by the Dark Energy Task Force (DETF) [110]. The FOM can be calculated from the Fisher matrix containing the cosmological parameter forecasts by

$$\text{FOM} = 1/\sqrt{\det(F^{-1}|_{w_0, w_a})}. \quad (3.32)$$

where $F^{-1}|_{w_0, w_a}$ is the inverse of the 2x2 sub Fisher matrix containing only the dark energy parameters w_0 and w_a .

The measurements made by a given survey may in the end be insufficient to constrain all the parameters of interest at once. For 21cm measurements this is certainly the case and one needs to combine measurements which may have already been conducted by other surveys. The most common of these is to add Planck CMB results into the constraints of a given survey because the CMB measurements has already given such high precision cosmological results. Adding an existing constraint to the new constraints is referred to as adding ‘priors’ or ‘prior information’. Here we combine Planck priors with our cosmological parameter constraints to break degeneracies and help obtain overall improvements on the

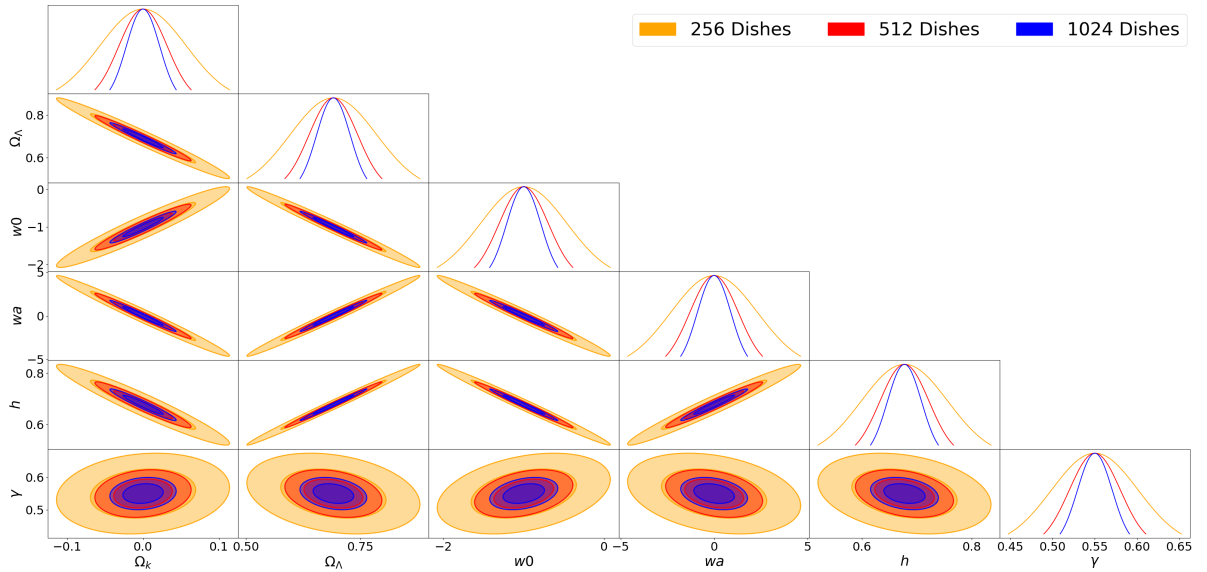


Figure 3.6: HIRAX constraints on the cosmological parameters for the 256, 512 and 1024 dish cases.

measurements. Understanding the improvement on the current constraints we have can give more insights into the capabilities of an upcoming survey.

In Figure 3.6 we show the cosmological parameter constraints for the HIRAX experiment over the entire survey redshift range. Here again we compare the effect of increasing the number of dishes. We compare the HIRAX 1024 measurements by adding in Planck priors on the cosmological parameters in Figure 3.7. We see here how the Planck priors help to make the HIRAX constraints much tighter on the cosmological parameters. We should note that the constraints on the dark energy EOS parameters may not be well measured by Planck but by combining both surveys we obtain overall improvements to all the varying parameters. Once we obtain data from the HIRAX survey it will be possible to construct a HIRAX + Planck likelihood which we can use to obtain a combined constraint on the cosmological parameters.

We show in Figure 3.8 the zoomed in constraints on the dark energy parameters. Here we show the concurrent constraints on both the dark energy EOS parameters showing how the constraints on one parameter influences the constraints on the other parameter for the HIRAX experiment alone and then with Planck priors added. We see in Figure 3.7 how

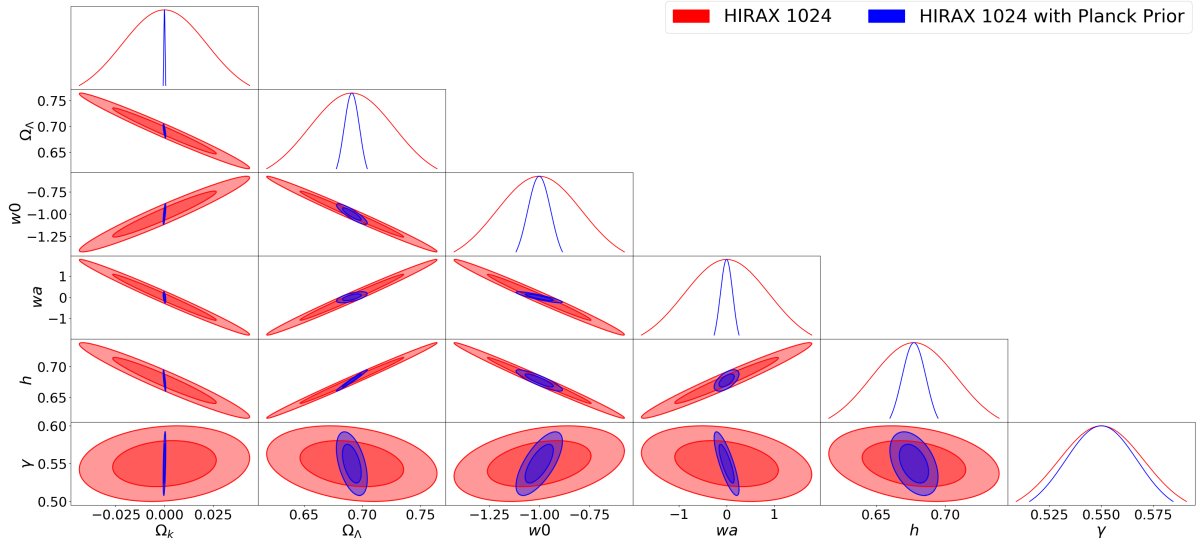


Figure 3.7: Cosmological constraints by HIRAX with Planck priors added in.

adding Planck priors to HIRAX measurements can improve the cosmological constraints. We see in Figure 3.8 how the prior information tightens the errors particularly on the linear EOS term w_0 . We compute the FOM for the HIRAX experiment with Planck priors to be around 436. We show in Chapter 4 how by using the CMB lensing convergence cross bispectrum we can greatly improve this estimate. In [36] they estimate that the best SKA phase 1 FOM is about 444. In [111] they compute the SKA phase 2 weak lensing dark energy FOM with a Planck Prior to get the FOM to be around 305. In [112] they compute forecasts for the FAST experiment and show that the best constraints by FAST on the dark energy EOS parameters are $\sigma_{w_0} = 0.04$ and $\sigma_{w_a} = 0.10$. In comparison our forecasts for HIRAX gives very similar constraints with $\sigma_{w_0} = 0.0472$ and $\sigma_{w_a} = 0.1068$. We further note that the HIRAX dark energy constraints greatly improves the current Planck constraints. The latest Planck results with combined Planck lensing and BAO information gives an error on w_0 as $\sigma_{w_0} = 0.2$ [113]. This is an improvement of about 9% in the parameter error. Hence we see how competitive the HIRAX dark energy measurements can be in autocorrelation mode with other survey forecasts.

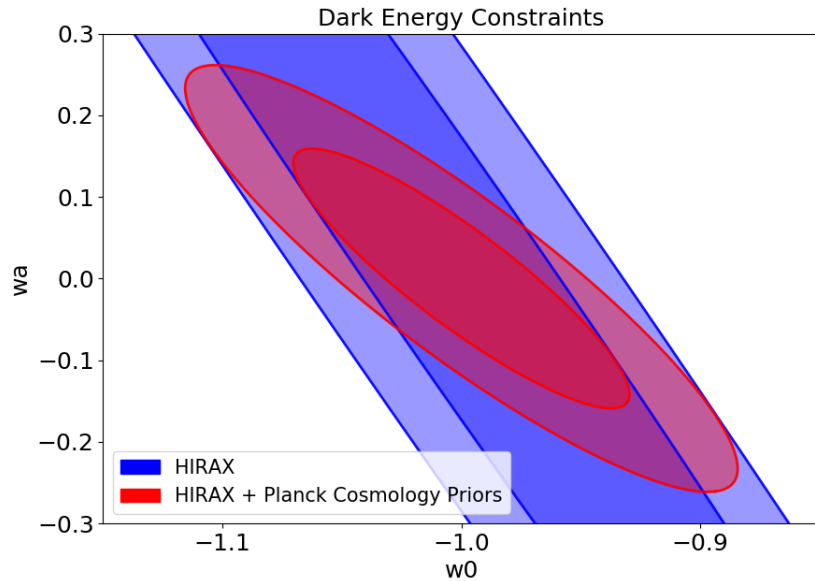


Figure 3.8: DE constraints on the EOS parameters for the HIRAX experiment. We show the improvement by adding in Planck priors to the cosmological set of parameters.

3.4. HIRAX Array Layout Optimisation

We have seen in the interferometer noise power spectrum equation that the sensitivity of the survey is affected by the array layout. Here we examine the effect of the array layout on the HIRAX experimental noise response as well as how it affects the calibration and foreground mitigation efforts. The array layout can also determine the data rate and data volumes of the experiment and hence choosing the optimal arrangement for the array is an important task that balances the HIRAX science goals, systematics and challenges.

The main task that follows this exercise is the ability of these layouts to extract the 21cm cosmological signal in the presence of a foreground contaminant. We seek to best set up the sensitivity of the baselines by minimizing the leakage of foreground signal into the cosmological signal. This means that given our final choice of array layout we hope to effectively recover and separate out the foregrounds and 21cm signals in frequency.

3.4.1 Array Layout Strategies

Here we simulate various array layouts to compare their abilities in the context of the HIRAX science goals and physical constraints such as data rate and volume. We compare the simulations for five proposed array layouts which we have labelled as the: ‘standard grid’, ‘subgrid’, ‘alternate spacing grid’, ‘extended grid’ and finally ‘Hera like grid’. The Hydrogen Epoch of Reionisation Array (HERA) experiment is designed to detect the distinctive signature that would allow us to understand the formation and evolution of the first stars and galaxies in the Universe [114]. HERA is located in the South African Karoo Astronomy Reserve and is expected to be the most sensitive SKA pathfinder to study the EOR. The HERA telescope will be constructed in an hexagonal closed packed arrangement and we consider this type of layout for our ‘Hera like grid’ case.

We discuss each of these grid arrangements below and we compare their baseline redundancies and uv coverage or sensitivity [115]. We will show the array layouts in the real space on an East-West (EW) and North-South (NS) grid arrangement and we show their uv redundancy coverage at the 600 MHz frequency channel.

The Standard Grid Layout

The standard grid layout is the proposed compact square closed packed grid. Here we assume compactness, i.e the dishes are packed such that their edges touch but in reality this may not be practical. Hence, a follow-up application of these simulations would be to study the effect of dish separation on the sensitivity.

The choice of a compact grid, which we consider in most of our simulations is to take advantage of redundancy and maximize small scale sensitivity needed for BAO measurements. The redundancy helps in calibrating the instrument because if we have many measurements of the same baseline we can calibrate that measurement more accurately. Redundancy also helps to keep the data rates and volume lower since if you more redundancy you have less unique baselines and hence less data. We see in Figure 3.9 the standard grid has its redundancy highly compact in the uv space mainly concentrated towards the lowest uv modes. This is

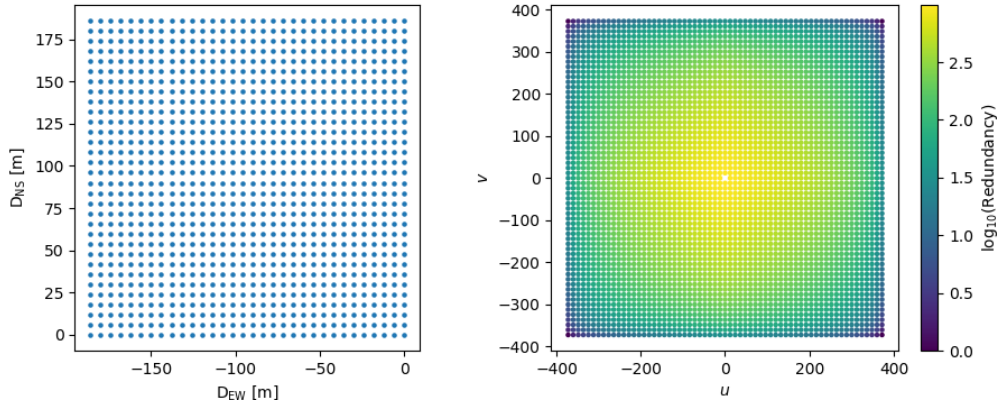


Figure 3.9: Compact square grid layout. On the left we show the layout in real space laid in EW and NS spacing. On the right we show the uv redundancy in the 600 MHz frequency channel.

expected since the standard grid is highly compact and samples many of the smallest baseline separations really well.

The Subgrid Layout

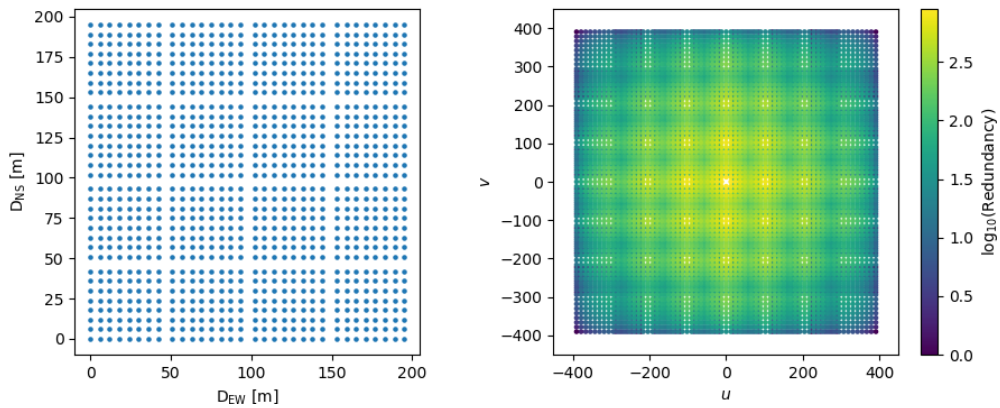


Figure 3.10: The Subgrid layout and uv redundancy in the 600MHz frequency channel.

In this layout arrangement we split the entire HIRAX 1024 array into 16 smaller subgrids of 64 dishes (8x8) in each segment. Here we seek to improve our redundant calibration efforts for most baselines by splitting the grids into smaller grids which we can sample individually.

We also investigate how this layout would affect the overall uv coverage which we can see from Figure 3.10. The uv redundancy shows a lot more structure which is created from subdividing the single grid. This would be a problem for any imaging efforts but the HIRAX experiment science goals do not require good imaging capabilities. The advantage of this uv sampling would be to improve our overall uv sensitivity as a function of frequency as we shall see in Section 3.4.2.

Alternate Spacing Grid

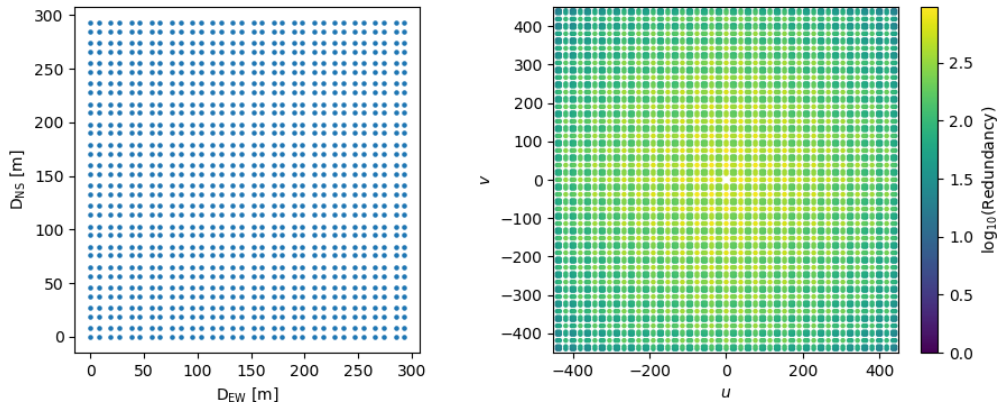


Figure 3.11: Alternate Spaced grid and uv coverage in the 600MHz frequency channel.

The alternate spaced grid layout or ‘fat vs skinny aisles’ layout is a variation of the subgrid layout. In this version we alternate the spacing between the dish edges using a 2m vs 5m alternating gaps. The idea here is to sample grids at half dish size spacing (3m) to help fill up the uv coverage for calibration and especially foreground treatment. We see in Figure 3.11 the layout of this strategy and the uv redundancy in the 600MHz channel. We see that the uv coverage does spread power more evenly throughout the uv space compared to the compact grids which has more redundancy at the smaller uv scales. This is a trade off between overall sensitivity for better uv sampling. As we discuss in Section 3.4.2 it may be of no benefit to have good sensitivity but lack the ability to remove the foregrounds efficiently. In other words it may be necessary to trade off overall sensitivity for uv sampling to effectively remove

the foreground signal.

Extended Grid Layout

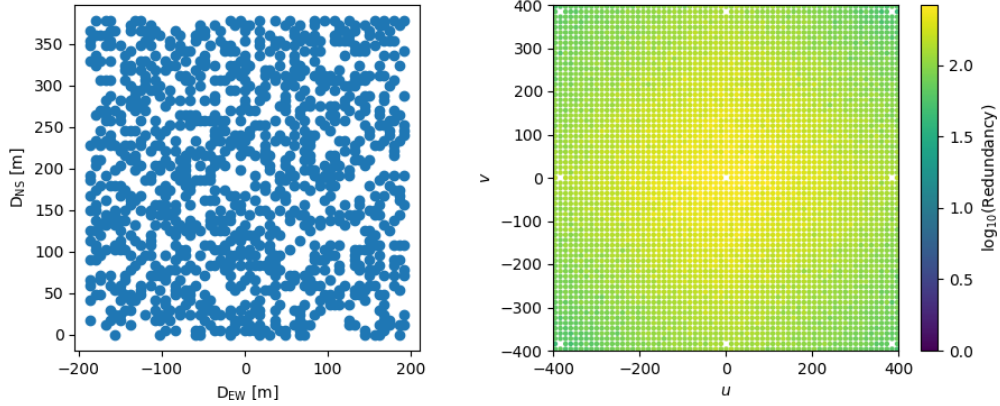


Figure 3.12: Extended grid layout and uv redundancy in the 600MHz range.

The extended grid layout is a slightly more complicated idea. Here we extend the region of the standard grid array into four larger segments or basically we double the length of the sides both in the EW and NS directions to create four quadrants of HIRAX standard grid outlines. We then take each of the 1024 dishes in the standard grid and assign them randomly in each of the four quadrants. In this way they preserve their initial position in the standard grid but move around to a different quadrant randomly. Here we greatly improve the uv sampling as compared to the compact grids as seen in Figure 3.12 however as we shall see in Section 3.4.2, for the extended grid and the alternate spacing grid we would suffer increased data rates and volume since we have spread the redundancy more uniformly from the shorter baselines to longer baselines.

HERA Like Grid

Here we consider placing the 1024 6m HIRAX dishes in a similar way that has been done for the HERA experiment. HERA has performed many tests and simulations on their array layout and proposed their hexagonal shape as an ideal way to sample the uv space and

obtain excellent redundancy [115]. The HERA experiment also uses outliers to improve their uv coverage and imaging but we do not consider outliers in our case. We show the layout and uv redundancy in Figure 3.13.

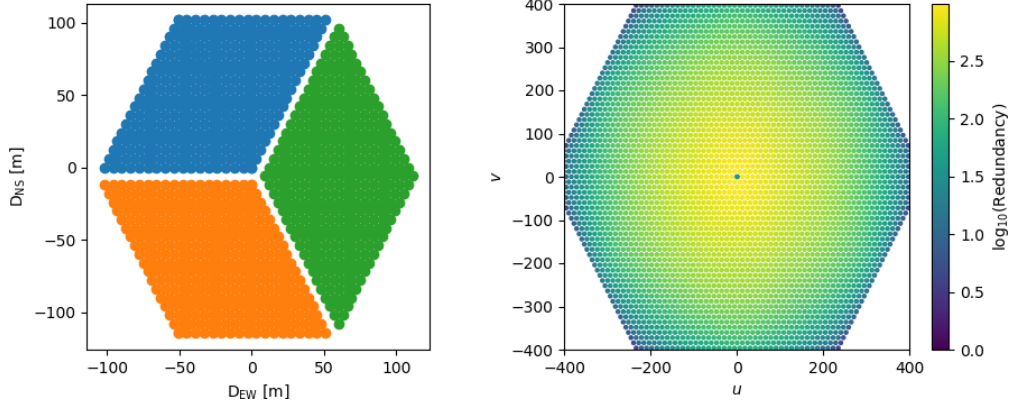


Figure 3.13: HERA-like array layout and uv redundancy in the 600MHz frequency channel.

3.4.2 Grid Layout Comparison and Analysis

We now summarise the results of the various grid layouts and show how they compare by their redundancy, data rates/volumes, sensitivity and redundant calibration. We also show how we can turn the redundancy information of the above layouts into sensitivity measurements which we can use to study the foreground removal and signal extraction capabilities.

To now compare the various layouts and how they challenge each other in the various aspects of uv coverage, data volume, data rates, calibration and noise sensitivity we have compiled a summary of plots shown in Figure 3.14.

In Figure 3.14 we first plot the redundancy against unique baseline index. This plot counts number of baselines for every unique baseline separation. This plot shows us the amount of data we expect to obtain for the different layouts. The maximum unique baseline index for each grid also indicated the total data volume for the different grids. From these plots we get a metric to compare the data rate and data volume for the different array layouts. The plot shows that the standard grid and HERA grid are very similar in their data performances.

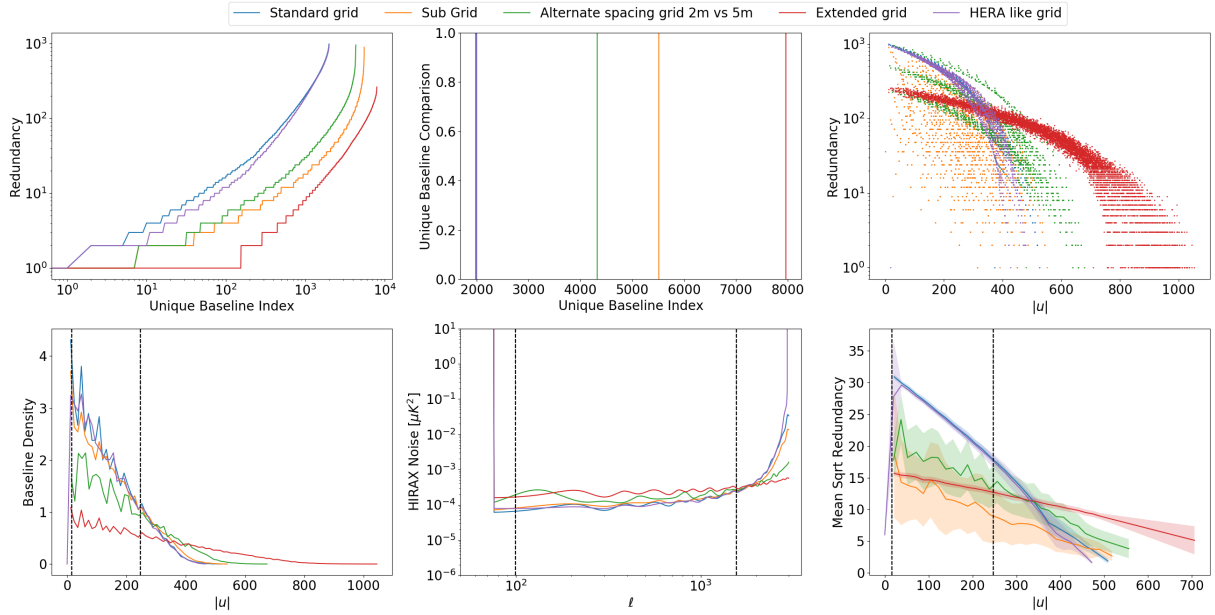


Figure 3.14: Grid layout summary plots computed in the 600 MHz frequency channel. We plot the redundancy vs unique baseline index which quantifies the data rate and volume. We plot the baseline density function which quantifies the sensitivity and can be converted into a noise estimate comparing the various grids. The mean square root of the redundancy quantifies the calibration efficiency.

These two grids are the best performers in this metric with the lowest expected data rate and data volume. The alternate grid, subgrid and extended grid are much higher in the maximum unique baseline index and redundancy for each unique baseline. The plot indicates that the extended grid is about four times higher in data volume than the standard and HERA grids. The Alternate spacing grid and subgrids are about two to three times higher in its data volume than the standard and HERA grids.

We then plot the redundancy against $|u|$ for the various grids. Here we show the redundancy as a scatter plot as a function of $|u|$ where $|u| = \sqrt{u^2 + v^2}$. This plot shows the spread of the redundancy for different baseline lengths $|u|$. We see here in this metric also that the standard grid and HERA grid are very similar in their redundancy over uv coverage. These two scatter plots basically overlay each other. The subgrid case spreads the redundancy around more on the lower $|u|$ values and this is due to the grid being subdivided into smaller squares. The alternate spacing and extended grids both spread the concentration of

the redundancy points from the smaller baselines to the larger ones.

The baseline density plot verse $|u|$ gives the measure of a layouts sensitivity. We recall from Section 3.2 that the interferometer noise depends on the baseline density function $n(u)$. Here we have plotted this baseline density function for the different array layouts. The baseline redundancy is an histograms of the redundancy scatter plot and we expect to see the same features. Here we see the standard grid, Hera grid and subgrid are more sensitive to the lower $|u|$ scales. The dashed black lines show the BAO scales in this frequency band. We see that the extended grid and alternate spacing grid pushes out sensitivity from the BAO scales outward toward the higher $|u|$ scales.

Since we know that the HIRAX interferometer noise depends on the baseline redundancy we can easily compute this noise for the various array layouts with their baseline density functions. We show the HIRAX noise for the different array layouts. Here again we plot the BAO scales in the black dashed lines. The effect on the overall noise amplitudes by the array layouts is not too severe. We see how the alternate spacing and extended grids which spreads the redundancy from shorter baseline lengths to longer baselines lose overall sensitivity since the total baseline density peak is flattered but we see that for these cases the noise extends out to higher $\ell = 2\pi|u|$ modes.

Finally we plot the mean square root of the redundancy. Here we compute a mean value in $|u|$ bins for the redundancy scatter and the shaded region shows the variance in each bin. This metric quantifies the calibration efforts for the arrays. We know that if we have higher redundancy it means we have many measurements of the same baseline length. This makes calibrating this baseline easier and more accurate. The caveat here is that we may naively expect the higher redundancy layout to be better for calibration. This may not be true, for example consider the standard grid and HERA grid cases, here they have the best mean square root redundancy in amplitude but only for lower u values $u < 400$. For array layouts with larger maximum separations we see that calibration on the longest baselines are improved well outside the BAO scales, however this may not improve our BAO constraints. The extended grid does the best at maintaining a constant calibration metric for most $|u|$ values.

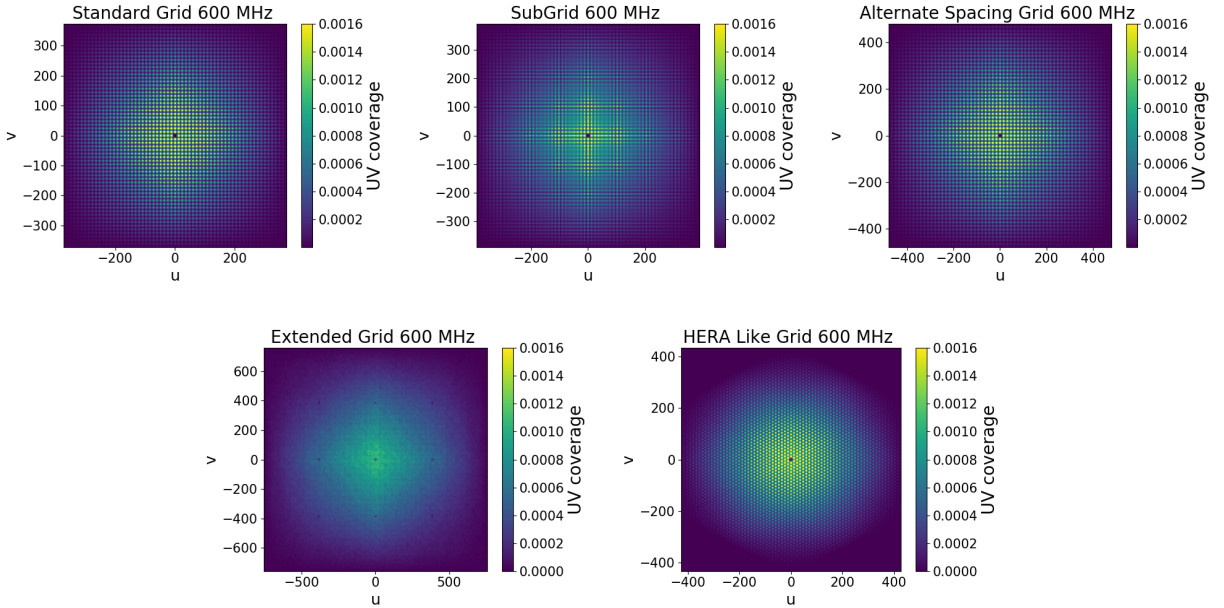


Figure 3.15: The uv coverage for the different array layout cases convolved with the primary beam. Here we see the alternate grid uv coverage is very similar to the standard grid case. The subgrid case induces much more structure into the redundancy at a single frequency snapshot. The extended grid spreads the redundancy over a wider uv range.

We now examine the uv coverage sensitivity for the grid layouts showing how we can obtain an estimate for the foreground characterisation and signal extraction. In Figure 3.15 we convolve the uv redundancy with the primary beam model for the dish. We assume the primary beam is Gaussian with a width corresponding to the HIRAX dish FWHM given by

$$B(\theta, \nu) = e^{-16 \ln(2) \theta^2 \theta_b^2} \quad (3.33)$$

where $\theta_b \approx D_{dish}/\lambda$ is the FWHM of a single dish with diameter D_{dish} . This convolution with the primary beam accounts for the response of the dish to the sky measurements which we show in Figure 3.15. We see how the primary beam causes the discrete dish points in the uv plane to be tapered off at the edges and it diminishes the overall sensitivity at the edge of the arrays according to the beam size. This is a more realistic simulation of our sensitivity given a dish beam pattern. We now look at one dimensional slices of this sensitivity estimate and how it evolves in the frequency direction. We do this to understand and compare how the

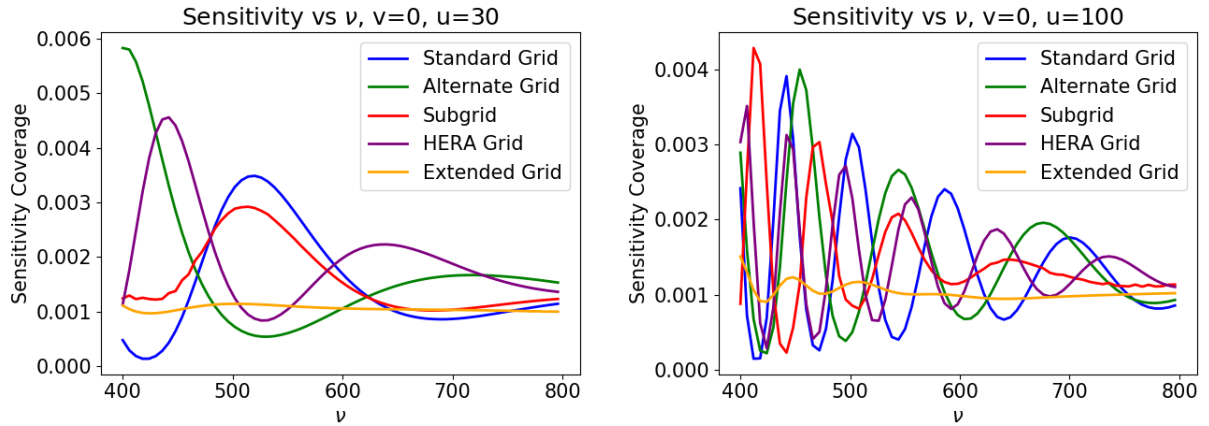


Figure 3.16: One dimensional slices of the array layout sensitivity as a function of frequency. We have sliced the coverage along $v = 0$ for $u = 30$ and $u = 100$. We see that our sensitivity along frequency oscillates in give uv modes which means we have ‘holes’ in our frequency coverage.

different array layouts will measure the 21cm signal. We show in Figure 3.16 the uv coverage sensitivity as a function of frequency at $v = 0$ for $u = 30$ and $u = 100$. This plot shows how the redundancy coverage fans out as a function of frequency. This happens because of the decreasing wavelength, i.e. at higher frequency the baseline separation in wavelength units gets larger. This frequency dependence affects the way a given array layout can measure the 21cm signal in frequency. If we consider a given curve in Figure 3.16 which represents a given uv mode, we see peaks and troughs in the frequency coverage. These peaks and troughs shows where the layouts sensitivity is for uv modes in frequency direction. We can only measure the signal where we have sensitivity and this means we can not measure the signal where there are troughs in Figure 3.16. Given a high amplitude smoothly varying foreground mode and an oscillating low amplitude 21cm signal along the 1D slices of sensitivity vs frequency we are required to recover the signal by each array layout. In this way we can compare the ability of the grids in the foreground mitigation effort by simulating a foreground signal and cosmological signal along our sensitivity and performing a signal reconstruction for each case.

In Figure 3.16 we can see that the subgrids but more especially the extended grid does the best in terms of reducing the peak to through ratio resulting in a smoother sensitivity.

This is the type of array we want to optimise to. We would like to preserve our redundancy and BAO sensitivity as much as possible while creating an array that would smooth out the sensitivity oscillations in the frequency direction.

Overall we see that the standard and the HERA grids are the best layouts in terms of redundancy, noise sensitivity and data challenges. However, our early results on the frequency sensitivity suggest that these array layouts may suffer from foreground leakage. In order to quantify the foreground leakage we plan to pass simulated foreground and 21cm signals to each array layout and see how well each layout can extract the 21cm signal. We can then compare these layouts for the final questions of interest which is the foreground subtraction and decide which is the best optimal layout.

Chapter 4

Cross-Correlations With HI Intensity Mapping

Cross-correlation surveys can be used as a powerful tool to probe the large scale structure. In cross-correlation surveys we can mitigate systematic effects and suppress uncorrelated noise. For these reasons, cross-correlations surveys may be able to make more precise measurements or recover information that may be inaccessible in the autocorrelation measurements. Here we consider cross-correlating the HIRAX 21cm survey with other large scale structure probes such as CMB lensing measurements by the AdvACT telescope, photometric galaxy surveys from LSST or DES and spectroscopic galaxy surveys from WFIRST or DESI. We discuss the prospect of each cross-correlation below showing the promising potential to make these detections and obtain high precision parameter constraints.

In this chapter we obtain new results on the prospects of cross-correlating the HIRAX experiment measurements with other large scale structure surveys. In Section 4.1 we show that the two point cross-correlation survey of HIRAX measurements with CMB lensing measurements vanishes after foreground removal. We then show that by considering the 21cm field up to second order we can compute a three point function cross-bispectrum between the 21cm position dependent power spectrum and the mean CMB lensing convergence field to recover a high signal to noise detection of this signal. We also show how the bispectrum parameter constraints can significantly improve the HIRAX 21cm constraints. In Section

4.2 we show the cross-correlation prospects for HIRAX with WFIRST spectroscopic galaxy measurements and for LSST photometric galaxy measurements. We show that for HIRAX cross-correlated with WFIRST measurements we can make high precision signal detection and put tight constraints on the HI model parameters as well as the galaxy bias terms. We also find that the HIRAX-LSST cross-correlation will be measured with high a signal to noise ratio.

4.1. HI IM-CMB Lensing Cross-Correlation

The lensing of CMB photons by intervening matter provides a projected estimator for the matter distribution of the universe. The lensing of the CMB photons means that the measured CMB we observe today is not actually the primordial CMB but rather a lensed version which encodes information of the matter distribution of the universe. We now investigate the possibility of measurements from HIRAX to be cross-correlated with CMB lensing measurements. For the CMB lensing measurements we consider the AdvACT experiment. The AdvACT is the planned upgrade for the 6m aperture Atacama Cosmology Telescope (ACT). The AdvACT will observe the CMB in five frequency bands and over a larger area of the sky with extremely high precision [116]. The specifications for the AdvACT telescope are given in Table 4.1 below.

Experiment	AdvACT
Channel	150 GHz
Beam size	1.4 arcmin
Temp Sensitivity	$7 \mu K$ -arcmin
Pol Sensitivity	$10 \mu K$ -arcmin

Table 4.1: AdvACT survey specifications [117].

4.1.1 CMB Lensing Convergence

As we have discussed in Section 2.2.5 the CMB lensing convergence is given by [79, 80]

$$\kappa(\boldsymbol{\theta}) = \int d\chi_{\parallel} W_{\kappa}(\chi_{\parallel}) \delta_m(\mathbf{r}; z) \quad (4.1)$$

where the lensing kernel is

$$W_{\kappa}(\chi_{\parallel}) = \frac{3}{2} \Omega_{m0} \left(\frac{H_0}{c} \right)^2 \chi_{\parallel}^2 \left(\frac{\chi_{\parallel}^* - \chi_{\parallel}}{\chi_{\parallel}^* \chi_{\parallel}} \right) (1 + z). \quad (4.2)$$

This expression for the convergence field describes the total integrated sum of the matter density fluctuation from the surface of last scattering to us today. This gives the statistical measure of the overall degree of deflection in the CMB measurements. Decomposing the convergence field into plane waves in the comoving volume gives

$$\kappa(\boldsymbol{\ell}) = \int \frac{dk_{\parallel}}{(2\pi)} \int d\chi_{\parallel} e^{ik_{\parallel}\chi_{\parallel}} K(\chi_{\parallel}) \frac{\delta_m\left(\mathbf{k}_{\perp} = \frac{\boldsymbol{\ell}}{\chi_{\parallel}}, k_{\parallel}, z = 0\right)}{\chi_{\parallel}^2} \quad (4.3)$$

where we have defined the lensing convergence kernel and its harmonic space counterpart as

$$K(\chi_{\parallel}) = W_{\kappa}(\chi_{\parallel}) D(\chi_{\parallel}) \quad (4.4)$$

$$K(k_{\parallel}) = \int d\chi_{\parallel} e^{ik_{\parallel}\chi_{\parallel}} W_{\kappa}(\chi_{\parallel}) D(\chi_{\parallel}). \quad (4.5)$$

respectively. In Figure 4.1 we show the CMB lensing kernel in real space as well as the overlapping redshift bins we are considering. Using Equation 4.3 we compute the CMB

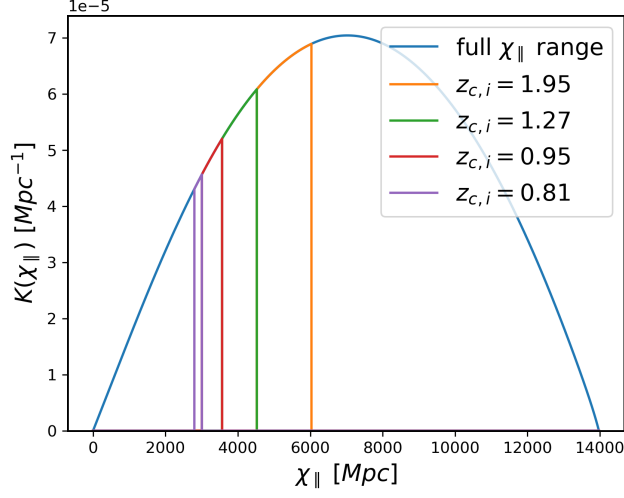


Figure 4.1: The CMB lensing kernel in real space which shows the CMB lensing power as a function of comoving distance. We also plot here the HIRAX redshift range split into four bins centred at the indicated z_i which we have used in the cross-correlation study.

lensing convergence angular power spectrum as

$$\begin{aligned}
C_\ell^{\kappa\kappa} &= \int \frac{d^2\ell'}{(2\pi)^2} \langle \kappa(\boldsymbol{\ell}) \kappa^*(\boldsymbol{\ell}') \rangle \\
&= \int \frac{d^2\ell'}{(2\pi)^2} \int \frac{dk_\parallel}{(2\pi)} \int \frac{d\chi_\parallel}{\chi_\parallel^2} \int \frac{dk'_\parallel}{(2\pi)} \int \frac{d\chi'_\parallel}{\chi'^2_\parallel} e^{ik_\parallel\chi_\parallel - ik'_\parallel\chi'_\parallel} \times \\
&\quad K(\chi_\parallel) K(\chi'_\parallel) \langle \delta_m(\mathbf{k}, z=0) \delta_m^*(\mathbf{k}', z=0) \rangle \\
&= \int \frac{dk_\parallel}{(2\pi)} \int d\chi_\parallel K(\chi_\parallel) \int d\chi'_\parallel K(\chi'_\parallel) e^{k_\parallel(\chi_\parallel - \chi'_\parallel)} \frac{P_m\left(\mathbf{k}_\perp = \frac{\boldsymbol{\ell}}{\chi_\parallel}, k_\parallel, z=0\right)}{\chi_\parallel^2}.
\end{aligned} \tag{4.6}$$

In the Limber approximation the CMB lensing convergence power spectrum reduces to [46]

$$C_\ell^{\kappa\kappa, Limber} = \int d\chi_\parallel K^2(\chi_\parallel) \frac{P_m\left(\frac{\boldsymbol{\ell}}{\chi_\parallel}, z=0\right)}{\chi_\parallel^2}. \tag{4.7}$$

To obtain the lensing convergence noise we use the harmonic space minimum variance

estimator for the lensing potential [118]

$$\hat{\psi}_{XY}(\boldsymbol{\ell}) = N_{XY}(\boldsymbol{\ell}) \int \frac{d^2\boldsymbol{\ell}'}{(2\pi)^2} \tilde{X}(\boldsymbol{\ell}') \tilde{Y}^*(\boldsymbol{\ell} - \boldsymbol{\ell}') g_{XY}(\boldsymbol{\ell}', \boldsymbol{\ell}) \quad (4.8)$$

where X, Y represents the temperature or polarization components of the CMB spectra T , E and B . For the temperature field TT the lensing potential becomes

$$\hat{\psi}_{TT}(\boldsymbol{\ell}) = N_{TT}(\boldsymbol{\ell}) \int \frac{d^2\boldsymbol{\ell}'}{(2\pi)^2} \tilde{T}(\boldsymbol{\ell}') \tilde{T}^*(\boldsymbol{\ell} - \boldsymbol{\ell}') g_{TT}(\boldsymbol{\ell}', \boldsymbol{\ell}) \quad (4.9)$$

where the function $g_{XY}(\boldsymbol{\ell}', \boldsymbol{\ell})$ is a weight function and for the TT case is

$$g_{TT}(\boldsymbol{\ell}', \boldsymbol{\ell}) = \frac{\boldsymbol{\ell}' \cdot \boldsymbol{\ell} C_{\ell, S}^{TT} + (\boldsymbol{\ell} - \boldsymbol{\ell}') \cdot \boldsymbol{\ell} C_{|\boldsymbol{\ell}' - \boldsymbol{\ell}|, S}^{TT}}{2\tilde{C}_{\ell, S}^{totTT} \tilde{C}_{\boldsymbol{\ell}' - \boldsymbol{\ell}, S}^{totTT}}. \quad (4.10)$$

For the polarization cross term $X = E$ and $Y = B$ the weight function becomes

$$g_{EB}(\boldsymbol{\ell}', \boldsymbol{\ell}) = \sin(2\phi) \frac{\boldsymbol{\ell}' \cdot \boldsymbol{\ell} C_{\ell, S}^{EE} + (\boldsymbol{\ell} - \boldsymbol{\ell}') \cdot \boldsymbol{\ell} C_{|\boldsymbol{\ell}' - \boldsymbol{\ell}|, S}^{BB}}{\tilde{C}_{\ell, S}^{totEE} \tilde{C}_{\boldsymbol{\ell}' - \boldsymbol{\ell}, S}^{totBB}} \quad (4.11)$$

where ϕ is the angle between $\boldsymbol{\ell}$ and $\boldsymbol{\ell} - \boldsymbol{\ell}'$. The normalization which ensures the estimator is unbiased for the TT case is

$$N_{TT}(\boldsymbol{\ell})^{-1} = \int \frac{d^2\boldsymbol{\ell}'}{(2\pi)^2} \frac{[\boldsymbol{\ell}' \cdot \boldsymbol{\ell} C_{\ell, S}^{TT} + (\boldsymbol{\ell} - \boldsymbol{\ell}') \cdot \boldsymbol{\ell} C_{|\boldsymbol{\ell}' - \boldsymbol{\ell}|, S}^{TT}]^2}{2\tilde{C}_{\ell, S}^{totTT} \tilde{C}_{\boldsymbol{\ell}' - \boldsymbol{\ell}, S}^{totTT}} \quad (4.12)$$

where $\tilde{C}_{\ell}^{tot} = C_{\ell, S}^{TT} + C_{\ell, N}^{TT}$. Similarly for the polarization cross term the normalization is

$$N_{EB}(\boldsymbol{\ell})^{-1} = \int \frac{d^2\boldsymbol{\ell}'}{(2\pi)^2} \frac{[\boldsymbol{\ell}' \cdot \boldsymbol{\ell} C_{\ell, S}^{EB} + (\boldsymbol{\ell} - \boldsymbol{\ell}') \cdot \boldsymbol{\ell} C_{|\boldsymbol{\ell}' - \boldsymbol{\ell}|, S}^{EB}]^2 \sin^2(2\phi)}{\tilde{C}_{\ell, S}^{totEE} \tilde{C}_{\boldsymbol{\ell}' - \boldsymbol{\ell}, S}^{totBB}}. \quad (4.13)$$

The noise of the lensing potential reconstruction is given by the inverse of the normalization factor. There are other contributions to the reconstruction such as the TB , EE and BB terms but we only consider the TT and EB combinations here since they provide a close to optimal reconstruction [118]. The convergence noise can be obtained from the lensing potential noise

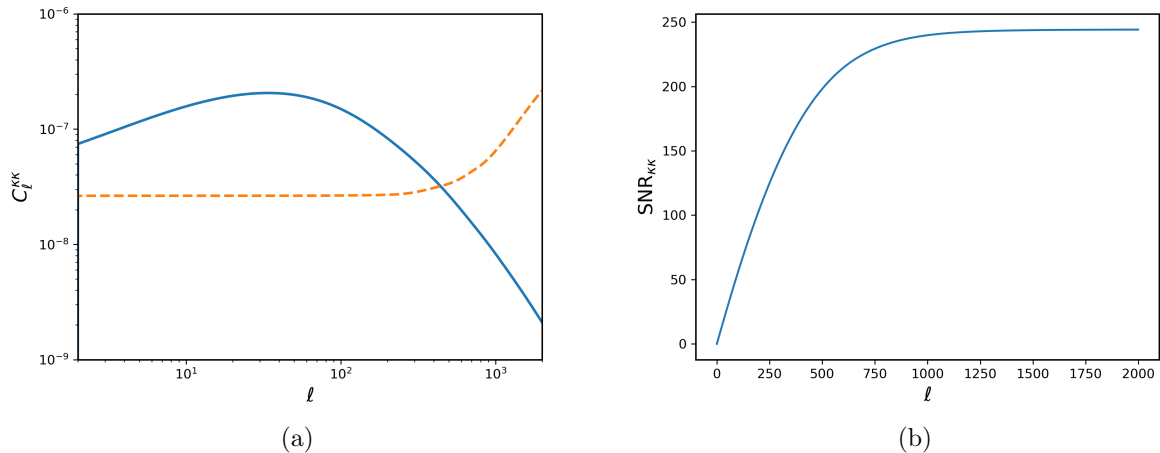


Figure 4.2: (a) CMB lensing convergence power spectrum (blue) versus the CMB reconstruction noise (orange). (b) The SNR calculated for the CMB lensing convergence. We use the CAMB code to compute the CMB lensing convergence power spectrum [76].

using the relation $\kappa(\ell) = \frac{1}{2}\ell^2\psi$. This gives the convergence noise power spectrum as

$$C_{\ell,N}^{\kappa\kappa} = \frac{\ell^4}{4}N(\ell)^{-1}. \quad (4.14)$$

To compute the signal to noise ratio we use

$$(SNR)^2 = \sum_{\ell} 2\ell\Delta\ell f_{sky} \left(\frac{C_{\ell}^{\kappa\kappa}}{C_{\ell}^{\kappa\kappa} + C_{\ell,N}^{\kappa\kappa}} \right)^2. \quad (4.15)$$

where $\ell\Delta\ell f_{sky}$ factor accounts for the number of modes accessible by a measurement.

In Figure 4.2 we show the CMB lensing convergence autocorrelation power spectrum and reconstructed noise. Here we consider the *EB* noise reconstruction which we also use in later sections to compute the cross-correlation. We calculate the convergence signal and the noise using an AdvACT like [117] setup. Figure 4.2(b) shows the cumulative signal to noise ratio we obtain by summing the SNR at every ℓ in quadrature. The SNR shows how experiments like the AdvACT will be able to make a significant detection of the CMB lensing convergence.

4.1.2 Vanishing Of The Two Point Cross-Correlation

In this section we calculate the two point cross-correlation between the HIRAX 21cm survey and the CMB lensing convergence field. We show that the two point function vanishes following a foreground subtraction of low radial modes. In the CMB lensing measurements most of the information is contained at low radial modes but in 21cm measurements such as HIRAX these modes are lost at the cost of foreground removal.

We now calculate the cross-correlation signal between the CMB lensing convergence and the 21cm brightness temperature in a given redshift bin centered at redshift z_i corresponding to central frequency $\tilde{\nu}_i$ with width $\Delta\tilde{\nu}_i = \tilde{\nu}_i^{\max} - \tilde{\nu}_i^{\min}$. The cross-correlation signal as a function of radial modes, $y = k_{\parallel} r_{\nu,i}$, can be calculated by

$$\begin{aligned}
\langle \delta T_{21}(\boldsymbol{\ell}, y; z_i) \kappa^*(\boldsymbol{\ell}') \rangle &= (2\pi)^2 \delta_D^2(\boldsymbol{\ell} - \boldsymbol{\ell}') C_{\ell}^{\kappa \delta T_{21}}(y; z_i) \\
\implies C_{\ell}^{\kappa \delta T_{21}}(y; z_i) &= \int \frac{d^2 \ell'}{(2\pi)^2} \langle \delta T_{21}(\boldsymbol{\ell}, y; z_i) \kappa^*(\boldsymbol{\ell}') \rangle \\
&= \bar{T}_b(z_i) (b_{HI}(z_i) + f(z_i) \mu_k^2) \frac{D(z_i)}{V_p(z_i)} \times \\
&\quad \int \frac{d^2 \ell'}{(2\pi)^2} \int \frac{dk_{\parallel}'}{(2\pi)} \int \frac{d\chi_{\parallel}'}{\chi_{\parallel}'^2} e^{ik_{\parallel}' x_{\parallel}'} K(\chi_{\parallel}') \langle \delta_m(\mathbf{k}, z=0) \delta_m^*(\mathbf{k}', z=0) \rangle \\
&= \bar{T}_b(z_i) (b_{HI}(z_i) + f(z_i) \mu_k^2) \frac{D(z_i)}{V_p(z_i)} \times \\
&\quad \int \frac{d^2 \ell'}{(2\pi)^2} \int \frac{dk_{\parallel}'}{(2\pi)} \int \frac{d\chi_{\parallel}'}{\chi_{\parallel}'^2} e^{ik_{\parallel}' x_{\parallel}'} K(\chi_{\parallel}') \delta_D^2(\mathbf{k}_{\perp} - \mathbf{k}'_{\perp}) \delta_D(k_{\parallel} - k'_{\parallel}) P_m(k, z=0) \\
&= \bar{T}_b(z_i) (b_{HI}(z_i) + f(z_i) \mu_k^2) D(z_i) K_{\kappa} \left(\frac{y}{r_{\nu,i}} \right) \frac{P_m \left(\frac{\ell}{\chi_{\parallel,i}}, k_{\parallel}; z=0 \right)}{V_p(z_i)}.
\end{aligned} \tag{4.16}$$

We can compute a signal to noise ratio estimator for the cross-correlation as

$$(SNR)^2 = (\Delta\tilde{\nu}_i S_{\text{area}}) \int_{y_{\min}}^{y_{\max}} \frac{dy}{(2\pi)} \int_{\ell_{\min}}^{\ell_{\max}} \frac{\ell d\ell}{(2\pi)} \frac{(C_{\ell,S}^{\kappa \delta T_{21}}(y; z_i))^2}{\text{var}[C_{\ell,S}^{\kappa \delta T_{21}}]}. \tag{4.17}$$

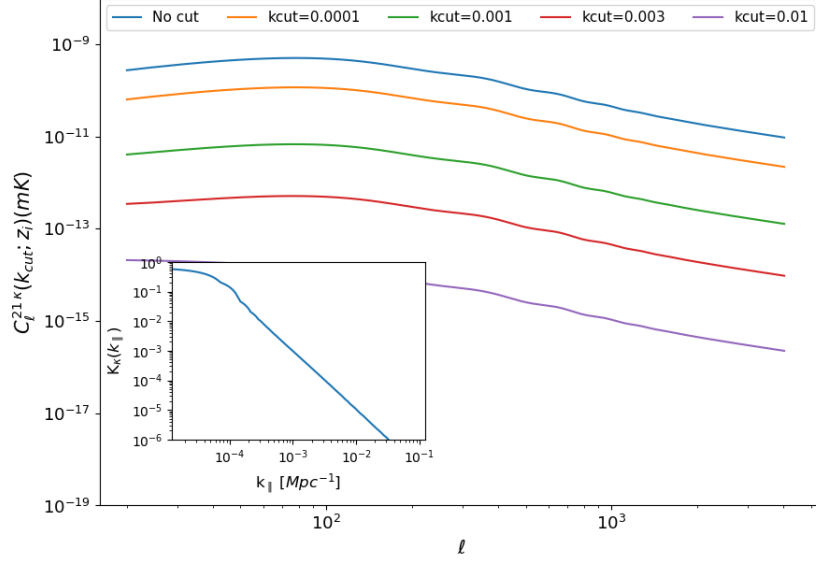


Figure 4.3: Cross-correlation signal as a function of removed k_{\parallel} modes. In the inset plot we show the CMB lensing convergence kernel in harmonic space which accounts for the significant drop in the signal as a function of radial wavenumber.

where we calculate the cross-variance as

$$\text{var}[C_{\ell,S}^{\kappa\delta T_{21}}] = (C_{\ell,S}^{\kappa\delta T_{21}}(y; z_i))^2 + (C_{\ell,S}^{\delta T_{21}}(y; z_i) + C_{\ell,N}^{\delta T_{21}}(y; z_i)) (C_{\ell,S}^{\kappa} + C_{\ell,N}^{\kappa}). \quad (4.18)$$

We show in Figure 4.3 how the cross-correlation signal drops sharply with $k_{\parallel} < k_{cut}$ modes removed. This feature can be explained by the CMB lensing convergence kernel in harmonic space shown in the inset plot in Figure 4.3. We see how the kernel drops sharply in magnitude as you go to higher k_{\parallel} modes.

In Figure 4.4(a) we show the SNR in the $k_{\perp} - k_{\parallel}$ plane for the cross-correlation without removing any k_{\parallel} modes. We see that in theory any statistical detection of the cross-correlation signal would occur at low k_{\parallel} modes. In practice, this cross-correlation signal is not detectable because HI intensity mapping experiments like HIRAX cannot access these modes. In 4.4(b) we see how the cross-correlation SNR is drastically reduced by a foreground treatment. Here we assume a foreground removal treatment would cost us the low k_{\parallel} modes. We remove

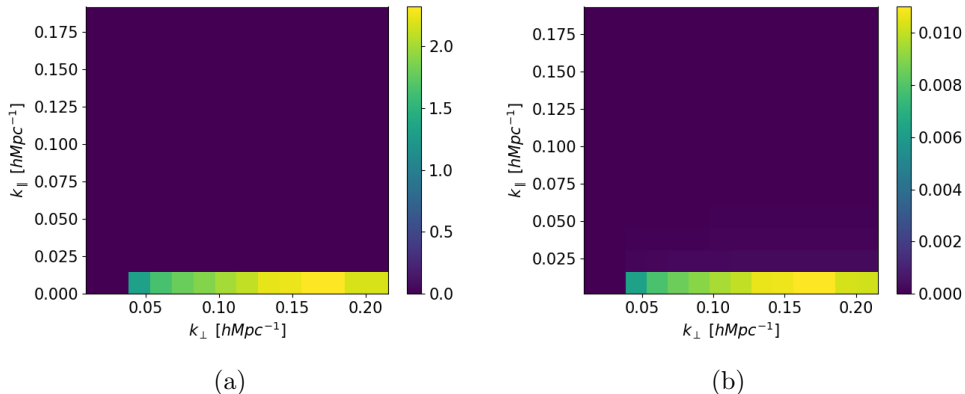


Figure 4.4: (a) The cross-correlation SNR as a function of k_{\perp} and k_{\parallel} modes for all HIRAX modes. (b) The cross-correlation SNR after removing modes $k_{\parallel} < 0.001\text{Mpc}^{-1}$ to accommodate a foreground removal treatment.

modes $k_{\parallel} < 0.001\text{Mpc}^{-1}$ which is an optimistic value relative to the nominal $k_{cut} = 0.01\text{Mpc}^{-1}$ value. Even at this optimistic level of k_{cut} we see the cross-correlation SNR drops significantly. This result is our motivation to construct the higher order correlation between the 21cm field and the CMB lensing convergence. In the next section we compute the 21-21- κ bispectrum by going to second order in the 21cm field and show that we can recover the lost signal using this configuration.

4.1.3 The Bispectrum Estimator

We have seen in the previous section how the two point cross-correlation function suffers signal loss due to foreground subtraction. Here we attempt to recover the cross-correlation using higher order correlations. We compute a three point function integrated bispectrum between the 21cm signal and CMB lensing convergence field. The integrated bispectrum is obtained by correlating the local power spectrum in some volume $V_{L,j} = L_{\parallel} * L_{\perp}^2$ (or position dependent power spectrum) with the mean overdensity of that volume [119]. Using this configuration we can reconstruct the information on the modes which are lost in 21cm measurements. To take advantage of this correlation we have to go to second order in the 21cm field since the first order bispectrum would vanish because these are Gaussian fields.

Here we correlate the 21cm position dependent power spectrum with the mean CMB lensing convergence field. We now need to compute the average CMB lensing convergence in a volume $V_{L,j}$ centered at \mathbf{r}_j along the past line cone. This corresponds to the volume covered by a given 21cm redshift bin with central redshift z_i and with length L_{\parallel} in the radial direction which corresponds to a given sub-band within the total bandwidth and width L_{\perp} in the transverse direction set by the telescope field-of-view. We first define radial and angular window functions, which we take to be top-hat functions in position space, hence, $W_L^{\parallel}(\mathbf{k}) = \text{sinc}(k_{\parallel}L_{\parallel})$ and $W_L^{\perp}(\mathbf{k}) = \text{sinc}(k_{\perp}L_{\perp})$. To obtain the average CMB in a given volume we use the integral convention for an average overdensity in a given region as

$$\bar{\delta}(r) = \int d^3r \delta(r) W_{L,\kappa}(\mathbf{r}) \quad (4.19)$$

which gives us the average CMB convergence in a volume as

$$\bar{\kappa}(\mathbf{r}_j; z_i) = \int d^3r \kappa(\mathbf{r}_j; z_i) W_{L,\kappa}(\mathbf{r}). \quad (4.20)$$

Using the expression for the convergence field Equation 4.3 we compute the average CMB convergence in the volume $V_{L,j} = L_{\parallel} * L_{\perp}^2$ centered at \mathbf{r}_j by

$$\bar{\kappa}(\mathbf{r}_j; z_i) = V_{L,j} [W_{\kappa}(\chi_{\parallel,i}) D(\chi_{\parallel,i}) / \chi_{\parallel,i}^2] \times \int \frac{d^3q'}{(2\pi)^3} \delta_m(-\mathbf{q}'; z=0) e^{-i\mathbf{r}_j \cdot \mathbf{q}'} W_{L,\kappa}(\mathbf{q}') \quad (4.21)$$

where $W_{L,\kappa}(\mathbf{q}') = W_{L,\kappa}^{\parallel}(q'_{\parallel}L_{\parallel}) \times W_{L,\kappa}^{\perp}(q'_{\perp}L_{\perp})$. We will correlate the average lensing convergence with the (local) 21cm power spectrum in the volume $V_{L,j}$. Now we have the local 21cm field as

$$\delta T_{21}(\boldsymbol{\ell}, y; \mathbf{r}_j, z_i) = \frac{1}{V_p(z_i)} \delta T_{21}(\mathbf{k}; \mathbf{r}_j, z_i) \quad (4.22)$$

and

$$\delta T_{21}(\mathbf{k}; \mathbf{r}_j, z_i) = V_{L,j} \int \frac{d^3k_1}{(2\pi)^3} \delta T_{21}(\mathbf{k} - \mathbf{k}_1; \mathbf{r}_j, z_i) W_{L,21}(\mathbf{k}_1) e^{-i\mathbf{k}_1 \cdot \mathbf{r}_j}, \quad (4.23)$$

where $V_p(z_i) = \chi_{\parallel,i}^2 r_{\nu,i}$ and $W_{L,21}(\mathbf{k}_1) = W_{L,21}^{\parallel}(\mathbf{k}_1) \times W_{L,21}^{\perp}(\mathbf{k}_1)$. The leading order term vanishes in cross-correlation with the lensing convergence due to it being a bispectrum of

Gaussian fields so we need to consider higher order terms in the 21cm field i.e. the cross-correlation between the ‘12’ and ‘21’ terms below.

The 21cm intensity field at second order is given by [120]

$$\delta T_{21}(\mathbf{k}; z_i) = \delta T_{21}^{(1)}(\mathbf{k}; z_i) + \frac{1}{\overline{T_b(z_i)}} \delta T_{21}^{(2)}(\mathbf{k}; z_i) \equiv \delta T_{21}^{(1)}(\mathbf{k}; z_i) + \overline{\delta T_{21}^{(2)}}(\mathbf{k}; z_i). \quad (4.24)$$

The second order short-wavelength mode is given by a coupling between a long-wavelength and small-wavelength mode

$$\delta T_{21}^{(2)}(\mathbf{k}; z_i) = \int \frac{d^3 q}{(2\pi)^3} Z_{HI}^{(2)}(\mathbf{q}, \mathbf{k} - \mathbf{q}; z_i) \frac{\delta T_{21}^{(1)}(\mathbf{k} - \mathbf{q}; z_i)}{Z_{HI}^{(1)}(\mathbf{k} - \mathbf{q}; z_i)} \frac{\delta T_{21}^{(1)}(\mathbf{q}; z_i)}{Z_{HI}^{(1)}(\mathbf{q}; z_i)}$$

where

$$\begin{aligned} Z_{HI}^{(2)}(\mathbf{q}, \mathbf{k} - \mathbf{q}; z_i) &= \frac{1}{2} b_{HI}^{(2)}(z_i) + b_{HI}^{(1)}(z_i) F_2(\mathbf{q}, \mathbf{k} - \mathbf{q}) + f(z_i) \left(\frac{k_{\parallel}}{k} \right)^2 G_2(\mathbf{q}, \mathbf{k} - \mathbf{q}) \\ &+ \frac{1}{2} f(z_i) k_{\parallel} \left[\frac{\mu_1}{q_1} \left(b_{HI}^{(1)}(z_i) + f(z_i) \mu_2^2 \right) + \frac{\mu_2}{q_2} \left(b_{HI}^{(1)}(z_i) + f(z_i) \mu_1^2 \right) \right] \end{aligned} \quad (4.25)$$

and the first order RSD term we have written compactly as

$$Z_{HI}^{(1)}(\mathbf{k}; z_i) = b_{HI}^{(1)}(z_i) + f(z_i) \mu_k^2. \quad (4.26)$$

The directional cosines μ_i are

$$\mu_1 = \frac{q_{\parallel}}{q_1}, \quad q_1 = |\mathbf{q}|; \quad \mu_2 = \frac{k_{\parallel} - q_{\parallel}}{q_2}, \quad q_2 = |\mathbf{k} - \mathbf{q}| \quad (4.27)$$

and the functions F_2 and G_2 are the kernels which depends on the matter density [120]

$$\begin{aligned} F_2(\mathbf{k}_1, \mathbf{k}_2) &= \frac{5}{7} + \frac{2}{7} \frac{(\mathbf{k}_1 \cdot \mathbf{k}_2)^2}{k_1^2 k_2^2} + \frac{1}{2} \frac{\mathbf{k}_1 \cdot \mathbf{k}_2}{k_1 k_2} \left(\frac{k_1}{k_2} + \frac{k_2}{k_1} \right), \\ G_2(\mathbf{k}_1, \mathbf{k}_2) &= \frac{3}{7} + \frac{4}{7} \frac{(\mathbf{k}_1 \cdot \mathbf{k}_2)^2}{k_1^2 k_2^2} + \frac{1}{2} \frac{\mathbf{k}_1 \cdot \mathbf{k}_2}{k_1 k_2} \left(\frac{k_1}{k_2} + \frac{k_2}{k_1} \right). \end{aligned} \quad (4.28)$$

We now compute the contribution from the two short-wavelength 21cm modes that enter the

bispectrum signal which is referred to as the position dependent power spectrum [119]. We calculate this contribution as

$$\begin{aligned}
P_{21}(k; \mathbf{r}_j, z_i) &= \frac{1}{V_{L,j}} \langle \delta T_{21}(\mathbf{k}; \mathbf{r}_j, z_i) \delta T_{21}^*(\mathbf{k}; \mathbf{r}_j, z_i) \rangle \\
&= V_{L,j} \int \frac{d^3 k_1}{(2\pi)^3} \int \frac{d^3 k'_1}{(2\pi)^3} W_{L,21}(\mathbf{k}_1) W_{L,21}^*(\mathbf{k}'_1) e^{-i(\mathbf{k}_1 - \mathbf{k}'_1) \cdot \mathbf{r}_j} \\
&\quad \times \overline{\delta T_{21}^{(2)}}(\mathbf{k} - \mathbf{k}_1; \mathbf{r}_j, z_i) \delta T_{21}^{(1)*}(\mathbf{k} - \mathbf{k}'_1; \mathbf{r}_j, z_i) + \{1 \leftrightarrow 2\} \\
&= V_{L,j} \int \frac{d^3 k_1}{(2\pi)^3} \int \frac{d^3 k'_1}{(2\pi)^3} W_{L,21}(\mathbf{k}_1) W_{L,21}^*(\mathbf{k}'_1) e^{-i(\mathbf{k}_1 - \mathbf{k}'_1) \cdot \mathbf{r}_j} \delta T_{21}^{(1)*}(\mathbf{k} - \mathbf{k}'_1) \\
&\quad \times \int \frac{d^3 q}{(2\pi)^3} \frac{Z_{HI}^{(2)}(\mathbf{q}, \mathbf{k} - \mathbf{k}_1 - \mathbf{q})}{Z_{HI}^{(1)}(\mathbf{k} - \mathbf{k}_1 - \mathbf{q})} \delta T_{21}^{(1)}(\mathbf{k} - \mathbf{k}_1 - \mathbf{q}) \frac{\delta T_{21}^{(1)}(\mathbf{q})}{\bar{T}_b(z_i) Z_{HI}^{(1)}(\mathbf{q})} + \{1 \leftrightarrow 2\} \\
&= V_{L,j} \int \frac{d^3 k_1}{(2\pi)^3} \int \frac{d^3 k'_1}{(2\pi)^3} W_{L,21}(\mathbf{k}_1) W_{L,21}^*(\mathbf{k}'_1) e^{-i(\mathbf{k}_1 - \mathbf{k}'_1) \cdot \mathbf{r}_j} \delta T_{21}^{(1)*}(\mathbf{k} - \mathbf{k}'_1) \\
&\quad \times \int \frac{d^3 q}{(2\pi)^3} \frac{Z_{HI}^{(2)}(\mathbf{q}, \mathbf{k} - \mathbf{k}_1 - \mathbf{q})}{Z_{HI}^{(1)}(\mathbf{k} - \mathbf{k}_1 - \mathbf{q})} \delta T_{21}^{(1)}(\mathbf{k} - \mathbf{k}_1 - \mathbf{q}) \delta_m(\mathbf{q}) + \{1 \leftrightarrow 2\}.
\end{aligned} \tag{4.29}$$

We now calculate the integrated bispectrum signal, which correlates the convergence field with the position dependent power spectrum in a sub volume centered at \mathbf{r}_j [121]. We calculate the 21-21- κ bispectrum signal as

$$\begin{aligned}
B_\ell^{2121\bar{\kappa}}(y; z_i) &= \langle \delta T_{21}(\boldsymbol{\ell}, y; \mathbf{r}_j, z_i) \delta T_{21}^*(\boldsymbol{\ell}, y; \mathbf{r}_j, z_i) \bar{\kappa}(\mathbf{r}_j; z_i) \rangle_{\mathbf{r}_j} \\
&= \left[\frac{V_{L,j}^2}{V_p(z_i)} \right] \left[\frac{W_\kappa(\chi_{\parallel,i}) D(\chi_{\parallel,i})}{\chi_{\parallel,i}^2} \right] \times \int \frac{d^3 k_1}{(2\pi)^3} \int \frac{d^3 k'_1}{(2\pi)^3} \int \frac{d^3 q}{(2\pi)^3} \int \frac{d^3 q'}{(2\pi)^3} \\
&\times W_{L,\kappa}(\mathbf{q}') W_{L,21}(\mathbf{k}_1) W_{L,21}^*(\mathbf{k}'_1) e^{-i(\mathbf{q}'+\mathbf{k}_1-\mathbf{k}'_1)\cdot\mathbf{r}_j} \left[\frac{Z_{HI}^{(2)}(\mathbf{q}, \mathbf{k} - \mathbf{k}_1 - \mathbf{q})}{Z_{HI}^{(1)}(\mathbf{k} - \mathbf{k}_1 - \mathbf{q})} \right. \\
&\left. \left\langle \delta T_{21}^{(1)}(\mathbf{k} - \mathbf{k}_1 - \mathbf{q}; z_i) \delta T_{21}^{(1)*}(\mathbf{k} - \mathbf{k}'_1; z_i) \delta_m(\mathbf{q}; z_i) \delta_m(-\mathbf{q}'; z=0) \right\rangle + \right. \\
&\left. \frac{Z_{HI}^{(2)}(\mathbf{q}, \mathbf{k} - \mathbf{k}'_1 - \mathbf{q})}{Z_{HI}^{(1)}(\mathbf{k} - \mathbf{k}'_1 - \mathbf{q})} \left\langle \delta T_{21}^{(1)*}(\mathbf{k} - \mathbf{k}'_1 - \mathbf{q}; z_i) \delta T_{21}^{(1)}(\mathbf{k} - \mathbf{k}_1; z_i) \delta_m^*(\mathbf{q}; z_i) \delta_m(-\mathbf{q}'; z=0) \right\rangle \right] \\
&= \left[\frac{V_{L,j}^2}{V_p(z_i)} \right] \left[\frac{W_\kappa(\chi_{\parallel,i}) D^4(\chi_{\parallel,i})}{\chi_{\parallel,i}^2} \right] \int \frac{d^3 q}{(2\pi)^3} W_{L,\kappa}(\mathbf{q}) P_m(\mathbf{q}; z=0) \int \frac{d^3 k_1}{(2\pi)^3} W_{L,21}(\mathbf{k}_1) W_{L,21}^*(\mathbf{k}_1 + \mathbf{q}) \\
&\times \left[\frac{Z_{HI}^{(2)}(-\mathbf{q}, \mathbf{k} - \mathbf{k}_1 - \mathbf{q})}{Z_{HI}^{(1)}(\mathbf{k} - \mathbf{k}_1 - \mathbf{q})} P_{21}(\mathbf{k} - \mathbf{k}_1 - \mathbf{q}; z=0) + \frac{Z_{HI}^{(2)}(\mathbf{q}, \mathbf{k} - \mathbf{k}_1)}{Z_{HI}^{(1)}(\mathbf{k} - \mathbf{k}_1)} P_{21}(\mathbf{k} - \mathbf{k}_1; z=0) \right] \\
&= \left[\frac{V_{L,j}^2}{V_p(z_i)} \right] \left[\frac{W_\kappa(\chi_{\parallel,i}) D^4(\chi_{\parallel,i})}{\chi_{\parallel,i}^2} \right] \int \frac{d^3 q}{(2\pi)^3} W_{L,\kappa}(\mathbf{q}) P_m(\mathbf{q}; z=0) \int \frac{d^3 k_1}{(2\pi)^3} W_{L,21}(\mathbf{k}_1) W_{L,21}^*(\mathbf{k}_1 + \mathbf{q}) \\
&\times \left\{ P_{21}(\mathbf{k}', z=0) \frac{Z_{HI}^{(2)}(\mathbf{q}, \mathbf{k}')}{Z_{HI}^{(1)}(\mathbf{k}')} + P_{21}(\mathbf{k} - \mathbf{k}_1, z=0) \frac{Z_{HI}^{(2)}(-\mathbf{q}, \mathbf{k} - \mathbf{k}_1)}{Z_{HI}^{(1)}(\mathbf{k} - \mathbf{k}_1)} \right\}
\end{aligned} \tag{4.30}$$

where we have set $\mathbf{k}' = \mathbf{k} - \mathbf{k}_1 - \mathbf{q}$. The expectation value of the other combinations vanishes in the squeezed triangle limit due to them being short mode-long mode combinations. Also note that $\int \frac{d^3 k_1}{(2\pi)^3} W_{L,21}(\mathbf{k}_1) W_{L,21}^*(\mathbf{k}_1 + \mathbf{q}) = W_{L,21}(\mathbf{q})/V_{L,j}$. Now if the wavenumber \mathbf{k} is much larger than the lensing wavenumber, \mathbf{q} , which is the case, then we can use the squeezed triangle approximation to simplify the term in brackets to obtain

$$\begin{aligned}
B_\ell^{2121\bar{\kappa}}(y; z_i) &= \left[\frac{V_{L,j} W_\kappa(\chi_{\parallel,i}) D^4(\chi_{\parallel,i})}{V_p(z_i) \chi_{\parallel,i}^2} \right] P_{21}(\mathbf{k}, z=0) \int \frac{d^3 q}{(2\pi)^3} W_{L,\kappa}(\mathbf{q}) W_{L,21}(\mathbf{q}) P_m(\mathbf{q}; z=0) \\
&\times \left\{ \frac{b_{HI}^{(2)}(\chi_{\parallel,i}) + 2(2\mu_k^2 - 1) f(\chi_{\parallel,i})(1 + f(\chi_{\parallel,i})\mu_k^2)}{b_{HI}^{(1)}(\chi_{\parallel,i}) + f(\chi_{\parallel,i})\mu_k^2} + \frac{1}{2}(1 + f(\chi_{\parallel,i})\mu_k^2) \left(3 - \frac{d \log P_m}{d \log k} \right) \right\}.
\end{aligned} \tag{4.31}$$

We show the detailed calculation of the squeezed approximation in Appendix B.1. In Figure 4.5 we show the bispectrum signal as a function of radial and transverse modes. We see that even though the bispectrum may be a weaker signal in amplitude than the two point

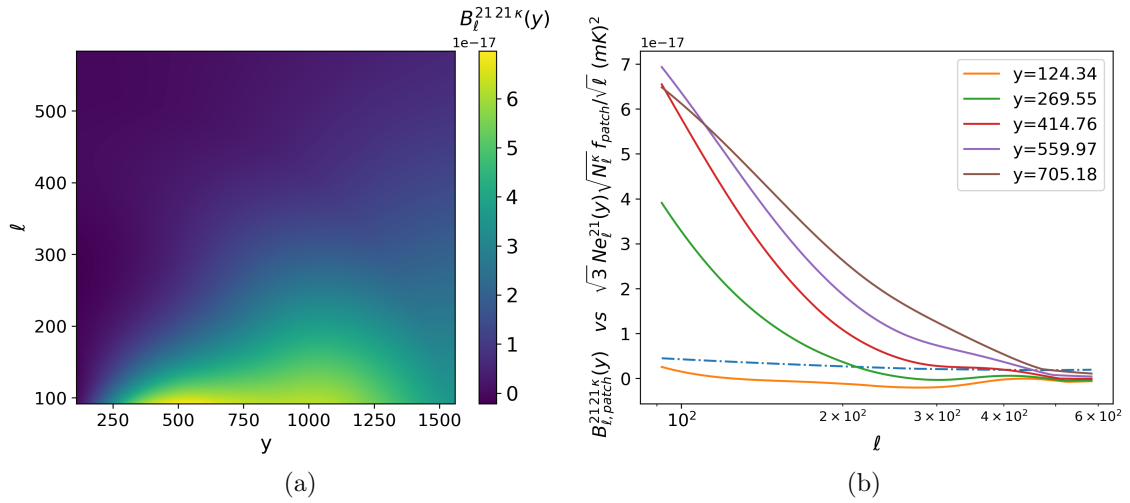


Figure 4.5: a) HI-HI- κ integrated bispectrum as a function of ℓ and y . (b) HI-HI- κ signal vs an effective leading order term in the instrument/reconstruction noise.

cross-correlation, it shows more promise for detection in relation to the leading order term of the bispectrum variance curve shown in blue. The leading order term in the bispectrum variance comes from the auto-noise terms and with the effective number of modes included. We now discuss the bispectrum variance and its detectability in the next section.

4.1.4 Detectability Of The Bispectrum

We now calculate the detectability of the bispectrum signal. We see from Figure 4.5 that the bispectrum in general is a weaker signal in amplitude than the two point cross-correlation but it is higher in relation to its variance. We now show the calculation of the bispectrum variance and thereafter use that to obtain signal to noise estimates for the bispectrum detectability.

We first describe the variances of the individual CMB lensing convergence and 21cm intensity probes respectively over their survey areas. The average CMB convergence variance is calculated as

$$\begin{aligned}
 \text{var}[\bar{\kappa}(r_j, z_i)]_{\text{survey}} &= f_{\text{sky}} \times \text{var}[\bar{\kappa}(r_j, z_i)]_{\text{sky}} = f_{\text{sky}} \langle \kappa(\ell = 0, z_i), \kappa^*(\ell = 0, z_i) \rangle_{r_j, \text{sky}} \\
 &= f_{\text{sky}} V_{L,j} \int \frac{d^3 q}{(2\pi)^3} |W_{L,\kappa}(\mathbf{q})|^2 C_{\ell,\kappa}^{\text{tot,sky}}(y)
 \end{aligned} \tag{4.32}$$

where $C_{\ell,\kappa}^{tot,sky}(y) = C_{\ell}^{\kappa,sky} + \mathcal{N}_{\ell}^{\kappa,sky}$. The 21cm variance is

$$\text{var}[\delta T_{21}(\ell, y; z_i)]_{\text{survey}} = \langle \delta T_{21}(\ell, y; z_i), \delta T_{21}^*(\ell, y; z_i) \rangle_{\text{survey}} = f_{\text{sky}} \left(C_{\ell,S}^{21,sky}(y) + C_{\ell,N}^{21,sky}(y) \right) \quad (4.33)$$

The integrated bispectrum signal over the survey area is just the signal in a patch multiplied by the number of patches:

$$B_{\ell,\text{sky}}^{2121\bar{\kappa}}(y; z_i) = N_{\text{patch}} B_{\ell,\text{patch}}^{2121\bar{\kappa}}(y; z_i). \quad (4.34)$$

Now we can calculate the variance of the integrated bispectrum as

$$\begin{aligned} \text{var} [B_{\ell,\text{sky}}^{2121\bar{\kappa}}(y; z_i)] &= \langle \delta T_{21}(\ell, y; z_i) \delta T_{21}(\ell, y; z_i) \bar{\kappa}(z_i) \delta T_{21}(\ell', y'; z_i) \delta T_{21}(\ell', y'; z_i) \bar{\kappa}'(z_i) \rangle \\ &= 3 \text{var}[\delta T_{21}(\ell, y; z_i)]^2 \times \text{var}[\bar{\kappa}(z_i)] + 12 \text{var}[\delta T_{21}(\ell, y; z_i)] \\ &\quad \times (C_{\ell}^{\bar{\kappa}\delta T_{21}}(y; z_i))^2 + 6 (B_{\ell,\text{sky}}^{2121\bar{\kappa}}(y; z_i))^2 \end{aligned} \quad (4.35)$$

where $\text{var}[\delta T_{21}(\ell, y; z_i)]$ and $\times \text{var}[\bar{\kappa}]$ have been computed in previous chapters. The full calculation for the variance is shown in Appendix B.1. For the bispectrum variance we require the cross-correlation spectrum between HI and the average lensing convergence, $C_{\ell}^{21\bar{\kappa}}(y; z_i)$, which is given by

$$C_{\ell}^{21\bar{\kappa}}(y; z_i) = \left[\frac{V_{L,j} W_{\kappa}(\chi_{\parallel,i}) D^2(\chi_{\parallel,i})}{V_p(z_i) \chi_{\parallel,i}^2} \right] \bar{T}_b(z_i) Z_{HI}^{(1)}(\mathbf{k}) W_{L,\kappa}(\mathbf{k}) W_{L,21}(\mathbf{k}) P_m(\mathbf{k}, z=0) \quad (4.36)$$

With the variance of the bispectrum at hand, we can now calculate the signal to noise ratio by

$$(SNR)^2 = (\Delta \tilde{\nu}_i S_{\text{area}}) \int_{y_{\min}}^{y_{\max}} \frac{dy}{(2\pi)} \int_{\ell_{\min}}^{\ell_{\max}} \frac{d\ell}{(2\pi)} \ell \frac{(B_{\ell,\text{sky}}^{2121\bar{\kappa}}(y; z_i))^2}{\text{var} [B_{\ell,\text{sky}}^{2121\bar{\kappa}}(y; z_i)]}. \quad (4.37)$$

In 4.6 we plot the bispectrum signal to noise ratio in the four bins over the HIRAX range. We plot the pixelized SNR computed by subdividing the $k_{\perp} - k_{\parallel}$ plane into 15 sub bins of width 0.01Mpc^{-1} and performing the SNR integral in Equation 4.37 in each bin. We find that in this case the SNR is much higher than the two point function cross-correlation case

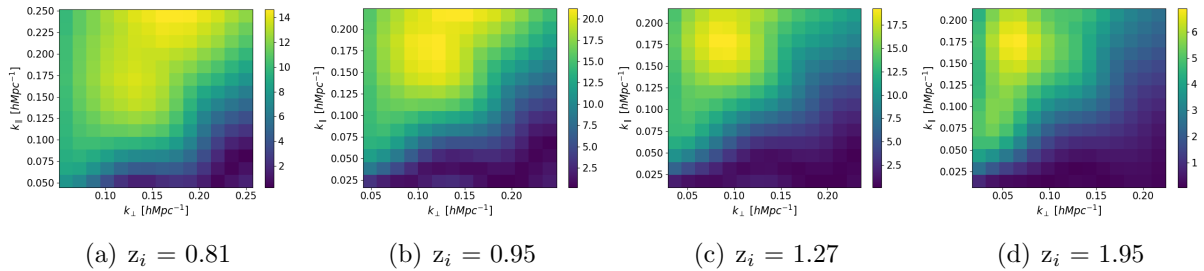


Figure 4.6: HI-HI- κ SNR in k_{\parallel} and k_{\perp} bins of width 0.01 Mpc^{-1} . We see how the bispectrum has much higher SNR values as compared to the two point correlation.

we showed in Figure 4.4. The SNR is not only larger in value but also extends further in the $k_{\perp} - k_{\parallel}$ plane. The SNR value in each of the four bins shows great promise for the detection of this signal as well as the potential to use this detection to constrain parameters. Another interesting feature of the bispectrum in constraining HI model parameters is that we model this signal to second order in the 21cm field. This means that we can constrain second order effects such as the second order HI bias.

4.1.5 Parameter Constraints

We now compute the parameter forecast constraints for both the cosmological and HI model parameters using the Fisher formalism method which we discussed in Section 3.3. We can use the bispectrum to add information to the HI autocorrelation constraints. With the bispectrum we can constrain the HI model parameters and include constraints on the HI bias at second order. We can also convert constraints of the distance scale parameters into cosmological constraints over the entire redshift range.

We differentiate the bispectrum shown in Equation 4.31 with respect to the linearly independent parameters $[A_{bao}, \sigma_8, \Omega_{HI}b_1, \Omega_{HI}f, b_2]$ similar to the HI case in Section 3.3. Note that here we drop the redshift dependence in the text for brevity like we did in Section 3.3 and we also rewrite the first and second order HI biases as $b_{HI}^{(1)} = b_1$ and $b_{HI}^{(2)} = b_2$. We show the bispectrum Fisher matrix derivatives for the cosmological and HI model parameters in Appendix A.

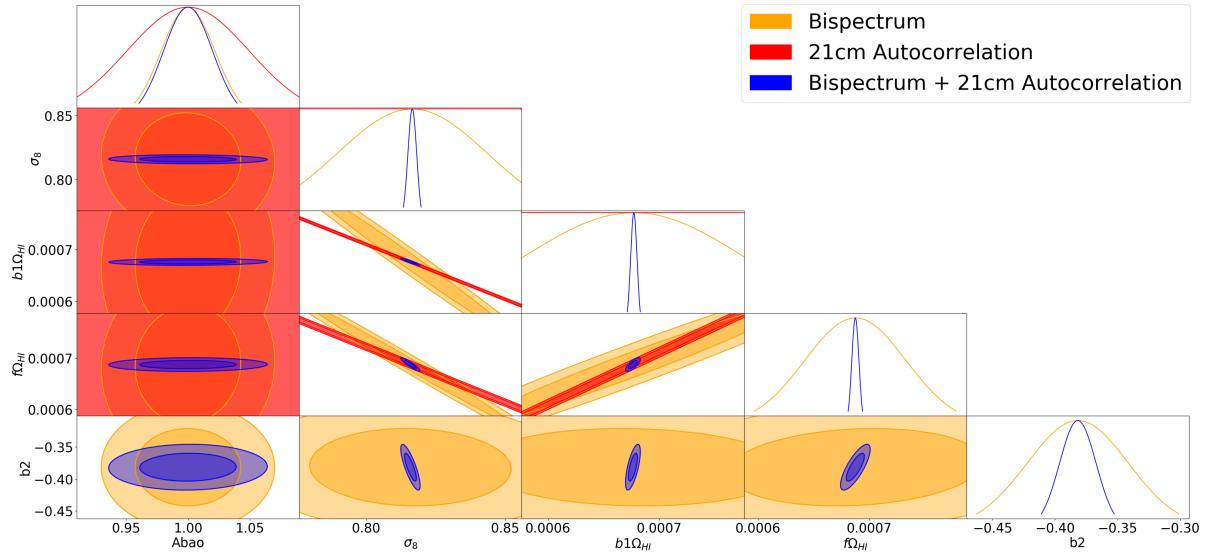


Figure 4.7: Forecast errors on the redshift dependent functions computed in the $z_i=1.2$ redshift bin.

We plot in Figure 4.7 the forecast constraints for the bispectrum on the HI model parameters. We also plot the 21cm autocorrelation constraints and the combined 21cm autocorrelation and bispectrum constraints. We show in Appendix B.2 that we can add the constraints from the 21cm autocorrelation and 21-21- κ together as if they are independent quantities because we get a negligible covariance between the probes. We see how by the adding the constraints from both probes we can make the constraints tighter particularly if the constraint ellipses are at different angles. This means that if a parameter enters each probe in a different way it can be constrained better by combination. One particularly interesting case of this is the $f - \sigma_8$ degeneracy. In most surveys this quantity enters as a single product $f\sigma_8$ and cannot be independently constrained. Here we see how the bispectrum together with the 21cm autocorrelation probe breaks this degeneracy. This happens because the parameters enter each probe differently. In the 21cm autocorrelation case the signal is proportional to $f\sigma_8^2$ but in the bispectrum it enters as $f\sigma_8^4$. This means the degeneracy angles are different which we see in Figure 4.7 and these parameters, with Ω_{HI} combined in f , can be independently constrained. We show in Figure 4.9(a) a close up view of the $f\Omega_{HI} - \sigma_8$ constraint. We note the combined constraints on the BAO amplitude is around 10%. We

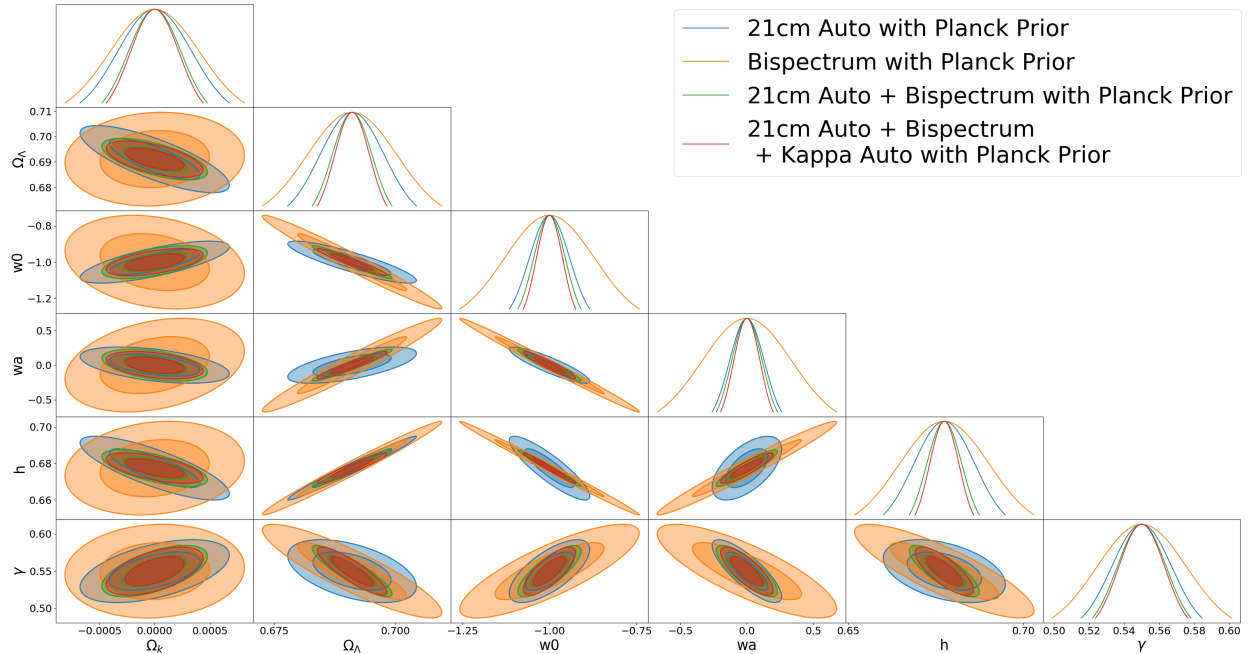


Figure 4.8: Cosmological parameter contour errors.

also see a stringent constraint on the second order bias of around 5%.

In Figure 4.8 we show how the bispectrum together with the 21cm autocorrelation can improve the constraints on cosmological parameters. We also show the impact of adding the CMB lensing convergence information on the cosmological parameters. For the purpose of this work we only consider the convergence constraints on σ_8 and the distance measures. We see that the cosmological constraints with Planck priors can improve the overall constraints considerably. We show in Figure 4.9(b) the close up plot of the dark energy equation of state parameter constraints. In this case with the bispectrum information the dark energy figure of merit value is around 927. This is an improvement by more than a factor of 2 on the 21cm autocorrelation constraint alone. This gives a fractional constraint on the equation of state parameters of 5%. The 21cm autocorrelation errors on the equation of state parameters were $\sigma_{w_0}^{21} = 0.047$ and $\sigma_{w_a}^{21} = 0.107$ but with the combined constraint here we get the errors down to $\sigma_{w_0}^{comb} = 0.031$ and $\sigma_{w_a}^{comb} = 0.081$. The combined curvature constraint on Ω_k is around 0.01% which would provide a significant measurement of the curvature of the universe.

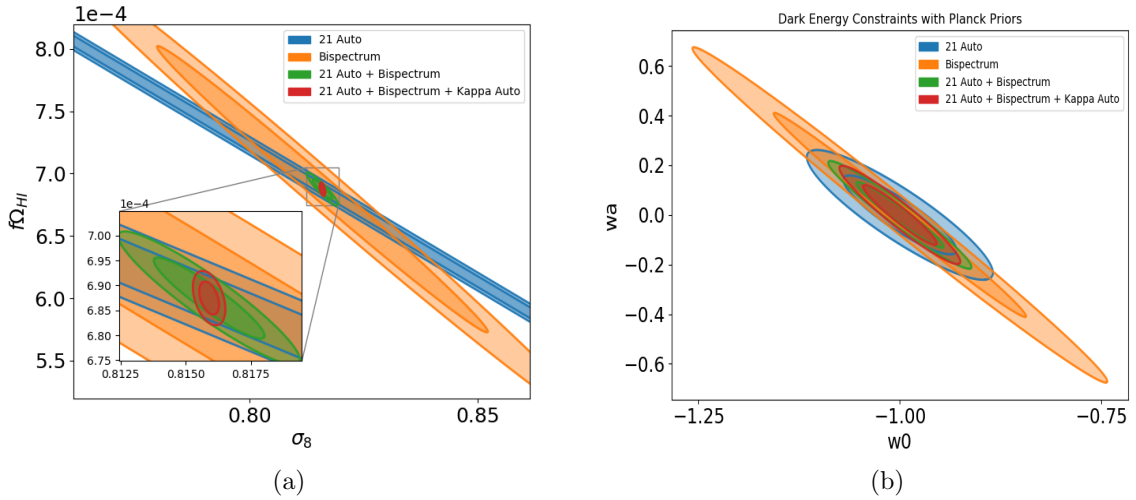


Figure 4.9: (a) Forecast constraints on f and σ_8 . (b) Forecast constraints on dark energy equation of state parameters.

4.2. HI IM-Galaxy Survey Cross-Correlation

Galaxy surveys have been used for a long time to measure the LSS and clustering of the baryonic matter in the universe. Measurements from the Two-degree-Field Galaxy Redshift Survey (2dFGRS) [4] and Sloan Digital Sky Survey (SDSS) [5] for example show the cosmic web structure which the galaxy distribution follows. We expect the distribution of galaxies to trace the underlying dark matter distribution just as in the 21cm case. Clustering measurements of galaxy surveys have already given us measurements on the BAO in the LSS autocorrelation functions [69] and in the matter power spectrum [9]. These galaxy clustering measurements have also provided some of the early high precision cosmological parameter constraints [8] as well as RSD constraints [122].

Galaxy surveys can be done using either spectroscopic surveys or photometric surveys. Spectroscopic galaxy surveys use spectral emissions from galaxy processes to identify galaxy populations. Spectroscopic instruments can be expensive to build and measurements of the sky requires longer observation times but we get higher resolution measurements and precise redshift information. Photometric galaxy surveys measure the optical light emitted

by galaxies by imaging through broadband filters. These surveys can measure the sky faster than spectroscopic surveys and are cheaper. One of the drawbacks of photometric surveys is that the redshift information is not well measured.

Cross-correlations between galaxy surveys and 21cm surveys can be used to make precision measurements on parameters like the galaxy and 21cm biases as well as the HI density fraction [37]. The first detection of the 21cm signal was made in cross-correlation with the optical galaxy survey DEEP2 and the Green Bank Telescope (GBT) [48]. Subsequent measurements were improved by the GBT and WiggleZ Dark Energy Survey [123]. Cross-correlating photometric measurements with 21cm surveys can be used to calibrate the photometric galaxy redshifts [50]. For these reasons, there is a lot of interest in cross-correlating the 21cm measurements with planned and recently developed next generation galaxy surveys such as the Dark Energy Survey (DES) [49], Dark Energy Spectroscopic Instrument (DESI) [124], Large Synoptic Survey Telescope (LSST) [125] and the Wide Field Infrared Survey Telescope (WFIRST) [126].

4.2.1 Spectroscopic Survey Cross-Correlations

We now study the prospects of cross-correlating HIRAX 21cm measurements with a spectroscopic galaxy survey like WFIRST. The WFIRST High Latitude Spectroscopic (HLS) survey will map out the distribution of galaxies covering a sky area of around 2000 deg² using the H_α and OIII emission line of galaxies [127]. Here we consider the OIII emission at its primary wavelength of 5007 Angstrom. The primary redshift range targets for the HLS are around $z \sim 1.05 - 2.77$.

Since we can access the redshift information of spectroscopic surveys we can obtain a 3D map of the universe. For this reason we can also obtain the power spectrum for all redshifts accessible to a given survey. We can therefore approximate the power spectrum in a given narrow redshift bin with central redshift z_i as

$$\delta_{gal}(\mathbf{k}; z_i) = W_{gal}(\chi_{||}(z_i))\delta_m(\mathbf{k}, z_i) \quad (4.38)$$

where z_i is the central redshift of a narrow bin. The galaxy density kernel is given as [46]

$$W_{gal}(\chi_{\parallel}) = N_{gal}^0 \frac{dN(z)}{dz} \frac{dz}{d\chi_{\parallel}} (b_{gal}(\chi_{\parallel}) + f\mu_k^2) + MB(\chi_{\parallel}) \quad (4.39)$$

where $\frac{dN(z)}{dz}$ describes the galaxy density of a sample population as a function of redshift and we normalize the galaxy density of a sample with the total number of galaxies measured so that $N_{gal}^0 = \frac{1}{\int dz' \frac{dN(z')}{dz'}}$. We show the simulated galaxy density distributions expected for a WFIRST-like experiment for both the H_{α} and OIII probes in Figure 4.10. Figure 4.10(a) shows that the H_{α} probe will perform much better at lower redshifts and gives an overall larger galaxy density measurement but the OIII probe will be able to obtain measurements up to much higher redshifts. The magnification bias is

$$MB(\chi_{\parallel}) = \frac{3}{2} \Omega_{m0} \left(\frac{H_0}{c} \right)^2 (1+z)(5s-2) f_g(\chi_{\parallel}), \quad (4.40)$$

where $f_g(\chi)$ denotes the normalized weight function described in [128] and is given as

$$f_g(\chi_{\parallel}) = \chi_{\parallel} \int_{\chi_{\parallel}}^{\chi_{\parallel}^*} d\chi'_{\parallel} \frac{\chi'_{\parallel} - \chi_{\parallel}}{\chi'_{\parallel}} \frac{dN(z)}{dz} \frac{dz}{d\chi'_{\parallel}}. \quad (4.41)$$

The logarithmic slope s of the number counts with some limiting magnitude m is given by

$$s = \frac{d \log N(< m)}{dm}. \quad (4.42)$$

The effect of the magnification is much smaller as compared to the galaxy distribution term $dN(z)/dz$ for scales relevant to our calculations and so we ignore it in our analysis. We use a parametric form for the galaxy bias from [129] as $b_{gal}(z) = b_{gal}^{(0)}(1 + b_{gal}^{(1)}z)$ where fiducial values for $b_{gal}^{(0)}$ and $b_{gal}^{(1)}$ are given in table 4.2.

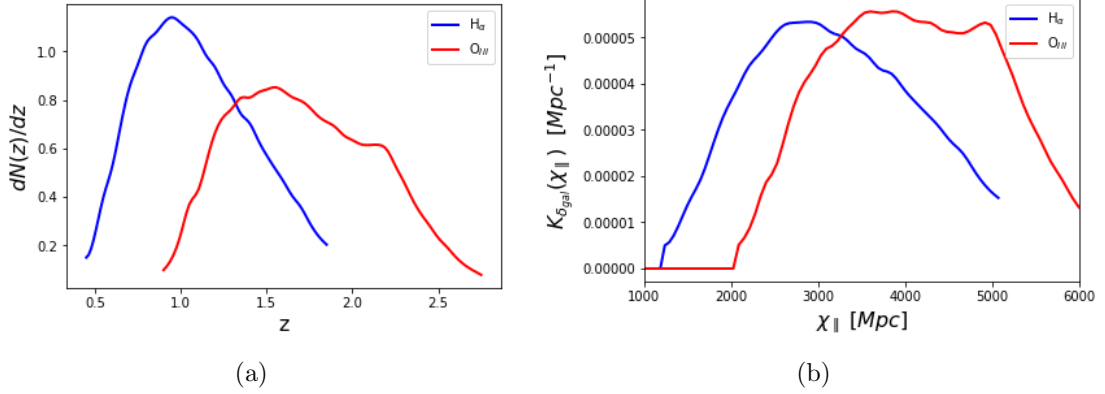


Figure 4.10: (a) Normalized galaxy density distribution for WFIRST. The plot shows how the H_α probe is expected to give a larger sample size in lower redshifts however, the O_{III} probe will be able to obtain measurements up to much higher redshifts. (b) Galaxy density kernel monopole ($\mu_k = 0$) as a function of comoving distance.

S_{area}	2000 deg ²
T_{obs}	0.59 years
Redshift range	0.45-1.85 [H_α] 0.9-2.75 [O_{III}]
N_{gal}	5182/deg ² [H_α] 685/deg ² [O_{III}]
$b_{gal}^{(0)}$	0.902
$b_{gal}^{(1)}$	0.444

Table 4.2: Specifications for WFIRST high latitude survey.

We first calculate the autocorrelation power spectra for the galaxy density probe using

$$\begin{aligned}
\langle \delta_{gal}(\mathbf{k}, z_i) \delta_{gal}^*(\mathbf{k}', z_i) \rangle &= (2\pi)^3 \delta_D^3(\mathbf{k} - \mathbf{k}') P_{gal}(\mathbf{k}, z_i) \\
\implies P_{gal}(\mathbf{k}, z_i) &= \int \frac{d^3 k'}{(2\pi)^3} \langle \delta_{gal}(\mathbf{k}, z_i) \delta_{gal}^*(\mathbf{k}', z_i) \rangle \\
&= \int \frac{d^3 k'}{(2\pi)^3} [W_{gal}(\chi_{\parallel}(z_i)) D(\chi_{\parallel}(z_i))]^2 \langle \delta_m(\mathbf{k}, z=0) \delta_m^*(\mathbf{k}', z=0) \rangle \quad (4.43) \\
&= \int \frac{d^3 k'}{(2\pi)^3} [K_{gal}]^2 \delta_D^3(\mathbf{k} - \mathbf{k}') P_m(k, z=0) \\
&= K_{gal}(\chi_{\parallel})^2 P_m(k, z=0).
\end{aligned}$$

where we have defined $K_{gal}(\chi_{\parallel}) = W_{gal}(\chi_{\parallel}(z_i)) D(\chi_{\parallel}(z_i))$ like we did in Section 4.1. We have plotted the galaxy kernel $K_{gal}(\chi_{\parallel})$ in Figure 4.10(b) which shows that probes will have the

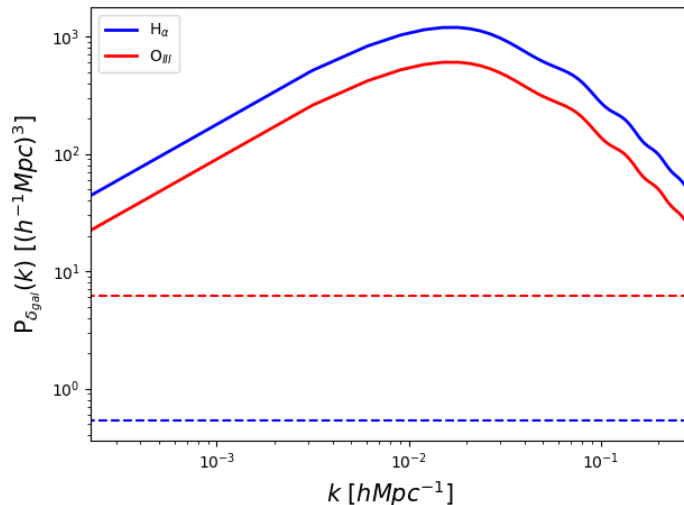


Figure 4.11: Galaxy density autocorrelation power spectrum and shot noise (dashed) computed for one redshift bin centered at $z_i=1.2$ with bin width $\Delta z=0.4$.

same magnitude kernels however they differ in their redshift comoving scales probed. This is expected since the galaxy distribution that enters the kernel is normalized by the total number of measured galaxies.

The noise associated with galaxy surveys is given by the shot noise contribution

$$P_N^{Shot} = \frac{1}{\bar{n}} = \frac{1}{N_g/V_{sur}} \quad (4.44)$$

where \bar{n} is the galaxy number density in a redshift bin, N_g is the number of galaxies in a redshift bin and the survey volume is given by [130]

$$V_{sur} = S_{area} \int_{z_{min}}^{z_{max}} dz \frac{dV}{dz d\Omega} = S_{area} \int_{z_{min}}^{z_{max}} dz \frac{c\chi_{\parallel}^2(z)}{H(z)}. \quad (4.45)$$

We show in Figure 4.11 the galaxy density autocorrelation power spectra spherically averaged over k and the shot noise for the H_{α} and O_{III} probes. We compute the power spectra at $z_i = 1.2$ with a bin width of $\Delta z = 0.4$. We can see from Figure 4.10 that at this redshift the galaxy densities and kernels are quite similar hence we expect that in Figure 4.11 the power spectra are quite similar in amplitude. The shot noise curves however are quite different

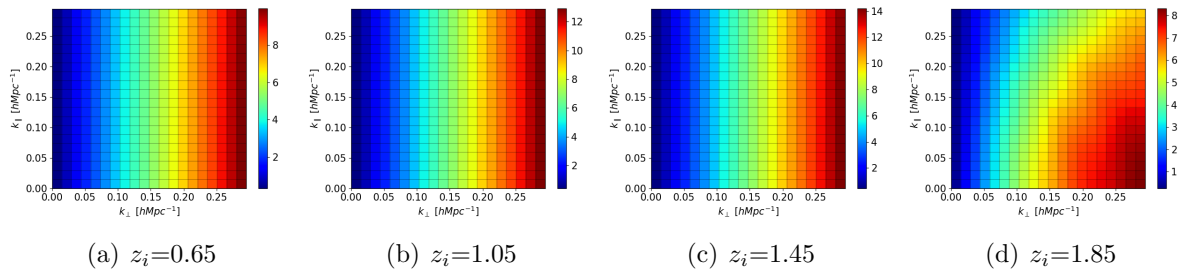


Figure 4.12: Galaxy density autocorrelation SNR for WFIRST for the H_α survey centered at the indicated redshift bins with redshift bin width of $\Delta z=0.4$. The plots show promising SNR levels in each redshift bin for the H_α probe up to $z=2$.

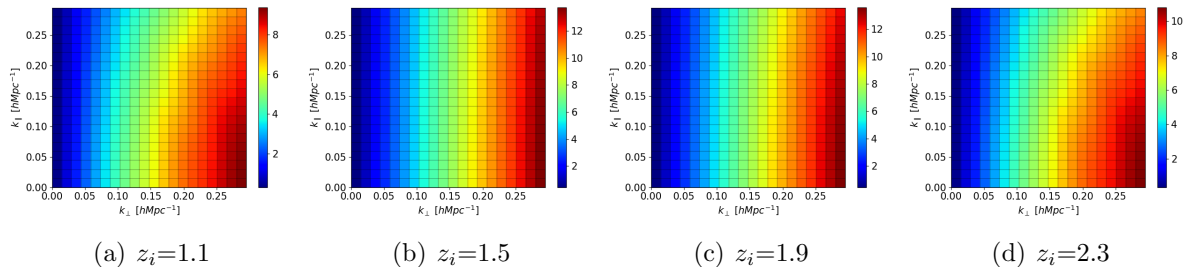


Figure 4.13: Galaxy density autocorrelation SNR for WFIRST for the O_{III} survey centered at the indicated redshift bins with redshift bin width of $\Delta z=0.4$. The plots show promising SNR levels in each redshift bin for the O_{III} probe which extends further than the H_α measurements out to $z=2.5$.

since the overall number of galaxies for the H_α probe is almost eight times the O_{III} case. For both cases however, we note the shot noise terms are well below the level of signal and we expect to make a significant detection of both probes. We quantify this level of detection now by computing the signal to noise ratio.

We estimate the signal to noise ratio for the galaxy density autocorrelation survey by

$$(SNR)^2 = \frac{V_{sur}}{2} \int_{k_{\parallel min}}^{k_{\parallel max}} \frac{dk_{\parallel}}{2\pi} \int_{k_{\perp min}}^{k_{\perp max}} \frac{dk_{\perp}}{(2\pi)^2} \left[\frac{P_{gal}(\mathbf{k}; z_i)}{P_{gal}(\mathbf{k}; z_i) + P_N^{Shot}} \right]^2. \quad (4.46)$$

For the spectroscopic galaxy survey we restrict our k_{max} to the linear scales $k < 0.14 \text{Mpc}^{-1}$. We show in Figures 4.12 and 4.13 the SNR computed for the spectroscopic survey autocorrelation measurements. Both spectroscopic probes show promise in their autocorrelation measurements. Here we see high SNR in each of the four bins and these can be used to

constrain the galaxy biases and the BAO signal. Due to the nature of the probes, the O_{III} measurements can extend further out in redshift and we see how the SNR values are promising out to $z > 2.3$. The H_α probe on the other hand will be able to obtain high precision measurements of the lower redshift universe down to $z < 0.65$. We now focus on calculating the cross-correlation signal between the 21cm measurements and the spectroscopic galaxy surveys.

We calculate the 21cm-spectroscopic galaxy cross-correlation power spectrum as

$$\langle \delta T_{21}(\mathbf{k}; z_i) \delta_{gal}^*(\mathbf{k}') \rangle = (2\pi)^3 \delta_D^3(\mathbf{k} - \mathbf{k}') P_{21-gal}(k; z_i) \quad (4.47)$$

to get

$$\begin{aligned} P_{21-gal}(\mathbf{k}; z_i) &= \bar{T}(z_i) [b_{HI} + f\mu_k^2] D(z_i)^2 W_{gal}(z_i) \int \frac{d^3 k'}{(2\pi)^3} \langle \delta_m(\mathbf{k}) \delta_m^*(\mathbf{k}') \rangle \\ &= \bar{T}(z_i) [b_{HI} + f\mu_k^2] D(z_i)^2 W_{gal}(z_i) P_m(k; z = 0). \end{aligned} \quad (4.48)$$

where this derivation assumes that the galaxies perfectly trace the HI distribution. We relax this assumption when computing forecast constraints by introducing the correlation coefficient r_{21-gal} .

The error on the cross-correlation is obtained from the variance estimator

$$\text{var}[P_{21-gal}(\mathbf{k}; z_i)] = P_{21-gal}^2(\mathbf{k}; z_i) + P_{21}^{Tot}(\mathbf{k}; z_i) P_{gal}^{Tot}(\mathbf{k}; z_i) \quad (4.49)$$

where $P_{21}^{Tot} = P_{21} + N_{21}$ and $P_{gal}^{Tot} = P_{gal} + N_{gal}$. Recall that the 3D power spectrum in Fourier space is related to the observational space power spectrum by the volume factor $V_p(z_i)$ such that

$$P_{21}(\mathbf{k}, z_i) = C_{\ell,S}^{21} V_p(z_i), \quad N_{21}(\mathbf{k}, z_i) = C_{\ell,N}^{21} V_p(z_i). \quad (4.50)$$

In Figure 4.14 we show the spherically averaged cross-correlation signal versus the cross-correlation variance term shown by the dashed curves. The variance drops below the cross-correlation signal at around $k \approx 0.03 h \text{Mpc}^{-1}$, which indicates we can make our detection of

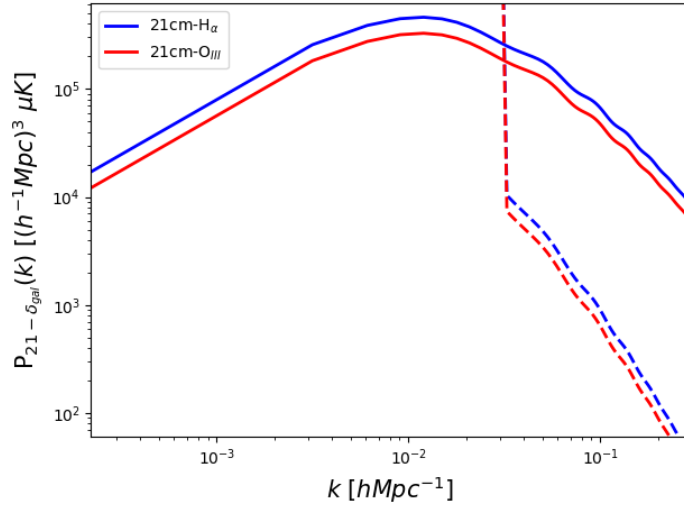


Figure 4.14: The 21cm-spectroscopic galaxy cross-correlation power spectrum and cross-correlation variance (dashed) for both the H_α and $OIII$ probes. The power spectra is computed for a redshift bin centered at $z_i=1.2$ and bin width $\Delta z=0.4$.

this signal only on these scales. We restrict our analysis to the linear regime, meaning we don't consider the spectra above $k > 0.2h\text{Mpc}^{-1}$ even if there may be significant signal here.

The variance for the cross-correlation can be used to determine the signal to noise ratio as

$$(SNR)^2 = \frac{V_{sur}}{2} \int_{k_{\parallel min}}^{k_{\parallel max}} \frac{dk_{\parallel}}{2\pi} \int_{k_{\perp min}}^{k_{\perp max}} \frac{dk_{\perp}}{(2\pi)^2} \left[\frac{(P_{21-gal}(\mathbf{k}; z_i))^2}{\text{var}[P_{21-gal}(\mathbf{k}; z_i)]} \right] \quad (4.51)$$

In Figures 4.15 and 4.16 we show the SNR for the cross-correlation measurements. For the 21cm- H_α cross-correlation we only consider 3 redshift bins of width $\Delta z = 0.4$ because of the limited redshift overlap between the two probes. For the cross-correlation with both H_α and $OIII$ probes there is good SNR which is promising for high precision measurements and signal detection. These SNR levels indicates there can be significant constraints on galaxy and 21cm parameters as well as the underlying cosmological parameters. From Figures 4.15 and 4.16 we see that the cross-correlation measurements improve the overall range of detection for the 21cm autocorrelation signal. The cross-correlation signal to noise also shows that the detection for the galaxy density is higher in this cross-correlation than in the autocorrelation measurements.

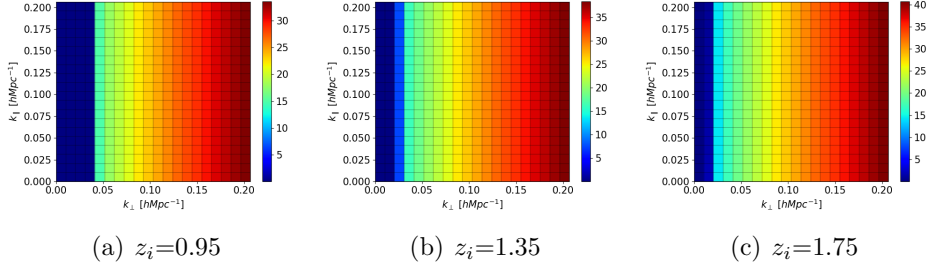


Figure 4.15: The cross-correlation SNR plots in three redshifts bins of width $\Delta z=0.4$ for the 21cm- H_α survey.

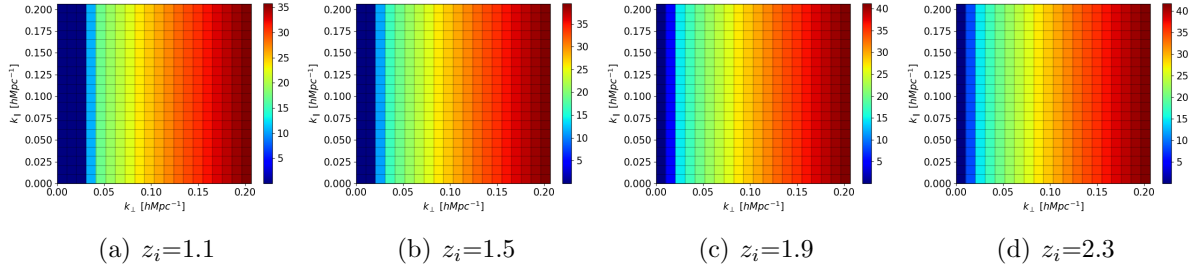


Figure 4.16: The cross-correlation SNR plots in the four redshifts bins of width $\Delta z=0.4$ for the 21cm- O_{III} survey.

Parameter Constraints

Here we show the possible parameter forecast constraints to the HI and galaxy parameters from the 21cm-spectroscopic cross-correlation. We compute the constraints using the Fisher matrix discussed in Section 3.3. Here we constrain the parameters $\{A_{BAO}, r_{21-gal}^{(0)}, r_{21-gal}^{(1)}, \gamma, A_{HI}^{(0)}, A_{HI}^{(1)}, A_{gal}^{(0)}, A_{gal}^{(1)}\}$ where $r_{21-gal}(z) = r_{21-gal}^{(0)} + r_{21-gal}^{(1)}z$ is the correlation coefficient which multiplies the cross-correlation signal. We have also defined $A_{HI}^{(0)} = b_{HI}^{(0)}\Omega_{HI}^{(0)}\sigma_8$ and $A_{HI}^{(1)} = b_{HI}^{(1)}\Omega_{HI}^{(0)}\sigma_8$. We use a similar parameterisation for the galaxy density parameters $A_{gal}^{(0)} = b_{gal}^{(0)}N_{gal}^{(0)}\sigma_8$ and $A_{gal}^{(1)} = b_{gal}^{(1)}N_{gal}^{(0)}\sigma_8$. Here we have parameterised the biases and HI fraction as

$$b_{HI}(z) = b_{HI}^{(0)} + b_{HI}^{(1)}z \quad (4.52)$$

$$b_{gal}(z) = b_{gal}^{(0)} + b_{gal}^{(1)}z \quad (4.53)$$

$$\Omega_{HI}(z) = \Omega_{HI}^{(0)} \left(1 + \Omega_{HI}^{(1)}z + \Omega_{HI}^{(2)}z^2 \right). \quad (4.54)$$

We have included quadratic terms in our fiducial model for $\Omega_{HI}(z)$ but we only vary the leading term. The reason we consider a redshift parameterisation here is because we want to constrain the redshift evolution of the cross-correlation and overall amplitude parameters. The galaxy density normalization $N_{gal}^{(0)}$ is just the total number of galaxies for the given survey integrated over its entire redshift range. We list the parameter values of our parameterisation in Table 4.3

$b_{HI}^{(0)}$	0.666
$b_{HI}^{(1)}$	0.178
$\Omega_{HI}^{(0)}$	4.830×10^{-4}
$\Omega_{HI}^{(1)}$	3.886×10^{-4}
$\Omega_{HI}^{(2)}$	6.512×10^{-5}
$N_{gal}^{(0)}$	$1/5182 \text{deg}^2 [\text{H}\alpha], 1/685 \text{deg}^2 [\text{OIII}]$
$b_{gal}^{(0)}$	0.902
$b_{gal}^{(1)}$	0.400
r_{21-gal}^0	1.0
r_{21-gal}^1	0.0

Table 4.3: HI and spectroscopic galaxy parametric model values.

We expand the galaxy power spectrum and cross-correlation in terms of the explicit dependencies like we did in the 21cm case to get

$$P_{gal}(\mathbf{k}, z_i) = n^2(z_i) (b_{gal}(z_i) + f(z_i)\mu_k^2)^2 D^2(z_i) (\sigma_8/\sigma_8^{fid})^2 (1 + A_{bao}f_{bao}(\mathbf{k})) P_m^{smooth}(k) \quad (4.55)$$

and the cross-correlation signal as

$$P_{21-gal}(\mathbf{k}, z_i) = \bar{T}(z_i) (b_{HI}(z_i) + f(z_i)\mu_k^2) n(z_i) (b_{gal}(z_i) + f(z_i)\mu_k^2) \times \left(\frac{\sigma_8}{\sigma_8^{fid}} \right)^2 r_{21-gal}(z_i) (1 + A_{bao}f_{bao}(\mathbf{k})) D^2(z_i) P_m^{smooth}(k). \quad (4.56)$$

In Figures 4.17 and 4.18 we show the combined constraints on the HI and galaxy density model parameters. We also show (green curves) the constraints if we only constrain the constant terms in our parametric form and fix the linear order ($r_{21-gal}^{(1)}, b_{HI}^{(1)}, b_{gal}^{(1)}$) terms. We

see that even if we vary all parameters up to linear order in redshift we can obtain extremely tight constraints on the model parameters. This suggests that the cross-correlation can measure redshift evolution in the cross-correlation and overall amplitude parameters. We can constrain the combined quantities A_{HI} and A_{gal} well below the percent level. We can obtain a 4% constraint on A_{BAO} and γ . We can also constrain the correlation coefficient parameters to below 2%. The high precision constraints on the model parameters from this cross-correlation is promising for constraints on the cosmological parameters which we plan to study in future work.

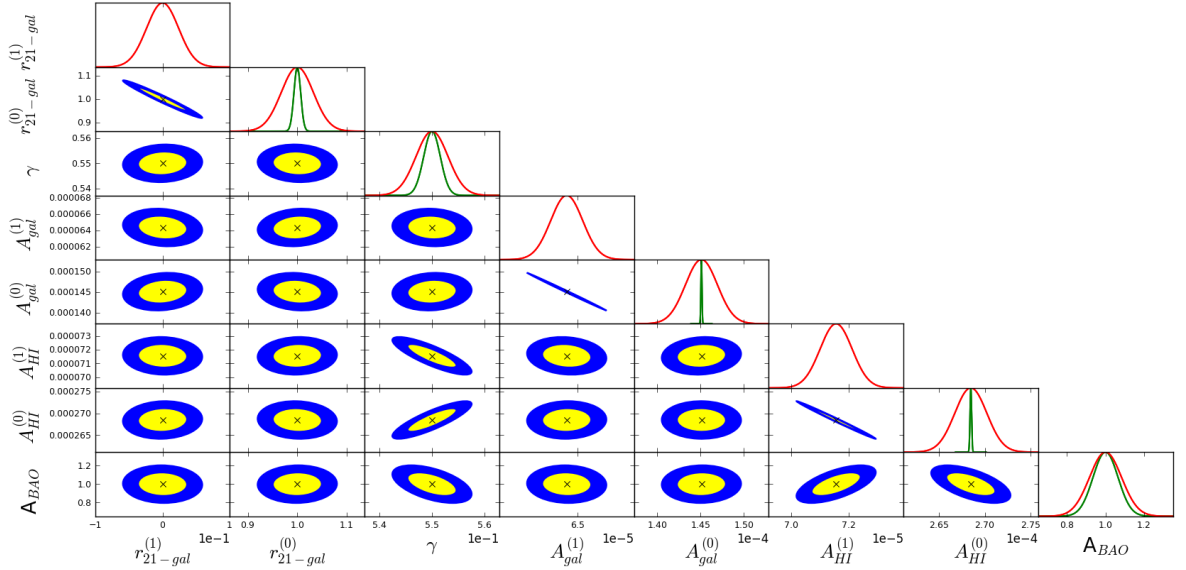


Figure 4.17: Forecast constraints on the HI and H_α galaxy survey parameters from the combined 21cm autocorrelation, spectroscopic galaxy density autocorrelation and cross-correlation probes. The yellow contours show 1σ errors and the blue contours show 2σ errors. The green curves show the constraints if we only vary the leading order terms in the parametric equations.

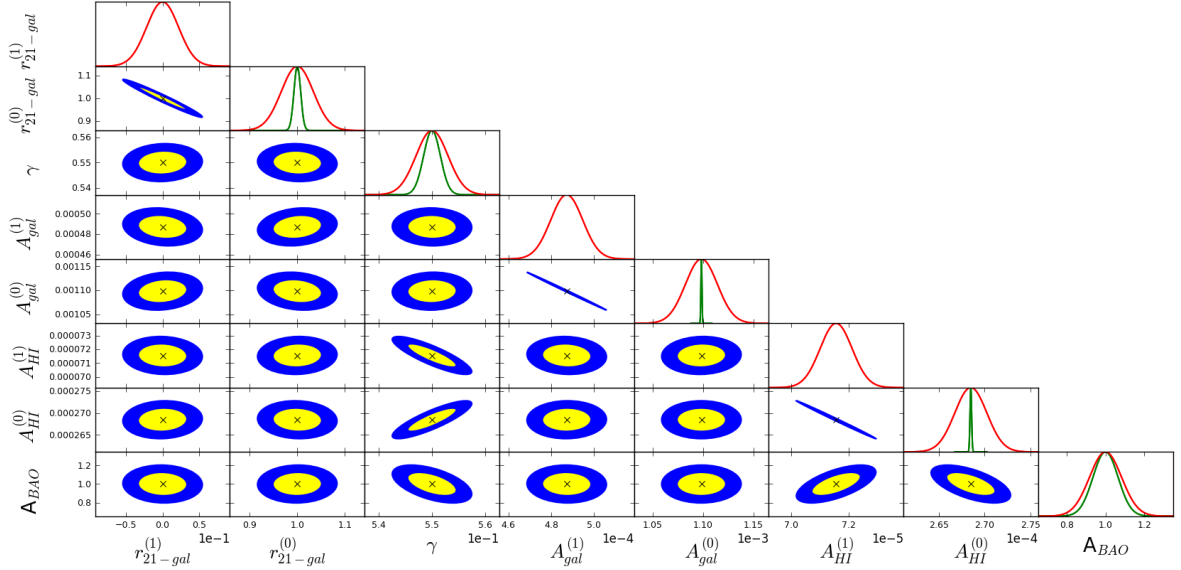


Figure 4.18: Forecast constraints on the HI and O_{III} galaxy survey parameters from the combined 21cm autocorrelation, spectroscopic galaxy density autocorrelation and cross-correlation probes. The yellow contours show 1σ errors and the blue contours show 2σ errors. The green curves show the constraints if we only vary the leading order terms in the parametric equations.

4.2.2 Photometric Survey Cross-Correlations

The modelling of the photometric galaxy survey is done in the same way as the spectroscopic case. The difference between the way we model these surveys is mainly in the galaxy density distribution. We also model the photometric signal in the angular space like the CMB lensing convergence since the redshift distributions are not tightly constrained. Here we consider an LSST type galaxy distribution as discussed in the LSST science book [125]. We summarise the LSST photometric survey specifications in Table 4.4. LSST will survey the southern sky meaning we expect to have excellent observational overlap with HIRAX.

S_{area}	20 000 deg ²
Effective aperture	6.7 m
Redshift range	$0 < z < 4$
Field of view	9.6 deg ²

Table 4.4: Specifications for LSST photometric galaxy survey.

In the angular space we can write the photometric galaxy density field as

$$\delta_{gal}(\boldsymbol{\ell}) = \int_0^{\chi_{\parallel}^*} d\chi_{\parallel} \frac{W_{gal}(\chi_{\parallel})}{\chi_{\parallel}^2} D(\chi_{\parallel}) \int \frac{dk_{\parallel}}{2\pi} e^{ik_{\parallel}\chi_{\parallel}} \delta_m(\boldsymbol{\ell}, k_{\parallel}, z=0). \quad (4.57)$$

We then calculate the autocorrelation angular power spectrum for the photometric galaxy survey as

$$\langle \delta_{gal}(\boldsymbol{\ell}) \delta_{gal}(\boldsymbol{\ell}')^* \rangle = (2\pi)^2 \delta_D^2(\boldsymbol{\ell} - \boldsymbol{\ell}') C_{\ell}^{gal} \quad (4.58)$$

to obtain

$$\begin{aligned} C_{\ell}^{gal} &= \int \frac{d^2\ell'}{(2\pi)^2} \langle \delta_{gal}(\boldsymbol{\ell}) \delta_{gal}(\boldsymbol{\ell}')^* \rangle \\ &= \int \frac{d^2\ell'}{(2\pi)^2} \int_0^{\chi_{\parallel}^*} d\chi_{\parallel} \frac{W_{gal}(\chi_{\parallel})}{\chi_{\parallel}^2} D(\chi_{\parallel}) \int \frac{dk_{\parallel}}{2\pi} e^{ik_{\parallel}\chi_{\parallel}} \int_0^{\chi_{\parallel}^*} d\chi'_{\parallel} \frac{W_{gal}(\chi'_{\parallel})}{\chi_{\parallel}'^2} D(\chi'_{\parallel}) \times \\ &\quad \int \frac{dk'_{\parallel}}{2\pi} e^{-ik'_{\parallel}\chi'_{\parallel}} \langle \delta_m(\mathbf{k}, z=0) \delta_m^*(\mathbf{k}', z=0) \rangle \\ &= \int \frac{d^2\ell'}{(2\pi)^2} \int_0^{\chi_{\parallel}^*} d\chi_{\parallel} \frac{W_{gal}(\chi_{\parallel})}{\chi_{\parallel}^2} D(\chi_{\parallel}) \int \frac{dk_{\parallel}}{2\pi} e^{ik_{\parallel}\chi_{\parallel}} \int_0^{\chi_{\parallel}^*} d\chi'_{\parallel} \frac{W_{gal}(\chi'_{\parallel})}{\chi_{\parallel}'^2} D(\chi'_{\parallel}) \times \\ &\quad \int \frac{dk'_{\parallel}}{2\pi} e^{-ik'_{\parallel}\chi'_{\parallel}} \delta_D^2(\mathbf{k}_{\perp} - \mathbf{k}'_{\perp}) \delta_D(k_{\parallel} - k'_{\parallel}) P_m(\mathbf{k}, z=0) \\ &= \int \frac{dk_{\parallel}}{2\pi} \int_0^{\chi_{\parallel}^*} d\chi_{\parallel} \int_0^{\chi_{\parallel}^*} d\chi'_{\parallel} e^{ik_{\parallel}(\chi_{\parallel} - \chi'_{\parallel})} W_{gal}(\chi_{\parallel}) D(\chi_{\parallel}) W_{gal}(\chi'_{\parallel}) D(\chi'_{\parallel}) P_m(\boldsymbol{\ell}, k_{\parallel}, z=0) \end{aligned} \quad (4.59)$$

The photometric survey noise is just the angular projection of the shot noise which is just scaled by the volume factor $V_p(z_i)$ to give

$$N_{\ell}^{gal}(z_i) = \frac{P_N^{shot}}{V_p(z_i)}. \quad (4.60)$$

With the power spectrum and noise expressions in hand we can then compute our signal to noise estimator as

$$(SNR)^2 = \sum_{\ell} 2\ell \Delta \ell f_{sky} \left(\frac{C_{\ell}^{gal}}{C_{\ell}^{gal} + N_{\ell}^{gal}} \right)^2. \quad (4.61)$$

We show in the Figure 4.19 the photometric galaxy survey power spectrum and the SNR for

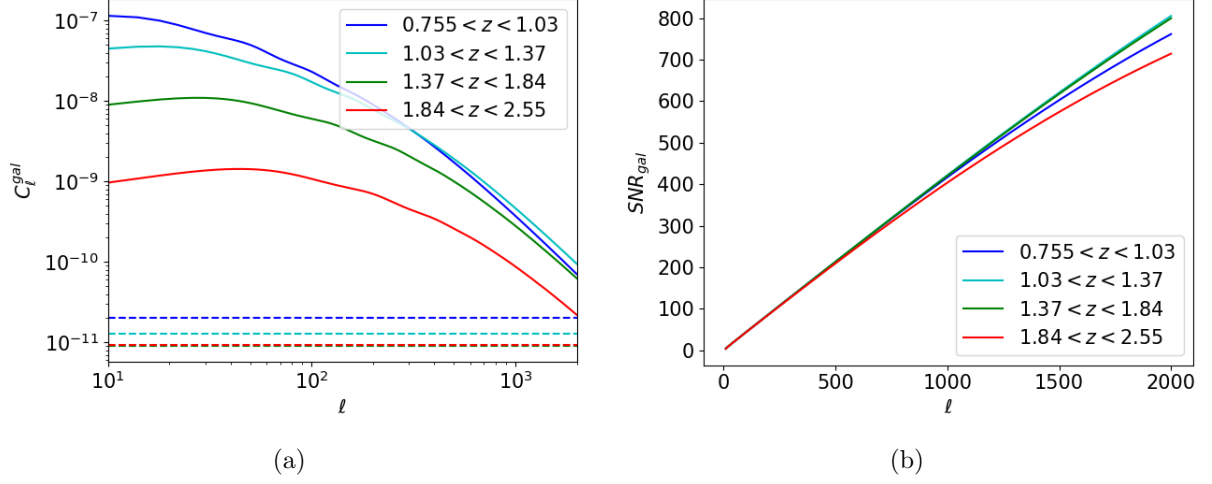


Figure 4.19: (a) Photometric galaxy survey power spectra computed in 100MHz bins over the HIRAX frequency range. The corresponding shot noise levels for each bin is shown by the dashed curves.(b) The cumulative SNR in the 100MHz bins for the Photometric galaxy survey with LSST experimental specifications.

the LSST experiment. We compute the signal and SNR in redshift range overlap with HIRAX of $0.755 < z < 2.55$ here since it is the relevant range for the cross-correlation. We consider four bins in this range for the photometric autocorrelation and the cross-correlation. In Figure 4.19(b) we show the large SNR detection level that the LSST experiment is expected to make with a cumulative SNR around 800. We sum the SNR at individual ℓ modes in quadrature to obtain the cumulative SNR. This gives us information tells us over what range of ℓ the cross-correlation signal builds up the most.

We now calculate the 21cm-photometric galaxy survey cross-correlation power spectrum as

$$\langle \delta T_{21}(\boldsymbol{\ell}, y; z_i) \delta_{gal}^*(\boldsymbol{\ell}') \rangle = (2\pi)^2 \delta_D^2(\boldsymbol{\ell} - \boldsymbol{\ell}') C_\ell^{21-gal} \quad (4.62)$$

to get the cross-correlation signal as

$$\begin{aligned}
C_\ell^{21-gal}(y; z_i) &= \int \frac{d^2\ell'}{(2\pi)^2} \langle \delta T_{21}(\boldsymbol{\ell}, y; z_i) \delta_{gal}^*(\boldsymbol{\ell}') \rangle \\
&= \int \frac{d^2\ell'}{(2\pi)^2} \bar{T}_b(z_i) (b_{HI}(z_i) + f(z_i)\mu_k^2) \frac{D(z_i)}{V_p(z_i)} \int_0^{\chi_\parallel^*} d\chi'_\parallel \frac{W_{gal}(\chi'_\parallel)}{\chi'^2_\parallel} D(\chi'_\parallel) \times \\
&\quad \int \frac{dk'_\parallel}{2\pi} e^{-ik'_\parallel\chi'_\parallel} \langle \delta_m(\mathbf{k}, z=0) \delta_m^*(\mathbf{k}', z=0) \rangle \\
&= \int \frac{d^2\ell'}{(2\pi)^2} \bar{T}_b(z_i) (b_{HI}(z_i) + f(z_i)\mu_k^2) \frac{D(z_i)}{V_p(z_i)} \int_0^{\chi_\parallel^*} d\chi'_\parallel \frac{W_{gal}(\chi'_\parallel)}{\chi'^2_\parallel} D(\chi'_\parallel) \times \\
&\quad \int \frac{dk'_\parallel}{2\pi} e^{-ik'_\parallel\chi'_\parallel} \delta_D^2(\mathbf{k}_\perp - \mathbf{k}'_\perp) \delta_D(k_\parallel - k'_\parallel) P_m(\mathbf{k}, z=0) \\
&= \bar{T}_b(z_i) (b_{HI}(z_i) + f(z_i)\mu_k^2) D(z_i) K_{gal} \left(\frac{y}{r_{\nu,i}} \right) \frac{P_m \left(\frac{\boldsymbol{\ell}}{\chi_\parallel}, \frac{y}{r_{\nu,i}}; z=0 \right)}{V_p(z_i)}.
\end{aligned} \tag{4.63}$$

Like in the CMB lensing convergence case we have defined the harmonic space kernel as

$$K_{gal}(k_\parallel) = \int d\chi'_\parallel e^{-ik'_\parallel\chi'_\parallel} W_{gal}(\chi'_\parallel) D(\chi'_\parallel). \tag{4.64}$$

The variance for this cross-correlation will also be similar to the CMB lensing convergence given by

$$\text{var} \left[C_\ell^{21-gal}(y; z_i) \right] = \left(C_\ell^{21-gal}(y; z_i) \right)^2 + (C_{\ell,S}^{21}(y; z_i) + C_{\ell,N}^{21}(y; z_i)) \left(C_{\ell,S}^{gal} + C_{\ell,N}^{gal} \right). \tag{4.65}$$

We then compute our signal to noise estimates for the cross-correlation as

$$(SNR)^2 = \sum_\ell 2\ell\Delta\ell f_{sky} \frac{\left(C_\ell^{21-gal} \right)^2}{\text{var} \left[C_\ell^{21-gal} \right]}. \tag{4.66}$$

In Figure 4.20 we show the cross-correlation signal between the photometric galaxy survey and 21cm HIRAX survey and the cumulative SNR as a function of angular wavenumber. The cumulative SNR is obtained by summing the SNR at each mode in quadrature. We compute the cross-correlation in four 100 MHz bins in the HIRAX frequency range. We

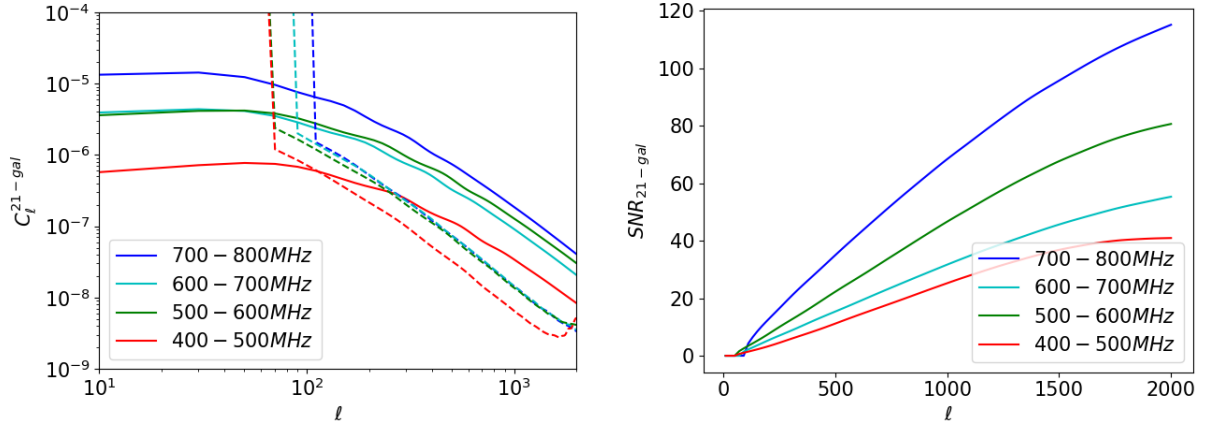


Figure 4.20: (a) The cross-correlation signal and noise for the HIRAX 21cm measurements in combination with the LSST photometric galaxy survey in the HIRAX frequency band binned in 100 MHz channels.(b) The cumulative SNR for the cross-correlation estimator in HIRAX frequency bins.

also show the cross-correlation variance (dashed lines). We see the cross variance term drops below the signal on scales of $\ell \approx 100$ leading to possible detection only above these modes. The cross-correlation SNR in each bin shows good statistical detection that can be used to obtain parameter constraints for the photometric galaxy bias and the HI model parameters. In the photometric case, going to finer bins can improve our overall SNR up to a certain threshold where our number density becomes too small. We will explore the possibility of parameter constraints from this cross-correlation signal in future work and show how finer binning can improve our results over the entire range. Another interesting application for this study is to use the cross-correlation to constrain the photometric redshifts of the galaxy survey. Since the redshift information in photometric surveys is not well constrained we can use HI surveys like HIRAX to help calibrate the photometric redshifts [50]. We will study photometric redshift calibration from HI surveys in future work in particular using the 21-21- δ_{gal} bispectrum to improve the redshift calibration by constraining the low k_{\parallel} 21cm modes lost in foreground removal.

Chapter 5

Conclusion

We have now entered the realm of precision cosmology with astronomical observations already placing stringent constraints on the cosmological parameters that describe the universe. Next generation experiments will survey even larger volumes of the universe than ever before and this provides an exciting prospect for improved precision on the cosmological model. In this thesis we examined the planned HIRAX experiment and performed forecasts on its ability to detect the cosmological 21cm signal and constrain the HI and cosmological parameters. We also investigated the cross-correlation prospects with other planned large scale structure surveys like CMB lensing and galaxy surveys.

In Chapter 2 we introduce the theoretical framework which describes the standard model of cosmology. We reviewed the solutions of a smooth homogenous universe then introduced the perturbations which we observe today in the form of large scale structure and CMB anisotropies. We then reviewed the observational probes used to measure the key features of the universe that are most relevant to this thesis.

In Chapter 3 we introduced the 21cm line emission and described the theoretical modelling of this signal. We showed that the HIRAX experiment will be able to make a strong statistical detection of this signal that can then be transformed into tight constraints on cosmological parameters. In this chapter we also investigated the HIRAX array layout op-

timisation. We showed how the layout strategy can affect our sensitivity and data volume of the experiment. By changing the array layout we can also examine the effect on signal extraction and foreground separation by a given layout design. Ideally, we would like to sample the uv space smoothly as a function of frequency which will allow us to efficiently remove the foreground contaminants but we also have to consider the data challenges and optimise for this. We have found that the standard compact grid layout is the best option in terms of redundancy and data volume. The standard grid also gives the best sensitivity at small scales for the BAO detection. We have also found however that by subdividing the standard grid into smaller grids or considering the extended grid which evenly spreads out the uv coverage we can smooth out the sensitivity as a function of frequency. For future work we plan to continue the investigation of the array layout optimisation. We look to turn the sensitivity as a function of frequency information into a signal recovery estimate. We plan to simulate a cosmological signal and foreground signal as a function of frequency and then for each array case see how well a given array layout can reconstruct both these signals along its sensitivity. We would be interested in identifying which cases can construct both these signals independently so that we can separate the foreground signal from the cosmological signal without leakage.

In Chapter 4 we studied what we can learn from cross-correlation surveys with HIRAX. Here we cross-correlated the 21cm signal with both the CMB lensing convergence and galaxy surveys. We found the CMB lensing two point cross-correlation signal is not detectable after foreground removal but we show that the three point bispectrum $B_{\ell}^{2121\kappa}$ can be detected with high signal to noise ratio in each of four HIRAX redshift bins. We have also shown how the bispectrum can be used in combination with the 21cm autocorrelation measurement to independently constrain parameters that are usually degenerate in large scale structure surveys. We have shown an independent constraint on the $f\Omega_{HI}$ and σ_8 parameter combination. We also used the bispectrum to improve our cosmological parameter constraints. Here we obtained a dark energy parameter figure of merit of 927, which is almost three times the 21cm autocorrelation case. We have also found that a 21cm-spectroscopic cross-correlation survey can be detected with high signal to noise in a given redshift bin and with this detection

we show how we can constrain the HI and galaxy parameters to below a percent level. We also showed that the 21cm-photometric galaxy cross-correlation is also promising in terms of its signal to noise ratio which can then be used to constrain parameters and the photometric redshift information. For future work we plan to turn the cross-correlation constraints obtained here into constraints on modified gravity theories and investigate non-Gaussianity parameters. We will also turn the promising 21cm-spectroscopic cross-correlation results into constraints on the cosmological parameters and cross-BAO forecasts. We also plan to use the 21cm-photometric cross-correlation to constrain the HI and photometric parameters as well as the cosmological parameters. For this case we also want to show how we can use the 21cm information to calibrate the photometric redshift information. For both the galaxy surveys we also plan to compute the bispectrum in a similar way to the CMB lensing convergence case to see how we may improve our parameter constraints.

Appendix A

Fisher Matrix Derivatives

A.1. The 21cm Signal Derivatives

Here we compute the Fisher matrix derivatives on the 21cm signal which can be written explicitly as

$$\begin{aligned}
 C_l^{2121}(y; z_i) &= \bar{T}^2 [b_{HI}^{(1)} + f\mu_k^2]^2 D^2 \frac{P_m(k, z=0)}{\chi_{\nu,i}^2} \\
 &= A_b^2 \Omega_{HI}^2 [b_{HI}^{(1)} + f\mu_k^2]^2 D^2 \frac{P_m(k, z=0)}{\chi_{\nu,i}^2} \left(\frac{\sigma_8}{\sigma_8^{fid}} \right)^2 \\
 &= A_b^2 [b_{HI}^{(1)} \Omega_{HI}^2 + f\Omega_{HI}^2 \mu_k^2]^2 D^2 \frac{P_m(k, z=0)}{\chi_{\nu,i}^2} \left(\frac{\sigma_8}{\sigma_8^{fid}} \right)^2
 \end{aligned} \tag{A.1}$$

where $A_b(z) = \frac{566h}{0.003} \frac{H_0}{H(z)} (1+z)^2 \mu K$ such that $\bar{T}(z) = A_b(z) \Omega_{HI}(z)$. We now differentiate the 21cm power spectrum with respect to each of the linearly independent parameters $\{A_{BAO}, \sigma_8, \Omega_{HI} b_{HI}, \Omega_{HI} f\}$ to get:

$$\frac{\partial C_l^{2121}(y; z_i)}{\partial A_{bao}} = \frac{f_{bao}}{1 + A_{bao} f_{bao}(k)} C_l^{2121}(y; z_i) \tag{A.2}$$

$$\frac{\partial C_l^{2121}(y; z_i)}{\partial \Omega_{HI} b_1} = \frac{2C_l^{2121}(y; z_i)}{b_{HI}^{(1)} + f\mu_k^2} \left(\frac{1}{\Omega_{HI}} \right) \tag{A.3}$$

$$\frac{\partial C_l^{2121}(y; z_i)}{\partial \Omega_{HI} f} = \frac{2\mu_k^2 C_l^{2121}(y; z_i)}{b_{HI}^{(1)} + f\mu_k^2} \left(\frac{1}{\Omega_{HI}} \right) \quad (\text{A.4})$$

$$\frac{\partial C_l^{2121}(y; z_i)}{\partial \sigma_8} = \frac{2C_l^{2121}(y; z_i)}{\sigma_8} \quad (\text{A.5})$$

For the derivative on the distance scale parameters we replace l, y with $\alpha_\perp \ell, \alpha_\parallel y$ and write the 21cm power spectrum as

$$C_{\ell, S}^{2121}(y; z_i) = T_b^2(z) \frac{\alpha_\perp^2 \alpha_\parallel}{\chi_{\parallel, i}^2 r_{\nu, i}} [b_{HI} + f\mu_{k_\alpha}^2]^2 D^2 P_m \left(\frac{\alpha_\perp \ell}{\chi_{\parallel, i}}, \frac{\alpha_\parallel y}{r_{\nu, i}}; z = 0 \right) \quad (\text{A.6})$$

where

$$\mu_{k_\alpha} = \frac{\alpha_\parallel \frac{y}{r_{\nu, i}}}{\sqrt{\alpha_\parallel^2 \left(\frac{y}{r_{\nu, i}} \right)^2 + \alpha_\perp^2 \left(\frac{\ell}{\chi_{\parallel, i}} \right)^2}}. \quad (\text{A.7})$$

We now calculate the derivatives as

$$\frac{\partial C_{\ell, S}^{2121}(y; z_i)}{\partial \alpha_\perp} = \left[\frac{2}{\alpha_\perp} + \frac{2f}{b_{HI} + f\mu_{k_\alpha}^2} \frac{\partial \mu_{k_\alpha}^2}{\partial \alpha_\perp} + \frac{\partial \log P(k_\alpha)}{\partial k} \frac{\partial k}{\partial \alpha_\perp} \right] C_{\ell, S}^{2121} \quad (\text{A.8})$$

and

$$\frac{\partial C_{\ell, S}^{2121}(y; z_i)}{\partial \alpha_\parallel} = \left[\frac{1}{\alpha_\parallel} + \frac{2f}{b_{HI} + f\mu_{k_\alpha}^2} \frac{\partial \mu_{k_\alpha}^2}{\partial \alpha_\parallel} + \frac{\partial \log P(k_\alpha)}{\partial k} \frac{\partial k}{\partial \alpha_\parallel} \right] C_{\ell, S}^{2121} \quad (\text{A.9})$$

where

$$\frac{\partial \mu_{k_\alpha}^2}{\partial \alpha_\perp} = \frac{-\alpha_\perp \left(\frac{\ell}{\chi_{\parallel, i}} \right) \mu_{k_\alpha}}{\alpha_\perp^2 \left(\frac{\ell}{\chi_{\parallel, i}} \right)^2 + \alpha_\parallel^2 \left(\frac{y}{r_{\nu, i}} \right)^2} \quad (\text{A.10})$$

and

$$\frac{\partial \mu_{k_\alpha}^2}{\partial \alpha_\parallel} = \left(\frac{1}{\alpha_\parallel} - \frac{1}{\sqrt{\alpha_\parallel^2 \left(\frac{y}{r_{\nu, i}} \right)^2 + \alpha_\perp^2 \left(\frac{\ell}{\chi_{\parallel, i}} \right)^2}} \right) \mu_{k_\alpha}. \quad (\text{A.11})$$

A.2. The Bispectrum Derivatives

The bispectrum expression is given by

$$B_l^{2121\kappa}(y; z_i) = \left[\frac{V_{L,j}}{V_p} \right] \left[\frac{W_\kappa(\chi_\parallel) D^4(\chi_\parallel)}{\chi_\parallel^2} \right] P_{21}(k, z_i = 0) \times \int \frac{d^3q}{(2\pi)^3} W_{L,\kappa}(\mathbf{q}) W_{L,21}(\mathbf{q}) P_m(\mathbf{q}, z = 0) \left\{ \frac{b_{HI}^{(2)} + 2(2\mu_k^2 - 1)f(1 + f\mu_k^2)}{b_{HI}^{(1)} + f\mu_k^2} + \frac{1}{2}(1 + f\mu_k^2) \left(3 - \frac{d \log P_m}{d \log k} \right) \right\}. \quad (\text{A.12})$$

we differentiate the bispectrum with respect to the linearly independent parameters $[A_{bao}, \sigma_8, \Omega_{HI} b_1, \Omega_{HI} f, b_2, \alpha_\parallel, \alpha_\perp]$ to get

$$\frac{\partial B_l^{2121\kappa}(y; z_i)}{\partial \sigma_{A_{bao}}} = B_l^{2121\kappa} \left[\frac{f_{bao}}{1 + A_{bao} f_{bao}} + \frac{\int \frac{d^3q}{(2\pi)^3} W_{L,\kappa}(\mathbf{q}) W_{L,21}(\mathbf{q}) \frac{\partial P_m(\mathbf{q}, z=0)}{\partial A_{bao}}}{\int \frac{d^3q}{(2\pi)^3} W_{L,\kappa}(\mathbf{q}) W_{L,21}(\mathbf{q}) P_m(\mathbf{q}, z = 0)} - \frac{1}{2} (1 + f\mu_k^2) \frac{\partial}{\partial A_{bao}} \left(\frac{d \log P_m}{d \log k} \right) \right] \quad (\text{A.13})$$

$$\frac{\partial B_l^{2121\kappa}(y; z_i)}{\partial \sigma_8} = \frac{4 B_l^{2121\kappa}(y; z_i)}{\sigma_8} \quad (\text{A.14})$$

$$\begin{aligned} \frac{\partial B_l^{2121\kappa}(y; z_i)}{\partial b_1 \Omega_{HI}} &= \frac{B_l^{2121\kappa}(y; z_i)}{\left[\frac{b_{HI}^{(2)} + 2f(2\mu_k^2 - 1)(1 + f\mu_k^2)}{b_{HI}^{(1)} + f\mu_k^2} + \frac{1}{2} \left(3 - \frac{d \log P_m}{d \log k} \right) \right]} \\ &\times \frac{2 \left[\frac{b_{HI}^{(2)} + 2f(2\mu_k^2 - 1)(1 + f\mu_k^2)}{b_{HI}^{(1)} + f\mu_k^2} + \frac{1}{2} \left(3 - \frac{d \log P_m}{d \log k} \right) \right]}{(b_{HI}^{(1)} + f\mu_k^2)} \\ &- \frac{b_{HI}^{(2)} + 2f(2\mu_k^2 - 1)(1 + f\mu_k^2)}{(b_{HI}^{(1)} + f\mu_k^2)^2} \times \left(\frac{1}{\Omega_{HI}} \right) \end{aligned} \quad (\text{A.15})$$

$$\frac{\partial B_l^{2121\kappa}(y; z_i)}{\partial b_2} = \frac{B_l^{2121\kappa}(y; z_i)}{\left[\frac{b_{HI}^{(2)} + 2f(2\mu_k^2 - 1)(1 + f\mu_k^2)}{b_{HI}^{(1)} + f\mu_k^2} + \frac{1}{2}(1 + f\mu_k^2) \left(3 - \frac{d \log P_m}{d \log k} \right) \right]} \times (b_{HI}^{(1)} + f\mu_k^2) \quad (\text{A.16})$$

$$\begin{aligned}
\frac{\partial B_\ell^{2121\kappa}(y; z_i)}{\partial f \Omega_{HI}} &= B_\ell^{2121\kappa}(y; z_i) \times \left\{ \frac{2\mu_k^2}{(b_{HI}^{(1)} + f\mu_k^2)} \right. \\
&+ \left(\frac{[2(2\mu_k^2 - 1)(1 + 2f\mu_k^2)] (b_{HI}^{(1)} + f\mu_k^2) - \mu_k^2 [b_{HI}^{(2)} + 2(2\mu_k^2 - 1)(1 + f\mu_k^2)f]}{(b_{HI}^{(1)} + f\mu_k^2)^2 \times \left[\frac{b_{HI}^{(2)} + 2(2\mu_k^2 - 1)(1 + f\mu_k^2)f}{b_{HI}^{(1)} + f\mu_k^2} + \frac{1}{2}(1 + f\mu_k^2) \left(3 - \frac{d \log P_m}{d \log k} \right) \right]} \right) \\
&\left. - \frac{\mu_k^2 \left(3 - \frac{d \log P_m}{d \log k} \right)}{2 \left[\frac{b_{HI}^{(2)} + 2(2\mu_k^2 - 1)(1 + f\mu_k^2)f}{b_{HI}^{(1)} + f\mu_k^2} + \frac{1}{2}(1 + f\mu_k^2) \left(3 - \frac{d \log P_m}{d \log k} \right) \right]} \right\} \times \left(\frac{1}{\Omega_{HI}} \right). \tag{A.17}
\end{aligned}$$

The derivatives for both distance scale parameters are

$$\begin{aligned}
\frac{\partial B_\ell^{\kappa 2121}}{\partial \alpha} &= B_\ell^{\kappa 2121} \left[\frac{n_\alpha}{\alpha} + \frac{\partial \log P_{21}(\mathbf{k})}{\partial \alpha} + \frac{\int \frac{d^3 q}{(2\pi)^3} \frac{\partial}{\partial q} (W_{L,\kappa}(\vec{q}) + W_{L,21}(\vec{q}) + P_m(\mathbf{q}; z=0)) \frac{\partial q}{\partial \alpha}}{\int \frac{d^3 q}{(2\pi)^3} W_{L,\kappa}(\mathbf{q}) W_{L,21}(\mathbf{q}) P_m(\mathbf{q}; z=0)} \right] + \\
&\left[\frac{[4f(1 + f\mu_k^2) + 2f^2\mu_k(2\mu_k^2 - 1)] (b + f\mu_k^2) - 2f(b_{HI}^{(2)} + (2\mu_k^2 - 1)(1 + f\mu_k^2)f)}{(b + f\mu_k^2)^2 \times \left[\frac{b_{HI}^{(2)} + 2(2\mu_k^2 - 1)(1 + f\mu_k^2)f}{b_{HI}^{(1)} + f\mu_k^2} + \frac{1}{2}(1 + f\mu_k^2) \left(3 - \frac{d \log P_m}{d \log k} \right) \right]} \frac{\partial \mu_k^2}{\partial \alpha} \right. \\
&\left. + \frac{\frac{1}{2}f \left(3 - \frac{d \log P_m}{d \log k} \right) \partial_\alpha \mu_k^2 - \frac{1}{2}(1 + f\mu_k^2) \frac{d}{dk} \left(\frac{d \log P_m}{d \log k} \right) \partial_\alpha k}{\left\{ \frac{b_{HI}^{(2)} + 2(2\mu_k^2 - 1)(1 + f\mu_k^2)f}{b_{HI}^{(1)} + f\mu_k^2} \right\}} \right] B_\ell^{\kappa 2121} \tag{A.18}
\end{aligned}$$

where $n_{\alpha_\parallel} = 1$, $n_{\alpha_\perp} = 4$ and

$$\begin{aligned}
\frac{d}{dk} \left(\frac{d \log P_m}{d \log k} \right) &= \frac{d}{dk} \left(\frac{k}{P_m} \frac{d P_m}{dk} \right) \\
&= \left(\frac{d^2 P_m}{d^2 k} \right) \frac{k}{P_m} + \left(\frac{P_m - \frac{d P_m}{dk} k}{P_m^2} \right) \frac{d P_m}{dk} \tag{A.19}
\end{aligned}$$

A.3. The Convergence Field Derivatives

For the CMB lensing convergence signal we only consider forecasts on $\{A_{bao}, \sigma_8, \alpha_{\parallel}, \alpha_{\perp}\}$.

The derivatives are given as

$$\frac{C_{\ell}^{\kappa\kappa}}{\partial A_{bao}} = \frac{f_{bao}}{1 + A_{bao}f_{bao}} C_{\ell}^{\kappa\kappa} \quad (\text{A.20})$$

$$\frac{C_{\ell}^{\kappa\kappa}}{\partial \sigma_8} = \frac{2}{\sigma_8} C_{\ell}^{\kappa\kappa} \quad (\text{A.21})$$

$$\partial C_{\ell}^{\kappa\kappa} \partial \alpha_{\parallel} = \left[\frac{\partial \log P(k)}{\partial k} \frac{\partial k}{\partial \alpha_{\parallel}} \right] C_{\ell}^{\kappa\kappa} \quad (\text{A.22})$$

and

$$\partial_{\alpha_{\perp} k} C_{\ell}^{\kappa\kappa} = \left[\frac{2}{\alpha_{\perp}} + \frac{\partial \log P(k)}{\partial k} \frac{\partial k}{\partial \alpha_{\perp}} \right] C_{\ell}^{\kappa\kappa}. \quad (\text{A.23})$$

A.4. Transformation Matrix Derivatives

Here we show the derivatives that go into the transformation matrix that converts the redshift function and distance scale parameters into cosmological parameter constraints.

We start with the derivatives of linear growth rate function f , which are

$$\frac{\partial f}{\partial \Omega_k} = -\gamma f \left[\Omega_M^{-1}(a) - \frac{\partial \log E(a)}{\partial \Omega_k} \right] \quad (\text{A.24})$$

$$\frac{\partial f}{\partial \Omega_{\Lambda}} = -\gamma f \left[\Omega_M^{-1}(a) - \frac{\partial_{\Omega_{\Lambda}} E(a)}{E(a)} \right] \quad (\text{A.25})$$

$$\frac{\partial f}{\partial w_0} = -\frac{3}{2} \gamma f \frac{\Omega_{\Lambda}(a)}{E(a)} \ln(a) \quad (\text{A.26})$$

$$\frac{\partial f}{\partial w_a} = -\frac{3}{2} \gamma f \frac{\Omega_{\Lambda}(a)}{E(a)} [(1 + \ln(a)) - a] \quad (\text{A.27})$$

$$\frac{\partial f}{\partial \gamma} = \frac{\gamma f}{\Omega_M(a)} \quad (\text{A.28})$$

$$\frac{\partial f}{\partial h} = 0 \quad (\text{A.29})$$

For α_{\parallel} the derivatives are

$$\frac{\partial \alpha_{\parallel}}{\partial \beta} = \frac{\partial E(a)}{\partial \beta} \frac{1}{E^{fid}(a)} \quad (\text{A.30})$$

for all parameters except h for which the derivative is given by

$$\frac{\partial \alpha_{\parallel}}{\partial h} = \frac{\alpha_{\parallel}}{h}. \quad (\text{A.31})$$

For the α_{\perp} the derivatives are

$$\frac{\partial \alpha_{\perp}}{\partial \beta} = \frac{\alpha_{\perp}}{\chi_{\parallel,i}^{fid}} \int \frac{cda}{a^2 E^2(a)} \frac{\partial E(a)}{\partial \beta} \quad (\text{A.32})$$

for all cosmological parameters. The derivatives of $E(a)$ are

$$\frac{\partial E(a)}{\partial \Omega_k} = \frac{(a^{-2} - a^{-3})}{2E(a)} \quad (\text{A.33})$$

$$\frac{\partial E(a)}{\partial \Omega_{\Lambda}} = \frac{1 - a^{-3}}{2E(a)} \quad (\text{A.34})$$

$$\frac{\partial E(a)}{\partial w_0} = \frac{-3 \Omega_{\Lambda}(a)}{2 E(a)} \ln(a) \quad (\text{A.35})$$

$$\frac{\partial E(a)}{\partial w_a} = \frac{-3 \Omega_{\Lambda}(a)}{2 E(a)} (1 + \ln(a) - a) \quad (\text{A.36})$$

$$\frac{\partial f}{\partial \gamma} = \frac{\partial f}{\partial h} = 0. \quad (\text{A.37})$$

Appendix B

The Bispectrum Derivation

B.1. The Squeezed Limit Bispectrum

Here we show the expansion of the bispectrum in Equation 4.30 under the squeezed triangle approximation. The bispectrum expression is

$$\begin{aligned}
 B_{\ell}^{\bar{\kappa}\delta T_{21}\delta T_{21}} &= \left[\frac{V_{L,j}}{V_p(\chi_{\parallel})} \right]^2 [W_{\kappa}(\chi_{\parallel}) D^4(\chi_{\parallel}) \chi_{\parallel,i}] \times \int \frac{d^3 q}{(2\pi)^3} W_{L,\kappa}(\mathbf{q}) P_m(\mathbf{q}; z=0) \\
 &\times \int \frac{d^3 k_1}{(2\pi)^3} W_{L,21}(\mathbf{k}_1) W_{L,21}^*(\mathbf{k}_1 + \mathbf{q}) \\
 &\left\{ P_{21}(\mathbf{k}', z=0) \frac{Z_{HI}^{(2)}(\mathbf{q}, \mathbf{k}')}{Z_{HI}^{(1)}(\mathbf{k}')} + P_{21}(\mathbf{k} - \mathbf{k}_1, z=0) \frac{Z_{HI}^{(2)}(-\mathbf{q}, \mathbf{k} - \mathbf{k}_1)}{Z_{HI}^{(1)}(\mathbf{k} - \mathbf{k}_1)} \right\}
 \end{aligned} \tag{B.1}$$

where we have set $\mathbf{k}' = \mathbf{k} - \mathbf{k}_1 - \mathbf{q}$. The expectation value of the other combinations vanishes in the squeezed triangle limit due to them being short mode-long mode combinations. Also note that $\int \frac{d^3 k_1}{(2\pi)^3} W_{L,21}(\mathbf{k}_1) W_{L,21}^*(\mathbf{k}_1 + \mathbf{q}) = W_{L,21}(\mathbf{q})/V_{L,j}$. Now if the wavenumber \mathbf{k} is much larger than \mathbf{q} and \mathbf{k}_1 , which is the case, then we can use the squeezed triangle approximation for the term in curly brackets. We start by setting

$$\mathbf{k}' = \mathbf{k} - \mathbf{k}_1 - \mathbf{q} = \mathbf{k}(1 - \epsilon_1 - \epsilon_2) \tag{B.2}$$

where $\mathbf{k}_1 = \epsilon_1 \mathbf{k}$ and $\mathbf{q}_1 = \epsilon_2 \mathbf{k}$. This also gives $\mathbf{k} - \mathbf{k}_1 = \mathbf{k}(1 - \epsilon_1)$. We now expand about ϵ_1 and ϵ_2 up to leading order. The expansion of each term is given as follows

Firstly we expand the 21cm power spectra,

$$\begin{aligned} P_{21}(\mathbf{k} - \mathbf{k}_1 - \mathbf{q}) &= P_{21}(\mathbf{k}(1 - \epsilon_1 - \epsilon_2)) \\ &= P_{21}(\mathbf{k}) \left(1 - (\epsilon_1 + \epsilon_2) \frac{\partial \ln P_{21}(\mathbf{k})}{\partial \ln k} \right) \end{aligned} \quad (\text{B.3})$$

and

$$\begin{aligned} P_{21}(\mathbf{k} - \mathbf{k}_1) &= P_{21}(\mathbf{k}(1 - \epsilon_1)) \\ &= P_{21}(\mathbf{k}) \left(1 - \epsilon_1 \frac{\partial \ln P_{21}(\mathbf{k})}{\partial \ln k} \right). \end{aligned} \quad (\text{B.4})$$

Now we expand the first order redshift distortion functions

$$\begin{aligned} Z_{HI}^{(1)}(\mathbf{k}', \chi_{\parallel}) &= b_{HI}(\chi_{\parallel}) + f(\chi_{\parallel}) \left(\frac{k_{\parallel}}{k} \right)^2 \\ &= b_{HI}(\chi_{\parallel}) + f(\chi_{\parallel}) \left(\frac{k_{\parallel}(1 - \epsilon_1 - \epsilon_2)}{k(1 - \epsilon_1 - \epsilon_2)} \right)^2 \\ &= b_{HI}(\chi_{\parallel}) + f(\chi_{\parallel}) \mu_k^2 \\ &= Z_{HI}^{(1)}(\mathbf{k}, \chi_{\parallel}). \end{aligned} \quad (\text{B.5})$$

and

$$\begin{aligned} Z_{HI}^{(1)}(\mathbf{k} - \mathbf{k}_1, \chi_{\parallel}) &= b_{HI}(\chi_{\parallel}) + f(\chi_{\parallel}) \left(\frac{k_{\parallel}}{k} \right)^2 \\ &= b_{HI}(\chi_{\parallel}) + f(\chi_{\parallel}) \left(\frac{k_{\parallel}(1 - \epsilon_1)}{k(1 - \epsilon_1)} \right)^2 \\ &= b_{HI}(\chi_{\parallel}) + f(\chi_{\parallel}) \mu_k^2 \\ &= Z_{HI}^{(1)}(\mathbf{k}, \chi_{\parallel}). \end{aligned} \quad (\text{B.6})$$

Now for the second order functions $Z_{HI}^{(2)}(\mathbf{k}_1, \mathbf{k}_2, \chi_{\parallel})$ we get

$$\begin{aligned}
Z_{HI}^{(2)}(\mathbf{q}, \mathbf{k} - \mathbf{k}_1 - \mathbf{q}, \chi_{\parallel}) &= Z_{HI}^{(2)}(\epsilon_2 \mathbf{k}, \mathbf{k}(1 - \epsilon_1 - \epsilon_2), \chi_{\parallel}) \\
&= 1/2 b_{HI}^{(2)}(\chi_{\parallel}) + b_{HI}^{(1)}(\chi_{\parallel}) F_2(\epsilon_2 \mathbf{k}, \mathbf{k}(1 - \epsilon_1 - \epsilon_2)) + f(\chi_{\parallel}) \left(\frac{k_{\parallel}}{k} \right)^2 G_2(\epsilon_2 \mathbf{k}, \mathbf{k}(1 - \epsilon_1 - \epsilon_2)) \\
&+ 1/2 f(\chi_{\parallel}) k_{\parallel} (1 - \epsilon) \times \\
&\quad \left[\frac{\mu_k}{\epsilon_2 k} \left(b_{HI}^{(1)}(\chi_{\parallel}) + f(\chi_{\parallel}) \left(\frac{k_{\parallel}}{k} \right)^2 \right) + \frac{\mu_k}{k(1 - \epsilon_1 - \epsilon_2)} \left(b_{HI}^{(1)}(\chi_{\parallel}) + f(\chi_{\parallel}) \left(\frac{k_{\parallel}}{k} \right)^2 \right) \right] \\
&= 1/2 b_{HI}^{(2)}(\chi_{\parallel}) + \left(b_{HI}^{(1)}(\chi_{\parallel}) + f(\chi_{\parallel}) \mu_k^2 \right) \times \\
&\quad \left[F_2(\epsilon_2 \mathbf{k}, \mathbf{k}(1 - \epsilon_1 - \epsilon_2)) + 1/2 f(\chi_{\parallel}) \mu_k^2 \left(\frac{1 - \epsilon_1}{\epsilon_2} + \frac{1 - \epsilon_1}{1 - \epsilon_1 - \epsilon_2} \right) \right].
\end{aligned} \tag{B.7}$$

The kernel functions are expanded as follows

$$\begin{aligned}
F_2(\epsilon_2 \mathbf{k}, \mathbf{k}(1 - \epsilon_1 - \epsilon_2)) &= G_2(\epsilon_2 \mathbf{k}, \mathbf{k}(1 - \epsilon_1 - \epsilon_2)) \\
&= \frac{5}{7} + \frac{2}{7} \left(\frac{\epsilon_2(1 - \epsilon_1 - \epsilon_2) \mathbf{k} \cdot \mathbf{k}}{k^2 \epsilon_2 (1 - \epsilon_1 - \epsilon_2)} \right)^2 + \frac{1}{2} \left(\frac{\epsilon_2(1 - \epsilon_1 - \epsilon_2) \mathbf{k} \cdot \mathbf{k}}{k^2 \epsilon_2 (1 - \epsilon_1 - \epsilon_2)} \right) \left[\frac{\epsilon_2}{1 - \epsilon_1 - \epsilon_2} + \frac{1 - \epsilon_1 - \epsilon_2}{\epsilon_2} \right] \\
&\approx \frac{5}{7} + \frac{2}{7}(1) + \frac{1}{2}(1) \left[\epsilon_2(1 + \epsilon_1 + \epsilon_2) + \frac{1}{\epsilon_2}(1 - \epsilon_1) - 1 \right] \\
&= 1 + \frac{1}{2} \left[\epsilon_2 + \frac{1}{\epsilon_2}(1 - \epsilon_1) - 1 \right] + \mathcal{O}(\epsilon_1^2, \epsilon_2^2, \epsilon_1 \epsilon_2) \\
&= \frac{1}{2} \left(1 + \epsilon_2 + \frac{1}{\epsilon_2}(1 - \epsilon_1) \right)
\end{aligned} \tag{B.8}$$

and where

$$\begin{aligned}
\frac{1 - \epsilon_1}{\epsilon_2} + \frac{1 - \epsilon_1}{1 - \epsilon_1 - \epsilon_2} &\approx \frac{1}{\epsilon_2}(1 - \epsilon_1) + (1 - \epsilon_1)(1 + \epsilon_1 + \epsilon_2) \\
&= \epsilon_2(1 - \epsilon_1) + 1 + \epsilon_1 + \epsilon_2 - \epsilon_1 - \epsilon_1^2 - \epsilon_2 \epsilon_1 \\
&= \epsilon_2 + \frac{1}{\epsilon_2}(1 - \epsilon_1) + 1 + \mathcal{O}(\epsilon_1^2, \epsilon_2 \epsilon_1).
\end{aligned} \tag{B.9}$$

Then $Z_{HI}^{(2)}(\mathbf{q}, \mathbf{k} - \mathbf{k}_1 - \mathbf{q}, \chi_{\parallel})$ becomes

$$\begin{aligned} Z_{HI}^{(2)}(\mathbf{q}, \mathbf{k} - \mathbf{k}_1 - \mathbf{q}, \chi_{\parallel}) &= Z_{HI}^{(2)}(\epsilon_2 \mathbf{k}, \mathbf{k}(1 - \epsilon_1 - \epsilon_2), \chi_{\parallel}) \\ &= 1/2 b_{HI}^{(2)}(\chi_{\parallel}) + \left(b_{HI}^{(1)}(\chi_{\parallel}) + f(\chi_{\parallel}) \mu_k^2 \right) \left(1 + 1/2 f(\chi_{\parallel}) \mu_k^2 \right) \left(\epsilon_2 + \frac{1}{\epsilon_2} (1 - \epsilon_1) + 1 \right) \end{aligned} \quad (\text{B.10})$$

and

$$\begin{aligned} Z_{HI}^{(2)}(-\mathbf{q}, \mathbf{k} - \mathbf{k}_1, \chi_{\parallel}) &= Z_{HI}^{(2)}(-\epsilon_2 \mathbf{k}, \mathbf{k}(1 - \epsilon_1), \chi_{\parallel}) \\ &= 1/2 b_{HI}^{(2)}(\chi_{\parallel}) + b_{HI}^{(1)}(\chi_{\parallel}) F_2(-\epsilon_2 \mathbf{k}, \mathbf{k}(1 - \epsilon_1)) + f(\chi_{\parallel}) \mu_k^2 G_2(-\epsilon_2 \mathbf{k}, \mathbf{k}(1 - \epsilon_1)) + \\ & f(\chi_{\parallel}) \mu_k^2 (1 - \epsilon_1 - \epsilon_2) \left(\frac{-1}{\epsilon_2} + \frac{1}{1 - \epsilon_1} \right) (b(\chi_{\parallel}) + f(\chi_{\parallel}) \mu_k^2) \\ &= 1/2 b_{HI}^{(2)}(\chi_{\parallel}) + (b(\chi_{\parallel}) + f(\chi_{\parallel}) \mu_k^2) \times \\ & \quad \left(F_2(-\epsilon_2 \mathbf{k}, \mathbf{k}(1 - \epsilon_1)) + \frac{1}{2} f \mu_k^2 \left(\frac{-1 + \epsilon_1 + \epsilon_2}{\epsilon_2} + \frac{1 - \epsilon_1 - \epsilon_2}{1 - \epsilon_1} \right) \right) \end{aligned} \quad (\text{B.11})$$

where $\mu_{-q} = \left(\frac{-\epsilon_2 \mathbf{k}_{\parallel}}{\epsilon_2 k} \right) = -\mu_k$. We now compute the response function

$$\begin{aligned} F_2(-\epsilon_2 \mathbf{k}, \mathbf{k}(1 - \epsilon_1)) &= G_2(-\epsilon_2 \mathbf{k}, \mathbf{k}(1 - \epsilon_1)) = \frac{5}{7} + \frac{2}{7}(1) + \frac{1}{2}(-1) \left[\frac{\epsilon_2}{1 - \epsilon_1} + \frac{1 - \epsilon_1}{\epsilon_2} \right] \\ &\approx 1 - \frac{1}{2} \left[\epsilon_1(1 + \epsilon_1) + \frac{1}{\epsilon_2}(1 - \epsilon_1) \right] \\ &= \frac{1}{2} \left[2 - \epsilon_2 - \frac{1}{\epsilon_2}(1 - \epsilon_1) \right] + \mathcal{O}(\epsilon_1 \epsilon_2) \end{aligned} \quad (\text{B.12})$$

and where

$$\begin{aligned} \frac{1 - \epsilon_1 - \epsilon_2}{-\epsilon_2} + \frac{1 - \epsilon_1 - \epsilon_2}{1 - \epsilon_1} &\approx -\frac{1}{\epsilon_2}(1 - \epsilon_1) + 1 + 1 - \epsilon_2(1 + \epsilon_1) \\ &= 2 - \frac{1}{\epsilon_2}(1 - \epsilon_1) - \epsilon_2 + \mathcal{O}(\epsilon_1 \epsilon_2) \end{aligned} \quad (\text{B.13})$$

which gives us

$$\begin{aligned} Z_{HI}^{(2)}(-\mathbf{q}, \mathbf{k} - \mathbf{k}_1, \chi_{\parallel}) &= Z_{HI}^{(2)}(-\epsilon_2 \mathbf{k}, \mathbf{k}(1 - \epsilon_1), \chi_{\parallel}) \\ &= 1/2 b_{HI}^{(2)}(\chi_{\parallel}) + \frac{1}{2} (b(\chi_{\parallel}) + f(\chi_{\parallel}) \mu_k^2) (1 + f(\chi_{\parallel}) \mu_k^2) \left(2 - \epsilon_2 - \frac{1}{\epsilon_2}(1 - \epsilon_1) \right) \end{aligned} \quad (\text{B.14})$$

Now we can expand the curly brackets in B.1

$$P_{21}(\mathbf{k}', z=0) \frac{Z_{HI}^{(2)}(\mathbf{q}, \mathbf{k}')}{Z_{HI}^{(1)}(\mathbf{k}')} + P_{21}(\mathbf{k} - \mathbf{k}_1, z=0) \frac{Z_{HI}^{(2)}(-\mathbf{q}, \mathbf{k} - \mathbf{k}_1)}{Z_{HI}^{(1)}(\mathbf{k} - \mathbf{k}_1)} \quad (\text{B.15})$$

which becomes

$$\frac{P_{21}(\mathbf{k})}{(b(\chi_{\parallel}) + f(\chi_{\parallel})\mu_k^2)} \times \mathcal{B} \quad (\text{B.16})$$

where we have defined

$$\begin{aligned} \mathcal{B} = & \left[1/2b_{HI}^{(2)}(\chi_{\parallel}) + \frac{1}{2} \left(b_{HI}^{(1)}(\chi_{\parallel}) + f(\chi_{\parallel})\mu_k^2 \right) (1 + f(\chi_{\parallel})\mu_k^2) \left(\epsilon_2 + \frac{1}{\epsilon_2}(1 - \epsilon_1) + 1 \right) \right] \\ & \left[1 - (\epsilon_1 + \epsilon_2) \frac{\partial \ln P_{21}(\mathbf{k})}{\partial \ln k} \right] \\ & + \left[1/2b_{HI}^{(2)}(\chi_{\parallel}) + \frac{1}{2} \left(b_{HI}^{(1)}(\chi_{\parallel}) + f(\chi_{\parallel})\mu_k^2 \right) (1 + f(\chi_{\parallel})\mu_k^2) \left(2 - \epsilon_2 - \frac{1}{\epsilon_2}(1 - \epsilon_1) \right) \right] \\ & \left[1 - \epsilon_1 \frac{\partial \ln P_{21}(\mathbf{k})}{\partial \ln k} \right]. \end{aligned} \quad (\text{B.17})$$

We now simplify these terms and note that the divergence terms cancel and we get

$$\begin{aligned} & = P_{21}(\mathbf{k}) \left\{ \frac{b_{HI}^{(2)}(\chi_{\parallel})}{(b(\chi_{\parallel}) + f(\chi_{\parallel})\mu_k^2)} + \frac{3}{2}(1 + f(\chi_{\parallel})\mu_k^2) - \frac{1}{2}(1 + f(\chi_{\parallel})\mu_k^2) \frac{\partial \ln P_{21}(k)}{\partial \ln k} + \mathcal{O}(\epsilon_1, \epsilon_2) \right\} \\ & = P_{21}(\mathbf{k}) \left\{ \frac{b_{HI}^{(2)}(\chi_{\parallel})}{(b(\chi_{\parallel}) + f(\chi_{\parallel})\mu_k^2)} + \frac{1}{2}(1 + f(\chi_{\parallel})\mu_k^2) \left[3 - \frac{\partial \ln P_{21}(k)}{\partial \ln k} \right] \right\} \\ & = P_{21}(\mathbf{k}) \left\{ \frac{b_{HI}^{(2)}(\chi_{\parallel}) + 2(2\mu_k^2 - 1)f(1 + f\mu_k^2)}{(b(\chi_{\parallel}) + f(\chi_{\parallel})\mu_k^2)} + \frac{1}{2}(1 + f(\chi_{\parallel})\mu_k^2) \left[3 - \frac{\partial \ln P_m(k)}{\partial \ln k} \right] \right\}. \end{aligned} \quad (\text{B.18})$$

B.2. The 21cm Autocorrelation and Bispectrum Covariance

Here we calculate the covariance between the three probes from the 21cm - CMB lensing convergence cross-correlation. In general the 21cm autocorrelation, bispectrum and the CMB convergence autocorrelation probes may not be strictly independent. The bispectrum in particular would measure the same 21cm and κ convergence modes as the respective autocorrelations. This means that simply adding the matrices as though they were independent may not be correct. In general, the Fisher matrix in terms of the likelihood function is defined as

$$F_{ij}(\ell, y) = \partial_i C(\ell, y)^T \text{cov}^{-1} \partial_j C(\ell, y) \quad (\text{B.19})$$

where for our case

$$C = \begin{pmatrix} C_\ell^{2121} \\ B_\ell^{2121-\kappa} \\ C_\ell^{\kappa\kappa} \end{pmatrix}. \quad (\text{B.20})$$

We now adopt the notation $P = C_\ell^{2121}$, $B = B_\ell^{2121-\kappa}$, $\kappa = C_\ell^{\kappa\kappa}$ for convenience in the following computation. The covariance matrix is given by

$$\text{Cov} = \begin{pmatrix} \hat{C}_{PP} & \hat{C}_{PB} & \hat{C}_{\kappa P} \\ \hat{C}_{PB} & \hat{C}_{BB} & \hat{C}_{B\kappa} \\ \hat{C}_{\kappa P} & \hat{C}_{B\kappa} & \hat{C}_{\kappa\kappa} \end{pmatrix}. \quad (\text{B.21})$$

where

$$\begin{aligned}
\hat{C}_{PP} &= C_{\ell,S}^{2121} + C_{\ell,N}^{2121} \\
\hat{C}_{BB} &= \text{var}[B_{\ell,sky}^{2121\kappa}] \\
\hat{C}_{\kappa\kappa} &= C_{\ell,S}^{\kappa\kappa} + C_{\ell,N}^{\kappa\kappa} \\
\hat{C}_{P\kappa} &= (C_{\ell,S}^{2121} + C_{\ell,N}^{2121})(C_{\ell,S}^{\kappa\kappa} + C_{\ell,N}^{\kappa\kappa}) \\
\hat{C}_{B\kappa} &= 3\text{var}[B_{\ell,sky}^{2121\kappa}](C_{\ell,S}^{\kappa\kappa} + C_{\ell,N}^{\kappa\kappa}) \\
\hat{C}_{PB} &= 6\text{var}[B_{\ell,sky}^{2121\kappa}](C_{\ell,S}^{2121} + C_{\ell,N}^{2121}).
\end{aligned} \tag{B.22}$$

This gives us our full Fisher matrix as

$$\begin{aligned}
F_{ij}(\ell, y) &= (1/\det[\text{cov}]) \times \\
& [[\partial_{ij}^2 P^2]D_{11} - 2[\partial_i P][\partial_j B]D_{12} + 2[\partial_i P][\partial_j \kappa]D_{13} + [\partial_{ij}^2 B^2]D_{22} - 2[\partial_i B][\partial_j \kappa]D_{32} + [\partial_{ij}^2 \kappa^2]D_{33}]
\end{aligned} \tag{B.23}$$

where $\det[\text{cov}] = \hat{C}_{PP}D_{11} - \hat{C}_{PB}D_{12} + \hat{C}_{P\kappa}D_{13}$ and

$$\begin{aligned}
D_{11} &= \hat{C}_{BB}\hat{C}_{\kappa\kappa} - \hat{C}_{B\kappa}^2 \\
D_{12} &= \hat{C}_{PB}\hat{C}_{\kappa\kappa} - \hat{C}_{B\kappa}\hat{C}_{P\kappa} = D_{21} \\
D_{13} &= \hat{C}_{PB}\hat{C}_{P\kappa} - \hat{C}_{BB}\hat{C}_{P\kappa} = D_{31} \\
D_{22} &= \hat{C}_{PP}\hat{C}_{\kappa\kappa} - \hat{C}_{P\kappa}^2 \\
D_{23} &= \hat{C}_{PP}\hat{C}_{B\kappa} - \hat{C}_{P\kappa}\hat{C}_{PB} = D_{32} \\
D_{33} &= \hat{C}_{PP}\hat{C}_{BB} - \hat{C}_{PB}^2
\end{aligned} \tag{B.24}$$

In Figure B.1 we show the effect of adding in the covariance terms to our Fisher forecasts. Our analysis suggests the covariance is negligible and we can treat the 21cm autocorrelation, bispectrum and convergence field autocorrelation as independent. The reason for this is due to the convergence field which is integrated over the line of sight whereas the 21cm modes oscillate over this range which leaves no covariance or dependence between how they combine in the bispectrum.

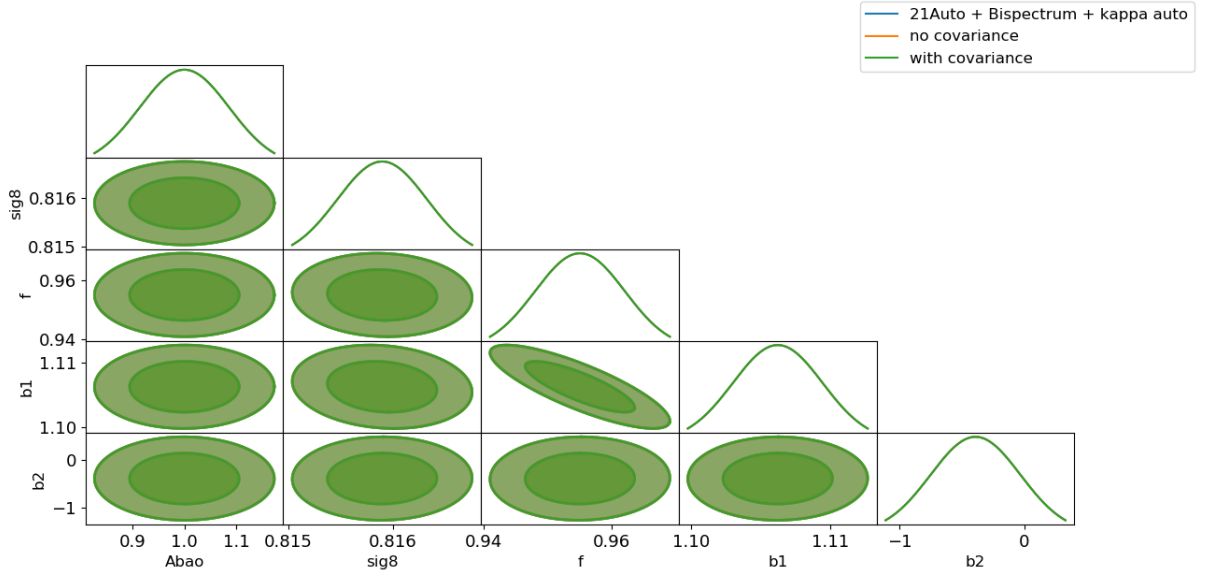


Figure B.1: Forecast constraints on the HI model parameters first for independently adding the 21cm autocorrelation, the bispectrum and the convergence autocorrelation versus the full covariance calculation with and without the covariance terms. We see that the covariance terms appear to be negligible in this study. For the purpose of this comparison we have fixed Ω_{HI} .

This gives us

$$\begin{aligned} \text{var} [B_{\ell, \text{sky}}^{\bar{\kappa} \delta T_{21} \delta T_{21}}(y; z_i)] &= 3 \text{var}[\delta T_{21}(\ell, y; z_i)]^2 \times \text{var}[\bar{\kappa}(z_i)] + 12 \text{var}[\delta T_{21}(\ell, y; z_i)] \\ &\times (C_{\ell}^{\bar{\kappa} \delta T_{21}}(y; z_i))^2 + 6 (B_{\ell, \text{sky}}^{\bar{\kappa} \delta T_{21} \delta T_{21}}(y; z_i))^2 \end{aligned} \quad (\text{B.26})$$

Bibliography

- [1] John C Mather, ES Cheng, RE Eplee Jr, RB Isaacman, SS Meyer, RA Shafer, R Weiss, EL Wright, CL Bennett, NW Boggess, et al. A preliminary measurement of the cosmic microwave background spectrum by the cosmic background explorer (cobe) satellite. *The Astrophysical Journal*, 354:L37–L40, 1990.
- [2] David N Spergel, Licia Verde, Hiranya V Peiris, E Komatsu, MR Nolta, CL Bennett, M Halpern, G Hinshaw, N Jarosik, A Kogut, et al. First-year wilkinson microwave anisotropy probe (wmap)* observations: determination of cosmological parameters. *The Astrophysical Journal Supplement Series*, 148(1):175, 2003.
- [3] Peter AR Ade, N Aghanim, MIR Alves, C Armitage-Caplan, M Arnaud, M Ashdown, F Atrio-Barandela, J Aumont, H Aussel, C Baccigalupi, et al. Planck 2013 results. I. Overview of products and scientific results. *Astronomy & Astrophysics*, 571:A1, 2014.
- [4] Matthew Colless, Gavin Dalton, Steve Maddox, Will Sutherland, Peder Norberg, Shaun Cole, Joss Bland-Hawthorn, Terry Bridges, Russell Cannon, Chris Collins, et al. The 2df galaxy redshift survey: spectra and redshifts. *Monthly Notices of the Royal Astronomical Society*, 328(4):1039–1063, 2001.
- [5] Donald G York, J Adelman, John E Anderson Jr, Scott F Anderson, James Annis, Neta A Bahcall, JA Bakken, Robert Barkhouser, Steven Bastian, Eileen Berman,

- et al. The sloan digital sky survey: Technical summary. *The Astronomical Journal*, 120(3):1579, 2000.
- [6] Adam G. Riess, Alexei V. Filippenko, Peter Challis, Alejandro Clocchiatti, Alan Diercks, Peter M. Garnavich, Ron L. Gilliland, Craig J. Hogan, Saurabh Jha, Robert P. Kirshner, and et al. Observational evidence from supernovae for an accelerating universe and a cosmological constant. *The Astronomical Journal*, 116(3):10091038, Sep 1998.
- [7] Wendy L Freedman, Barry F Madore, Brad K Gibson, Laura Ferrarese, Daniel D Kelson, Shoko Sakai, Jeremy R Mould, Robert C Kennicutt Jr, Holland C Ford, John A Graham, et al. Final results from the hubble space telescope key project to measure the hubble constant. *The Astrophysical Journal*, 553(1):47, 2001.
- [8] Max Tegmark, Michael R. Blanton, Michael A. Strauss, Fiona Hoyle, David Schlegel, Roman Scoccimarro, Michael S. Vogeley, David H. Weinberg, Idit Zehavi, Andreas Berlind, and et al. The Three Dimensional Power Spectrum of Galaxies from the Sloan Digital Sky Survey. *The Astrophysical Journal*, 606(2):702740, May 2004.
- [9] Shaun Cole, Will J Percival, John A Peacock, Peder Norberg, Carlton M Baugh, Carlos S Frenk, Ivan Baldry, Joss Bland-Hawthorn, Terry Bridges, Russell Cannon, et al. The 2dF Galaxy Redshift Survey: power-spectrum analysis of the final data set and cosmological implications. *Monthly Notices of the Royal Astronomical Society*, 362(2):505–534, 2005.
- [10] Alexandre Refregier, Jason Rhodes, and Edward J Groth. Cosmic shear and power spectrum normalization with the hubble space telescope. *The Astrophysical Journal Letters*, 572(2):L131, 2002.
- [11] Rupert AC Croft, David H Weinberg, Mike Bolte, Scott Burles, Lars Hernquist, Neal Katz, David Kirkman, and David Tytler. Toward a precise measurement of matter

- clustering: Ly α forest data at redshifts 2-4. *The Astrophysical Journal*, 581(1):20, 2002.
- [12] Adam G. Riess, LouisGregory Strolger, John Tonry, Stefano Casertano, Henry C. Ferguson, Bahram Mobasher, Peter Challis, Alexei V. Filippenko, Saurabh Jha, Weidong Li, and et al. Type Ia Supernova Discoveries at $z > 1$ from the Hubble Space Telescope: Evidence for past deceleration and constraints on dark energy evolution. *The Astrophysical Journal*, 607(2):665687, Jun 2004.
- [13] P Astier, J Guy, and N Regnault. The supernova legacy survey: Measurement of Ω_m , Ω_Λ , and w from the. *Astronomy and Astrophysics*, 447:1, 2005.
- [14] Sidney van den Bergh. The early history of dark matter. *Publications of the Astronomical Society of the Pacific*, 111(760):657660, Jun 1999.
- [15] K. Freese. Review of observational evidence for dark matter in the universe and in upcoming searches for dark stars. *EAS Publications Series*, 36:113126, 2009.
- [16] Fritz Zwicky. Die rotverschiebung von extragalaktischen nebeln. *Helvetica Physica Acta*, 6:110–127, 1933.
- [17] Vera C Rubin and W Kent Ford Jr. Rotation of the andromeda nebula from a spectroscopic survey of emission regions. *The Astrophysical Journal*, 159:379, 1970.
- [18] Richard Massey, Thomas Kitching, and Johan Richard. The dark matter of gravitational lensing. *Reports on Progress in Physics*, 73(8):086901, Jul 2010.
- [19] Raphael Gavazzi, Tommaso Treu, Jason D. Rhodes, Leon V. E. Koopmans, Adam S. Bolton, Scott Burles, Richard J. Massey, and Leonidas A. Moustakas. The Sloan Lens ACS Survey. IV. The mass density profile of earlytype galaxies out to 100 effective radii. *The Astrophysical Journal*, 667(1):176190, Sep 2007.
- [20] N. W. Halverson, E. M. Leitch, C. Pryke, J. Kovac, J. E. Carlstrom, W. L. Holzapfel, M. Dragovan, J. K. Cartwright, B. S. Mason, S. Padin, and et al. Degree angular

scale interferometer first results: A measurement of the cosmic microwave background angular power spectrum. *The Astrophysical Journal*, 568(1):3845, Mar 2002.

- [21] Alan H Guth. Inflationary universe: A possible solution to the horizon and flatness problems. *Physical Review D*, 23(2):347, 1981.
- [22] Philip JE Peebles and JT Yu. Primeval adiabatic perturbation in an expanding universe. *The Astrophysical Journal*, 162:815, 1970.
- [23] Thanu Padmanabhan. *Structure formation in the universe*. Cambridge university press, 1993.
- [24] Wayne Hu. Lecture notes on cmb theory: From nucleosynthesis to recombination, 2008.
- [25] PF Scott, Richard Saunders, Guy Pooley, Cr idhe O’Sullivan, AN Lasenby, Michael Jones, MP Hobson, PJ Duffett-Smith, and Joanne Baker. Measurements of structure in the cosmic background radiation with the cambridge cosmic anisotropy telescope. *The Astrophysical Journal Letters*, 461(1):L1, 1996.
- [26] Arthur Kosowsky. The atacama cosmology telescope. *New Astronomy Reviews*, 47(11-12):939–943, 2003.
- [27] GS Tucker, HP Gush, M Halpern, I Shinkoda, and W Towlson. Anisotropy in the microwave sky: Results from the first flight of the balloon-borne anisotropy measurement (bam). *The Astrophysical Journal Letters*, 475(2):L73, 1997.
- [28] P De Bernardis, Peter AR Ade, R Artusa, JJ Bock, A Boscaleri, BP Crill, G De Troia, PC Farese, M Giacometti, VV Hristov, et al. Mapping the cmb sky: the boomerang experiment. *New Astronomy Reviews*, 43(2-4):289–296, 1999.
- [29] BP Crill, Peter AR Ade, Elia Stefano Battistelli, S Benton, R Bihary, JJ Bock, JR Bond, J Brevik, S Bryan, CR Contaldi, et al. Spider: a balloon-borne large-scale cmb polarimeter. In *Space Telescopes and Instrumentation 2008: Optical, Infrared, and*

- Millimeter*, volume 7010, page 70102P. International Society for Optics and Photonics, 2008.
- [30] Florian Beutler, Chris Blake, Matthew Colless, D Heath Jones, Lister Staveley-Smith, Lachlan Campbell, Quentin Parker, Will Saunders, and Fred Watson. The 6df galaxy survey: baryon acoustic oscillations and the local hubble constant. *Monthly Notices of the Royal Astronomical Society*, 416(4):3017–3032, 2011.
- [31] Chris Blake, Eyal A Kazin, Florian Beutler, Tamara M Davis, David Parkinson, Sarah Brough, Matthew Colless, Carlos Contreras, Warrick Couch, Scott Croom, et al. The wigglez dark energy survey: mapping the distance–redshift relation with baryon acoustic oscillations. *Monthly Notices of the Royal Astronomical Society*, 418(3):1707–1724, 2011.
- [32] Lauren Anderson, Eric Aubourg, Stephen Bailey, Dmitry Bizyaev, Michael Blanton, Adam S Bolton, Jon Brinkmann, Joel R Brownstein, Angela Burden, Antonio J Cuesta, et al. The clustering of galaxies in the SDSS-III baryon oscillation spectroscopic survey: baryon acoustic oscillations in the data release 9 spectroscopic galaxy sample. *Monthly Notices of the Royal Astronomical Society*, 427(4):3435–3467, 2012.
- [33] Daniel J Eisenstein, Wayne Hu, and Max Tegmark. Cosmic complementarity: H_0 and ω_m from combining cosmic microwave background experiments and redshift surveys. *The Astrophysical Journal Letters*, 504(2):L57, 1998.
- [34] Daniel Eisenstein. Large-scale structure and future surveys. *arXiv preprint astro-ph/0301623*, 2003.
- [35] Somnath Bharadwaj, Biman B Nath, and Shiv K Sethi. Using HI to probe large scale structures at $z \sim 3$. *Journal of Astrophysics and Astronomy*, 22(1):21–34, 2001.
- [36] Philip Bull, Pedro G Ferreira, Prina Patel, and Mario G Santos. Late-time cosmology with 21 cm intensity mapping experiments. *The Astrophysical Journal*, 803(1):21, 2015.

- [37] Alkistis Pourtsidou, David Bacon, Robert Crittenden, and R Benton Metcalf. Prospects for clustering and lensing measurements with forthcoming intensity mapping and optical surveys. *Monthly Notices of the Royal Astronomical Society*, 459(1):863–870, 2016.
- [38] Christopher Carilli and Steve Rawlings. Science with the square kilometer array: motivation, key science projects, standards and assumptions. *arXiv preprint astro-ph/0409274*, 2004.
- [39] Justin Jonas et al. The meerkat radio telescope. In *MeerKAT Science: On the Pathway to the SKA*, volume 277, page 001. SISSA Medialab, 2018.
- [40] Kevin Bandura, Graeme E Addison, Mandana Amiri, J Richard Bond, Duncan Campbell-Wilson, Liam Connor, Jean-François Cliche, Greg Davis, Meiling Deng, Nolan Denman, et al. Canadian hydrogen intensity mapping experiment (chime) pathfinder. In *Ground-based and Airborne Telescopes V*, volume 9145, page 914522. International Society for Optics and Photonics, 2014.
- [41] LB Newburgh, K Bandura, MA Bucher, T-C Chang, HC Chiang, JF Cliche, R Davé, M Dobbs, C Clarkson, KM Ganga, et al. HIRAX: a probe of dark energy and radio transients. In *Ground-based and Airborne Telescopes VI*, volume 9906, page 99065X. International Society for Optics and Photonics, 2016.
- [42] Xuelei Chen. The tianlai project: a 21cm cosmology experiment. In *International Journal of Modern Physics: Conference Series*, volume 12, pages 256–263. World Scientific, 2012.
- [43] Richard Battye, Ian Browne, Tianyue Chen, Clive Dickinson, Stuart Harper, Lucas Olivari, Michael Peel, Mathieu Remazeilles, Sambit Roychowdhury, Peter Wilkinson, et al. Update on the bingo 21cm intensity mapping experiment. *arXiv preprint arXiv:1610.06826*, 2016.
- [44] Rendong Nan, Di Li, Chengjin Jin, Qiming Wang, Lichun Zhu, Wenbai Zhu, Haiyan Zhang, Youling Yue, and Lei Qian. The five-hundred-meter aperture spherical radio

- telescope (fast) project. *International Journal of Modern Physics D*, 20(06):989–1024, 2011.
- [45] Ruth Pearson and Oliver Zahn. Cosmology from cross correlation of cmb lensing and galaxy surveys. *Physical Review D*, 89(4):043516, 2014.
- [46] Blake D Sherwin, Sudeep Das, Amir Hajian, Graeme Addison, J Richard Bond, Devin Crichton, Mark J Devlin, Joanna Dunkley, Megan B Gralla, Mark Halpern, et al. The atacama cosmology telescope: Cross-correlation of cosmic microwave background lensing and quasars. *Physical Review D*, 86(8):083006, 2012.
- [47] Tapomoy Guha Sarkar, Kanan K Datta, and Somnath Bharadwaj. The CMBR ISW and HI 21 cm cross-correlation angular power spectrum. *Journal of Cosmology and Astroparticle Physics*, 2009(08):019, 2009.
- [48] Tzu-Ching Chang, Ue-Li Pen, Kevin Bandura, and Jeffrey B Peterson. Hydrogen 21-cm intensity mapping at redshift 0.8. *arXiv preprint arXiv:1007.3709*, 2010.
- [49] University of Chicago Lawrence Berkeley National Laboratory Cerro-Tololo Inter-American Observatory Dark Energy Survey Collaboration: Fermilab, University of Illinois at Urbana-Champaign and Brenna Flaugher. The dark energy survey. *International Journal of Modern Physics A*, 20(14):3121–3123, 2005.
- [50] David Alonso, Pedro G Ferreira, Matt J Jarvis, and Kavilan Moodley. Calibrating photometric redshifts with intensity mapping observations. *Physical Review D*, 96(4):043515, 2017.
- [51] Edwin Hubble. A relation between distance and radial velocity among extra-galactic nebulae. *Proceedings of the national academy of sciences*, 15(3):168–173, 1929.
- [52] Scott Dodelson. *Modern cosmology*. Elsevier, 2003.
- [53] Patrick Peter. Cosmological perturbation theory. *arXiv preprint arXiv:1303.2509*, 2013.

- [54] Hannu Kurki-Suonio. Introduction to cosmological perturbation theory. *Lecture Notes*, 2011.
- [55] James M Bardeen. Gauge-invariant cosmological perturbations. *Physical Review D*, 22(8):1882, 1980.
- [56] Chung-Pei Ma and Edmund Bertschinger. Cosmological perturbation theory in the synchronous and conformal newtonian gauges. *arXiv preprint astro-ph/9506072*, 1995.
- [57] Y Akrami, F Arroja, M Ashdown, J Aumont, C Baccigalupi, M Ballardini, AJ Banday, RB Barreiro, N Bartolo, S Basak, et al. Planck 2018 results. i. overview and the cosmological legacy of planck. *arXiv preprint arXiv:1807.06205*, 2018.
- [58] Wayne Hu and Scott Dodelson. Cosmic microwave background anisotropies. *Annual Review of Astronomy and Astrophysics*, 40(1):171–216, 2002.
- [59] Sigurd Naess, Matthew Hasselfield, Jeff McMahon, Michael D Niemack, Graeme E Addison, Peter AR Ade, Rupert Allison, Mandana Amiri, Nick Battaglia, James A Beall, et al. The atacama cosmology telescope: Cmb polarization at 200; j 9000. *Journal of Cosmology and Astroparticle Physics*, 2014(10):007, 2014.
- [60] Pea de Bernardis, Peter AR Ade, JJ Bock, JR Bond, J Borrill, A Boscaleri, K Coble, BP Crill, G De Gasperis, PC Farese, et al. A flat universe from high-resolution maps of the cosmic microwave background radiation. *Nature*, 404(6781):955–959, 2000.
- [61] Sea Hanany, P Ade, A Balbi, J Bock, J Borrill, A Boscaleri, P De Bernardis, PG Ferreira, VV Hristov, AH Jaffe, et al. Maxima-1: a measurement of the cosmic microwave background anisotropy on angular scales of $10^{\prime-5}$. *The Astrophysical Journal Letters*, 545(1):L5, 2000.
- [62] Matias Zaldarriaga and Uroš Seljak. All-sky analysis of polarization in the microwave background. *Physical Review D*, 55(4):1830, 1997.

- [63] MM Hedman, D Barkats, JO Gundersen, Suzanne Therese Staggs, and B Winstein. A limit on the polarized anisotropy of the cosmic microwave background at subdegree angular scales. *The Astrophysical Journal Letters*, 548(2):L111, 2001.
- [64] Edward R Harrison. Fluctuations at the threshold of classical cosmology. *Physical review D*, 1(10):2726, 1970.
- [65] Rashid A Sunyaev and Ya B Zeldovich. Small-scale fluctuations of relic radiation. *Astrophysics and Space Science*, 7(1):3–19, 1970.
- [66] Samuel R Hinton, Eyal Kazin, Tamara M Davis, Chris Blake, Sarah Brough, Matthew Colless, Warrick J Couch, Michael J Drinkwater, Karl Glazebrook, Russell J Jurek, et al. Measuring the 2d baryon acoustic oscillation signal of galaxies in wigglez: cosmological constraints. *Monthly Notices of the Royal Astronomical Society*, page stw2725, 2016.
- [67] Seshadri Nadathur, Paul M Carter, Will J Percival, Hans A Winther, and Julian E Bautista. Beyond bao: Improving cosmological constraints from boss data with measurement of the void-galaxy cross-correlation. *Physical Review D*, 100(2):023504, 2019.
- [68] Valerio Marra and Eddy G Chirinos Isidro. A first model-independent radial bao constraint from the final boss sample. *Monthly Notices of the Royal Astronomical Society*, 487(3):3419–3426, 2019.
- [69] Daniel J Eisenstein, Idit Zehavi, David W Hogg, Roman Scoccimarro, Michael R Blanton, Robert C Nichol, Ryan Scranton, Hee-Jong Seo, Max Tegmark, Zheng Zheng, et al. Detection of the baryon acoustic peak in the large-scale correlation function of sdss luminous red galaxies. *The Astrophysical Journal*, 633(2):560, 2005.
- [70] Wayne Hu and Scott Dodelson. Cosmic microwave background anisotropies. *Annual Review of Astronomy and Astrophysics*, 40(1):171216, Sep 2002.
- [71] Nick Kaiser. Clustering in real space and in redshift space. *Monthly Notices of the Royal Astronomical Society*, 227(1):1–21, 1987.

- [72] Eric V Linder. Cosmic growth history and expansion history. *Physical Review D*, 72(4):043529, 2005.
- [73] Ludovic Van Waerbeke, Y Mellier, T Erben, JC Cuillandre, F Bernardeau, R Maoli, E Bertin, HJ Mc Cracken, O Le Fevre, B Fort, et al. Detection of correlated galaxy ellipticities on cfht data: first evidence for gravitational lensing by large-scale structures. *Arxiv preprint astro-ph/0002500*, 2000.
- [74] Peter Schneider. Detection of (dark) matter concentrations via weak gravitational lensing. *Monthly Notices of the Royal Astronomical Society*, 283(3):837–853, 1996.
- [75] H Hildebrandt, M Viola, C Heymans, S Joudaki, K Kuijken, C Blake, T Erben, B Joachimi, D Klaes, L t Miller, et al. Kids-450: Cosmological parameter constraints from tomographic weak gravitational lensing. *Monthly Notices of the Royal Astronomical Society*, 465(2):1454–1498, 2016.
- [76] Antony Lewis and Anthony Challinor. Weak gravitational lensing of the cmb. *Physics Reports*, 429(1):1–65, 2006.
- [77] Matthias Bartelmann and Peter Schneider. Weak gravitational lensing. *Physics Reports*, 340(4-5):291–472, 2001.
- [78] Ludovic Van Waerbeke, Ismael Tereno, Yannick Mellier, and Francis Bernardeau. Cosmic shear review. *arXiv preprint astro-ph/0212150*, 2002.
- [79] Martin Kilbinger. Cosmology with cosmic shear observations: a review. *Reports on Progress in Physics*, 78(8):086901, 2015.
- [80] Tapomoy Guha Sarkar. CMBR weak lensing and HI 21-cm cross-correlation angular power spectrum. *Journal of Cosmology and Astroparticle Physics*, 2010(02):002, 2010.
- [81] Joachim Wambsganss. Gravitational lensing in astronomy. *Living Reviews in Relativity*, 1(1):12, 1998.

- [82] Y Omori and G Holder. Cross-correlation of cfhtlens galaxy number density and planck cmb lensing. *arXiv preprint arXiv:1502.03405*, 2015.
- [83] Fuyu Dong, Jun Zhang, Yu Yu, Xiaohu Yang, HeKun Li, Jiaxin Han, Wentao Luo, Jiajun Zhang, and Liping Fu. Constraining dark energy with stacked concave lenses. *The Astrophysical Journal*, 874(1):7, 2019.
- [84] Romeel Davé, Neal Katz, Benjamin D Oppenheimer, Juna A Kollmeier, and David H Weinberg. The neutral hydrogen content of galaxies in cosmological hydrodynamic simulations. *Monthly Notices of the Royal Astronomical Society*, 434(3):2645–2663, 2013.
- [85] Jacinta Delhaize, MJ Meyer, LJBB Staveley-Smith, and BJ Boyle. Detection of HI in distant galaxies using spectral stacking. *Monthly Notices of the Royal Astronomical Society*, 433(2):1398–1410, 2013.
- [86] SN Reeves, EM Sadler, JR Allison, BS Koribalski, SJ Curran, and MB Pracy. HI emission and absorption in nearby, gas-rich galaxies. *Monthly Notices of the Royal Astronomical Society*, 450(1):926–942, 2015.
- [87] Steven R Furlanetto, S Peng Oh, and Frank H Briggs. Cosmology at low frequencies: The 21 cm transition and the high-redshift universe. *Physics reports*, 433(4-6):181–301, 2006.
- [88] RS Booth, WJG De Blok, JL Jonas, and B Fanaroff. Meerkat key project science, specifications, and proposals. *arXiv preprint arXiv:0910.2935*, 2009.
- [89] Laura B Newburgh, Graeme E Addison, Mandana Amiri, Kevin Bandura, J Richard Bond, Liam Connor, Jean-François Cliche, Greg Davis, Meiling Deng, Nolan Denman, et al. Calibrating chime: a new radio interferometer to probe dark energy. In *Ground-based and Airborne Telescopes V*, volume 9145, page 91454V. International Society for Optics and Photonics, 2014.

- [90] RA Battye, ML Brown, IWA Browne, RJ Davis, P Dewdney, C Dickinson, G Heron, B Maffei, A Pourtsidou, and PN Wilkinson. Bingo: a single dish approach to 21cm intensity mapping. *arXiv preprint arXiv:1209.1041*, 2012.
- [91] S Peng Oh and Katherine J Mack. Foregrounds for 21-cm observations of neutral gas at high redshift. *Monthly Notices of the Royal Astronomical Society*, 346(3):871–877, 2003.
- [92] Adrian Liu and Max Tegmark. A method for 21 cm power spectrum estimation in the presence of foregrounds. *Physical Review D*, 83(10):103006, 2011.
- [93] Hee-Jong Seo and Christopher M Hirata. The foreground wedge and 21-cm bAO surveys. *Monthly Notices of the Royal Astronomical Society*, 456(3):3142–3156, 2016.
- [94] Miguel F Morales, Judd D Bowman, and Jacqueline N Hewitt. Improving foreground subtraction in statistical observations of 21 cm emission from the epoch of reionization. *The Astrophysical Journal*, 648(2):767, 2006.
- [95] J Richard Shaw, Kris Sigurdson, Michael Sitwell, Albert Stebbins, and Ue-Li Pen. Coaxing cosmic 21 cm fluctuations from the polarized sky using m-mode analysis. *Physical Review D*, 91(8):083514, 2015.
- [96] J Richard Shaw, Kris Sigurdson, Ue-Li Pen, Albert Stebbins, and Michael Sitwell. All-sky interferometry with spherical harmonic transit telescopes. *The Astrophysical Journal*, 781(2):57, 2014.
- [97] Adrian Liu and J Richard Shaw. Data analysis for precision 21 cm cosmology. *arXiv preprint arXiv:1907.08211*, 2019.
- [98] Francisco Villaescusa-Navarro, Shy Genel, Emanuele Castorina, Andrej Obuljen, David N Spergel, Lars Hernquist, Dylan Nelson, Isabella P Carucci, Annalisa Pillepich, Federico Marinacci, et al. Ingredients for 21cm intensity mapping. *arXiv preprint arXiv:1804.09180*, 2018.

- [99] Mário G Santos, Asantha Cooray, and Lloyd Knox. Multifrequency analysis of 21 centimeter fluctuations from the era of reionization. *The Astrophysical Journal*, 625(2):575, 2005.
- [100] Adrian Liu, Max Tegmark, Judd Bowman, Jacqueline Hewitt, and Matias Zaldarriaga. An improved method for 21-cm foreground removal. *Monthly Notices of the Royal Astronomical Society*, 398(1):401–406, 2009.
- [101] Miguel F Morales, Adam Beardsley, Jonathan Pober, Nichole Barry, Bryna Hazelton, Daniel Jacobs, and Ian Sullivan. Understanding the diversity of 21 cm cosmology analyses. *Monthly Notices of the Royal Astronomical Society*, 483(2):2207–2216, 2018.
- [102] Max Tegmark, Andy N Taylor, and Alan F Heavens. Karhunen-loeve eigenvalue problems in cosmology: How should we tackle large data sets? *The Astrophysical Journal*, 480(1):22, 1997.
- [103] Max Tegmark. Measuring cosmological parameters with galaxy surveys. *Physical Review Letters*, 79(20):3806, 1997.
- [104] Chris Blake, Paul Carter, and Jun Koda. Power spectrum multipoles on the curved sky: an application to the 6-degree field galaxy survey. *Monthly Notices of the Royal Astronomical Society*, 479(4):5168–5183, 2018.
- [105] Charles Alcock and Bohdan Paczyński. An evolution free test for non-zero cosmological constant. *Nature*, 281(5730):358–359, 1979.
- [106] Chris Blake and Karl Glazebrook. Probing dark energy using baryonic oscillations in the galaxy power spectrum as a cosmological ruler. *The Astrophysical Journal*, 594(2):665, 2003.
- [107] Beth A Reid, Lado Samushia, Martin White, Will J Percival, Marc Manera, Nikhil Padmanabhan, Ashley J Ross, Ariel G Sánchez, Stephen Bailey, Dmitry Bizyaev, et al.

- The clustering of galaxies in the SDSS-III baryon oscillation spectroscopic survey: measurements of the growth of structure and expansion rate at $z=0.57$ from anisotropic clustering. *Monthly Notices of the Royal Astronomical Society*, 426(4):2719–2737, 2012.
- [108] Shaun A. Thomas, Filipe B. Abdalla, and Jochen Weller. Constraining modified gravity and growth with weak lensing. *Monthly Notices of the Royal Astronomical Society*, 395(1):197209, May 2009.
- [109] Andreas Albrecht, Gary Bernstein, Robert Cahn, Wendy L Freedman, Jacqueline Hewitt, Wayne Hu, John Huth, Marc Kamionkowski, Edward W Kolb, Lloyd Knox, et al. Report of the dark energy task force. *arXiv preprint astro-ph/0609591*, 2006.
- [110] Andreas Albrecht, Luca Amendola, Gary Bernstein, Douglas Clowe, Daniel Eisenstein, Luigi Guzzo, Christopher Hirata, Dragan Huterer, Robert Kirshner, Edward Kolb, et al. Findings of the joint dark energy mission figure of merit science working group. *arXiv preprint arXiv:0901.0721*, 2009.
- [111] Ian Harrison, Stefano Camera, Joe Zuntz, and Michael L Brown. Ska weak lensing—I. cosmological forecasts and the power of radio-optical cross-correlations. *Monthly Notices of the Royal Astronomical Society*, 463(4):3674–3685, 2016.
- [112] Wenkai Hu, Xin Wang, Fengquan Wu, Yougang Wang, Pengjie Zhang, and Xuelei Chen. Forecast for fast: from galaxies survey to intensity mapping. *arXiv preprint arXiv:1909.10946*, 2019.
- [113] Planck Collaboration, N. Aghanim, Y. Akrami, M. Ashdown, J. Aumont, C. Baccigalupi, M. Ballardini, A. J. Banday, R. B. Barreiro, N. Bartolo, S. Basak, R. Battye, K. Benabed, J. P. Bernard, M. Bersanelli, P. Bielewicz, J. J. Bock, J. R. Bond, J. Borrill, F. R. Bouchet, F. Boulanger, M. Bucher, C. Burigana, R. C. Butler, E. Calabrese, J. F. Cardoso, J. Carron, A. Challinor, H. C. Chiang, J. Chluba, L. P. L. Colombo, C. Combet, D. Contreras, B. P. Crill, F. Cuttaia, P. de Bernardis, G. de Zotti, J. Delabrouille, J. M. Delouis, E. Di Valentino, J. M. Diego, O. Dor, M. Douspis, A. Ducout,

X. Dupac, S. Dusini, G. Efstathiou, F. Elsner, T. A. Enlin, H. K. Eriksen, Y. Fantaye, M. Farhang, J. Fergusson, R. Fernandez-Cobos, F. Finelli, F. Forastieri, M. Frailis, A. A. Fraisse, E. Franceschi, A. Frolov, S. Galeotta, S. Galli, K. Ganga, R. T. Gnova-Santos, M. Gerbino, T. Ghosh, J. Gonzalez-Nuevo, K. M. Grski, S. Gratton, A. Gruppuso, J. E. Gudmundsson, J. Hamann, W. Handley, F. K. Hansen, D. Herranz, S. R. Hildebrandt, E. Hivon, Z. Huang, A. H. Jaffe, W. C. Jones, A. Karakci, E. Keihnen, R. Keskitalo, K. Kiiveri, J. Kim, T. S. Kisner, L. Knox, N. Krachmalnicoff, M. Kunz, H. Kurki-Suonio, G. Lagache, J. M. Lamarre, A. Lasenby, M. Lattanzi, C. R. Lawrence, M. Le Jeune, P. Lemos, J. Lesgourgues, F. Levrier, A. Lewis, M. Liguori, P. B. Lilje, M. Lilley, V. Lindholm, M. Lopez-Caniego, P. M. Lubin, Y. Z. Ma, J. F. Macas-Prez, G. Maggio, D. Maino, N. Mandolesi, A. Mangilli, A. Marcos-Caballero, M. Maris, P. G. Martin, M. Martinelli, E. Martinez-Gonzalez, S. Matarrese, N. Mauri, J. D. McEwen, P. R. Meinhold, A. Melchiorri, A. Mennella, M. Migliaccio, M. Millea, S. Mitra, M. A. Miville-Deschnes, D. Molinari, L. Montier, G. Morgante, A. Moss, P. Natoli, H. U. Nrgaard-Nielsen, L. Pagano, D. Paoletti, B. Partridge, G. Patanchon, H. V. Peiris, F. Perrotta, V. Pettorino, F. Piacentini, L. Polastri, G. Polenta, J. L. Puget, J. P. Rachen, M. Reinecke, M. Remazeilles, A. Renzi, G. Rocha, C. Rosset, G. Roudier, J. A. Rubio-Martn, B. Ruiz-Granados, L. Salvati, M. Sandri, M. Savelainen, D. Scott, E. P. S. Shellard, C. Sirignano, G. Sirri, L. D. Spencer, R. Sunyaev, A. S. Suur-Uski, J. A. Tauber, D. Tavagnacco, M. Tenti, L. Toffolatti, M. Tomasi, T. Trombetti, L. Valenziano, J. Valiviita, B. Van Tent, L. Vibert, P. Vielva, F. Villa, N. Vittorio, B. D. Wandelt, I. K. Wehus, M. White, S. D. M. White, A. Zacchei, and A. Zonca. Planck 2018 results. vi. cosmological parameters, 2018.

[114] David R DeBoer, Aaron R Parsons, James E Aguirre, Paul Alexander, Zaki S Ali, Adam P Beardsley, Gianni Bernardi, Judd D Bowman, Richard F Bradley, Chris L Carilli, et al. Hydrogen epoch of reionization array (hera). *Publications of the Astronomical Society of the Pacific*, 129(974):045001, 2017.

[115] Joshua S Dillon and Aaron R Parsons. Redundant array configurations for 21 cm

cosmology. *The Astrophysical Journal*, 826(2):181, 2016.

- [116] Francesco De Bernardis for the ACT collaboration, Jason Stevens, M. Hasselfield, D. Alonso, J. R. Bond, E. Calabrese, S. K. Choi, K. T. Crowley, M. Devlin, J. Dunkley, and et al. Survey strategy optimization for the atacama cosmology telescope. *Observatory Operations: Strategies, Processes, and Systems VI*, Jul 2016.
- [117] SW Henderson, R Allison, J Austermann, T Baildon, N Battaglia, JA Beall, D Becker, Francesco De Bernardis, JR Bond, Erminia Calabrese, et al. Advanced actpol cryogenic detector arrays and readout. *Journal of Low Temperature Physics*, 184(3-4):772–779, 2016.
- [118] Takemi Okamoto and Wayne Hu. Cosmic microwave background lensing reconstruction on the full sky. *Physical Review D*, 67(8):083002, 2003.
- [119] Chi-Ting Chiang, Christian Wagner, Fabian Schmidt, and Eiichiro Komatsu. Position-dependent power spectrum of the large-scale structure: a novel method to measure the squeezed-limit bispectrum. *Journal of Cosmology and Astroparticle Physics*, 2014(05):048, 2014.
- [120] Francis Bernardeau, S Colombi, E Gaztanaga, and R Scoccimarro. Large-scale structure of the universe and cosmological perturbation theory. *Physics reports*, 367(1-3):1–248, 2002.
- [121] Chi-Ting Chiang. Position-dependent power spectrum: a new observable in the large-scale structure. *arXiv preprint arXiv:1508.03256*, 2015.
- [122] John A Peacock, Shaun Cole, Peder Norberg, Carlton M Baugh, Joss Bland-Hawthorn, Terry Bridges, Russell D Cannon, Matthew Colless, Chris Collins, Warrick Couch, et al. A measurement of the cosmological mass density from clustering in the 2df galaxy redshift survey. *Nature*, 410(6825):169, 2001.

- [123] KW Masui, ER Switzer, N Banavar, K Bandura, C Blake, L-M Calin, T-C Chang, X Chen, Y-C Li, Y-W Liao, et al. Measurement of 21 cm brightness fluctuations at $z = 0.8$ in cross-correlation. *The Astrophysical Journal Letters*, 763(1):L20, 2013.
- [124] Michael Levi, Chris Bebek, Timothy Beers, Robert Blum, Robert Cahn, Daniel Eisenstein, Brenna Flaugher, Klaus Honscheid, Richard Kron, Ofer Lahav, et al. The desi experiment, a whitepaper for snowmass 2013. *arXiv preprint arXiv:1308.0847*, 2013.
- [125] Zeljko Ivezic, JA Tyson, B Abel, E Acosta, R Allsman, Y AlSayyad, SF Anderson, J Andrew, R Angel, G Angeli, et al. Lsst: from science drivers to reference design and anticipated data products. *arXiv preprint arXiv:0805.2366*, 2008.
- [126] D Spergel, N Gehrels, C Baltay, D Bennett, J Breckinridge, M Donahue, A Dressler, BS Gaudi, T Greene, O Guyon, et al. Wide-field infrared survey telescope-astrophysics focused telescope assets wfirst-afta 2015 report. *arXiv preprint arXiv:1503.03757*, 2015.
- [127] D. Spergel, N. Gehrels, C. Baltay, D. Bennett, J. Breckinridge, M. Donahue, A. Dressler, B. S. Gaudi, T. Greene, O. Guyon, C. Hirata, J. Kalirai, N. J. Kasdin, B. Macintosh, W. Moos, S. Perlmutter, M. Postman, B. Rauscher, J. Rhodes, Y. Wang, D. Weinberg, D. Benford, M. Hudson, W. S. Jeong, Y. Mellier, W. Traub, T. Yamada, P. Capak, J. Colbert, D. Masters, M. Penny, D. Savransky, D. Stern, N. Zimmerman, R. Barry, L. Bartusek, K. Carpenter, E. Cheng, D. Content, F. Dekens, R. Demers, K. Grady, C. Jackson, G. Kuan, J. Kruk, M. Melton, B. Nemati, B. Parvin, I. Poberezhskiy, C. Peddie, J. Ruffa, J. K. Wallace, A. Whipple, E. Wollack, and F. Zhao. Wide-field infrared survey telescope-astrophysics focused telescope assets wfirst-afta 2015 report, 2015.
- [128] Hiranya V Peiris and David N Spergel. Cross-correlating the sloan digital sky survey with the microwave sky. *The Astrophysical Journal*, 540(2):605, 2000.
- [129] Eifler et al. In preparation 2019.

- [130] Alkistis Pourtsidou. Synergistic tests of inflation. *arXiv preprint arXiv:1612.05138*, 2016.